Doctor of Engineering Thesis

Study on Frame Vibration Suppression Control Method for Position Sensorless drive System of Permanent Magnet Synchronous Motor

(永久磁石同期モーターの位置センサレス制御におけるフレーム振動抑制に関する研究)

Suthep Supharat

Division of System Engineering,

Graduate School of Engineering

Mie University, Japan

September, 2016

三重大学

I declare that this chapter contains no material which has been accepted for a degree or diploma by the University or any other institution, except by way of background information and duly acknowledged in the thesis, and that, to the best of my knowledge and belief, this thesis contains no material previously published or written by another person, except where due acknowledgement is made in the text of the thesis.

Signed: _____

Suthep Supharat

Date: _____

Signed:_____

Suthep Supharat

Date: _____

Doctor of Engineering

DEGREE

Electrical Control System	System Engineering
LABORATORY	DIVISION

TITLE: **Study on Frame Vibration Suppression Control Method for Position Sensorless drive System of Permanent Magnet Synchronous Motor (永久磁石同期モーターの位置センサレス制御におけるフレーム振動抑制に関する研究)**

NAME: **Mr. Suthep Supharat**

THIS THESIS HAS BEEN ACCEPTED BY

THESIS ADVISOR

(**Professor Dr. Muneaki Ishida**)

THESIS REFEREE

(**Professor Dr. Junji Hirai**)

THESIS REFEREE

(**Professor Dr. Satoshi Komada**)

THESIS REFEREE

(**Associate Professor Dr. Naoki Yamamura**)

ABSTRACT

Permanent magnet synchronous motor has been widely used in variable speed drive system for various fields, such as industry, household applications, etc., The merits of PMSM are rugged construction, high efficiency, high torque to current ratio, low inertia, etc. Recently, PMSM driven air-conditioners and refrigerators are obviously increased. However, the compressors used in the air-conditioners have the problem that vibration occurs due to the torque pulsation. The frame vibration results in adverse effects, such as mechanical damage, acoustic noise and deterioration of control performance, etc.. Therefore, the vibration suppression control of PMSM driven compressor has been demanded.

As a method of vibration suppression, a rubber vibration insulator has been applied. However, anti-vibration rubber is affected by the environment, such as temperature, etc.. There are disadvantages, such as short usage life, etc..

In the earlier research, several solutions have been presented based on either additional sensors, such as accelerometers, position sensors, etc., or advanced control techniques, such as the internal model principle, etc. However, the use of sensors includes negative aspects such as high-cost, more space and low reliability. As a result, the research on sensorless skill is a hot point.

In the prior studies, the vibration suppression technique by a repetitive control with Fourier Transformer (FT) have been proposed. A compensation signal for vibration suppression is generated from the signal detected by the acceleration sensor and performs vibration suppression control by being superimposed to the torque current reference of the PMSM. However, in the conventional technique, it is necessary to install an acceleration sensor to detect frame vibration. As the same time, the position sensor is required to detect the rotor angular position of the PMSM. Use of these sensors depends on environmental constraints, such as temperature and installation space. High cost is also one of the reasons why it's not preferred.

In this study, a novel frame anti-vibration control method which is called Specific Component Reduction Control (SCRC) is proposed. In this method, a position sensorless speed control system is built using the Extended Electromotive Force (EEMF) observer. Then, the estimated velocity is used for generating a compensation signal in SCRC through a Fourier Transformer, to achieve the vibration suppression control without the position sensor or the acceleration sensor. Here, the conventional technique to generate compensation signal has been the repetitive controller. However, this method has a large

gain in high frequency regions. The high frequency noise include in the estimated position. This noise with the position sensorless control has been increased although the desired frequency component of the vibration has been detected by FT. In this study, a new vibration suppression control method (SCRC) that takes the replace of the repetitive controller is proposed. In SCRC, the extracted vibration frequency component by the FT is learned by the integrator to generate the compensation signal. SCRC is quite difficult to amplify the noise for performing a compensation signal generation using the estimated position information. The stability analysis is also carried out. In addition, there is the possibility to perform the vibration suppression control in variable speed and the mechanical resonance point vicinity in the future.

The proposed control method has the following features:

(1). In our system, the estimated speed from EEMF observer has been taken as the input of SCRC. As a result, accelerometer is not necessary in the whole system.

(2). The Fourier Transformation(FT) has been applied in SCRC. Only one target frequency component which is the same as command speed frequency has been taken into SCRC. The vibration suppression control system is easily stabilized by the adjustment of control parameters in SCRC. Since there is no positive feedback in SCRC, the high-frequency components are not amplified.

(3). By proper calculation, SCRC can be performed as the form of Repetitive Controller based on the position which is not fluctuated. After simplifying the whole system, the linearized system diagram can be got. With this system diagram, Nyquist analysis is applied to design two most important parameters in SCRC. The target frequency harmonics component which is the same as the command mechanical speed frequency can be effectively eliminated by SCRC.

(4). The experiment is carried out in the different constant speed regions, and speed variable control is also achieved with the proper design of parameters in SCRC.

(5) SCRC has been developed, not only for the first-order frequency component of the estimated speed signal, but also for the second-order one. It shows that SCRC can be taken into practice of multiple components application. This controller is named as Multiple Specific Component Reduction Controller (M-SCRC).

The position sensorless method, using a low-pass filter and the Extended Electromotive Force Model can't estimate zero speed. As a result, a huge speed estimation error happens in the very low-speed region due to the parameter error and model error of the motor. The PMSM parameter estimation and new position sensorless method will be developed for the very low speed in the near future.

ACKNOWLEDGEMENTS

I wish to thank all those who helped me in completing my degree during my graduate studies in the Mie University. Several persons collaborated directly and indirectly with my research and encouraged me to finish the works. That is why I wish to dedicate this section to recognize their support.

Firstly, I wish to gratefully acknowledge the enthusiastic supervision of my Ph.D study and my thesis supervisor Professor Dr. Junji Hirai I sincerely appreciate him for his patience, unselfish support, motivation and immense knowledge the whole time of my study at the Control System Laboratory, Division of Electrical and Electronics Engineering, Graduate School of Engineering, Mie University. I could not have imagined if he does not call me back from Thailand for the continuous PhD study at Mie University. The influence of his excellent personality and erudite knowledge helped me to success the research and completed this thesis.

I thank my research advisor, Prof. Ishida, for his continuous guidance throughout the process of performing my research and organizing this dissertation. He always showed me the right direction to finish this work with his passion and supported me throughout all the way. I thank all the professors in my committee, Professor Dr. Satoshi Komada and , Associate Professor Dr. Naoki Yamamura, who gave me advice whenever I asked. I owe my sincere gratitude to all professors who guided me to have engineering scope.

I sincerely hope to mention the students at the Electrical system Laboratory of Mie University for their assisting during I have been at this Laboratory. Moreover, I wish to thank to Thai students at Mie University for the good memory during my staying.

Finally, I would link to take this opportunity to thank my mother and father, my brother and sister, including all of contains, for their constant affections, encouragements, and supports since I have come to Japan until I can finish my task as a Ph.D.

TABLE OF CONTENTS

LIST OF FIGURES

Chapter 1

Chapter 2

Chapter 3

Chapter 4

Chapter 5

Chapter 6

List of Tables

Chapter 1

Chapter 6

Chapter 7

Nomenclature

B	magnetic flux density
E	open circuit phase emf voltage, electric field
E_d	d-axis emf voltage at steady-state
E_q	q-axis emf voltage at steady-state
I_d	d-axis phase current at steady-state
I_q	q-axis phase current at steady-state
i_a, i_b, i_c	instantaneous phase current of the stator windings
I_{max}	maximum input phase current
J	current density in the elements
L_s	Stator inductance of PMSM
L	phase inductance of the stator windings
L_d	phase inductance of d-axis
L_q	phase inductance of q-axis
P	real power per phase per pole-pair of the motor
p	differential operator
R	resistance of the stator windings
T_s	Sampling period
T_{dif}	output torque
T_e	motor driving torque
T_L	load torque
$\Delta\tau_{Lrip}$	load torque ripple
$\varphi_{\omega rip}$	phase of the speed ripple
$\delta\theta_{rfm}$	position angle error
ϕ	magnetic flux
Φ	magnetic flux at the stator caused stator current
Ke	flux-linkage produced by the permanent magnet
E_α	α-axis stator back-EMF in the stationary reference frame
E_β	β-axis stator back-EMF in the stationary reference frame
$\hat{e}_{\alpha\beta}$	αβ -axis estimated by the EEMF observer
f_c	Cutoff frequency of LPF
v_α	α-axis stator voltage in the stationary reference frame
v_β	β-axis stator voltage in the stationary reference frame
v_d	d-axis stator voltage in the rotor reference frame
v_q	q-axis stator voltage in the rotor reference frame
i_α	α-axis stator current in the stationary reference frame
i_β	β-axis stator current in the stationary reference frame
i_d	d-axis stator current in the rotor reference frame
i_q	q-axis stator current in the rotor reference frame
θ_{rm}	rotor mechanical position
θ_{fm}	frame mechanical position
θ_{rfm}	motor mechanical position

$\hat{\theta}_{rfm}$	motor mechanical estimated position
k_3	integration gain
k_4	phase compensation gain.
$A\tau_{Lrip}$	amplitude of the load torque ripple
-α	designed real axis pole of EEMF
τ	time constant of the derivative filter
ω_e	electrical angular velocity
ω_{fm}	frame mechanism speed
$\Delta\omega_{rip}$	periodic speed ripple
ω_{rfm}	motor mechanical speed
$\hat{\omega}_{rfm}$	motor mechanical estimated speed
ω_n	target angular frequency of vibration
s	Laplace operator
AC	alternating current
BDCM	brushless DC motor, also called BLDC
DC	direct current
d	direct axis
q	quadrature axis
emf	electromotive force
IPMSM	interior permanent magnet synchronous motor
IM	induction motor
PM	permanent magnet
PMSM	permanent magnet synchronous motor
SPMSM	surface-mounted permanent magnet synchronous motor
FFT	Fast Fourier Transform
LPF	Low-Pass Filter
PI	Proportional-Integral
PWM	Pulse Width Modulation
VC	Vector Control
Back-EMF	Back Electromagnetic Force
rpm	revolution per minute
k_{in}	SCRC parameter gain compensation
φ_{cn}	SCRC parameter phase compensation

Chapter 1

I. INTRODUCTION

1.1 Backgrounds

DC electric machine drive systems had been adopted in a variety of industrial applications for more than 100 years, due to the convenience of control. During the past 30 years, with the development of power electronics technology, digital signal processors (DSPs), and computer control theory, AC motor drives [1]-[3] have achieved the same performance as DC motor drives and have potentials to occupy the market in speed variable drive applications. Nowadays, various types of AC drives with induction machines (IM), permanent-magnet synchronous machines (PMSM), switched reluctance machines (SRM), etc., are widely used in industrial applications.

Permanent magnet synchronous motors (PMSMs) have widely been used in speed-variable drive applications such as industry, home applications, etc. due to its rugged construction, high efficiency, and high torque to current ratio, low inertia, etc. But in PMSM speed-variable applications, a position sensor like optical encoder is necessary for the PMSM control system to obtain the rotor position and speed. However, sensors increase the complexity, weight, and cost of the system. In recent years, rotors with the active utilization of reluctance torque, concentrated-winding stators, and other modifications have been introduced for even more efficient, compact, and powerful PMSM designs. However, compact motors show a trend towards stronger torque pulsation produced by space harmonics due to magnetic saturation and other factors, and stronger frame vibration due to greater radial forces caused by magnetic saturation and a smaller air gap. Methods of suppressing such frame vibration are necessary to prevent degradation of control performance, generation of acoustic noise, and deterioration of the mechanical system.

The mechanical vibration analysis of electrical devices has become a major area in improving the performance and efficiency of the system [4]. There are various related techniques. The basis of these strategies includes data capturing, analysis and formation of the control signal in the control system. In this paper, some of these techniques used currently will be discussed and some improvement or advanced versions for them are tried to find.

Methods of vibration suppression can be divided into passive and active [5] and [6]. Passive methods are represented by rubber insulators and other dampers. Rubber

insulators have the advantages of multidirectional damping and simple design but their damping characteristics are strongly affected by humidity and other ambient conditions. On the other hand, there are active mass dampers and another actuator- based methods. Active methods are based on the generation of vibrations of opposite phase, thus canceling the vibrations of the object. Such systems using displacement or acceleration detected by sensors have been implemented in high-speed railways and passenger car suspensions [7]. However, all the above methods require additional components, such as rubber dampers, sensors, and actuators, which inevitably results in higher cost of the control system.

The speed control system such as an air compressor is presented in this study, where attachment of the rotor position sensor is a difficult speed control system. Rotor position sensorless speed control system is recommended. As refered in [8] , the position sensorless control system using the zero-cross point of the electromotive force, speed ripple has been performed by the repetitive control, which is widely applied.

1.2 The Synchronous motor[1]

1.2.1 Electric motors

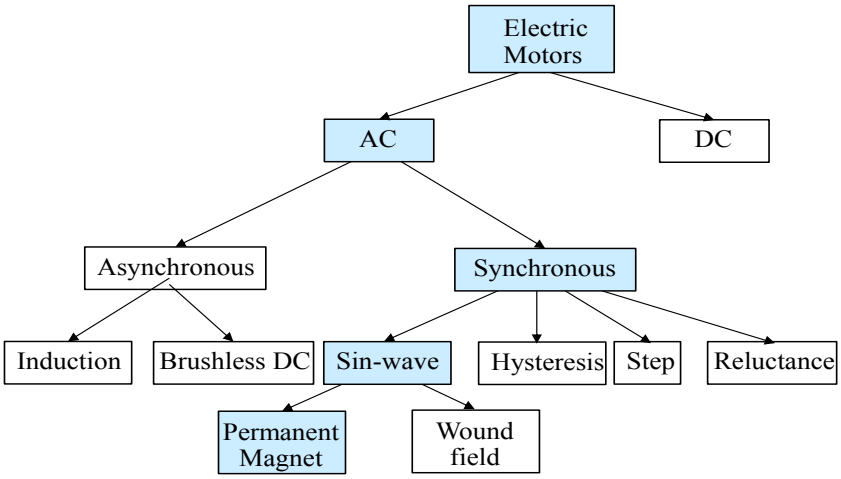

Fig. 1.1 Classification of electric motors

Among all the existing motors on the market, there are three ‘classical motors’: the Direct Current motor with commutators (wound field or permanent magnet field) and two alternative current motors the synchronous and the asynchronous motors. These motors,

when properly controlled, produce constant instantaneous torque (very little torque ripple) and operate from pure DC or AC sine wave supplies. The motor studied in this application note is part of the alternative current supplied motors. It is synchronous motor as its speed may directly be determined by the stator frequency and the number of poles.

Table 1-1 Comparison of the electric motors for the application.

Machine Type	Advantages	Disadvantages
DC Motor	• Easy control • Desirable torque-speed characteristics	• Frequent need of maintenance • Low efficiency and reliability • Low speed range
Induction Motor (IM)	• High speed range • High reliability • Low cost • Rigidity in hostile environments	• Low power density and large size • Low efficiency • Thermal problem at high speed
PM Synchronous Motor (PMSM)	• High power density and small size • High efficiency	• Limited speed range • High cost • High stator core loss at high speed
Switched Reluctance Motor (SRM)	• Desirable torque-speed characteristics • High reliability • Low cost • Rigidity in hostile environments	• High torque ripple and noise • Low power density • Low efficiency

Since DC motor systems have the proper characteristics for the traction application of vehicles, they were popularly used a couple of decades ago [9]. Thanks to the rapid development of large-scale integrated (LSI) circuits and powerful switching devices, such as IGBT (insulated gated bipolar transistor), the Induction Motor (IM), Permanent Magnet Synchronous Motor (PMSM), and Switched Reluctance Motor (SRM) can achieve the same performance as DC motor systems. Each type of motor has its own advantages and disadvantages as listed in Table 1.1 which are summarized from references [10] with knowledge about electric machines.

1.2.2 Permanent Magnet Synchronous Machines

The most widely used PMSMs [11] have an external stator with conductors and an internal rotor with PMs. According to the rotor structures, the PMSMs with an approximately sinusoidal back electromotive force (EMF) can be broadly characterized into two major categories: non-salient-pole PMSMs, e.g., surface-mounted PMSMs SPMSM), and salient-pole PMSMs, e.g., interior PMSMs (IPMSM). A comparison of different types of PMSMs can be found in [12] and [13].

The cross-section of a typical SPMSM is shown in Figure 1.1(a). Since the PMs are mounted on the surface of the rotor core, the SPMSM has a uniform effective air gap. This property makes the synchronous inductances in direct (*d*-) and quadrature (*q*-) axes to be the same. As a result, the SPMSM only produces a magnetic torque. Compared with the IPMSM, the SPMSM has a relatively limited flux-weakening capability. The surface mounted rotor configuration is simple enough for manufacturing and assembly. However, the PMs are exposed directly to the armature reaction field and at the risk of demagnetization. Due to the surface mounted rotor structure, the shaft rotating speed should be limited to keep the PMs at the rotor surface against the effect of the centrifugal force. Therefore, SPMSMs are commonly used in low-speed applications, e.g., WECSs and household appliances.

A typical cross-section of an IPMSM is shown in Figure 1.1(b), where the magnets are buried and effectively shielded in the rotor iron, which significantly reduces the risk of demagnetization of the PMs during the flux-weakening operation. Due to the rotor saliency, the *d*-axis and *q*-axis inductances are different. Both the magnetic torque and the reluctance torque contribute to the total torque produced by the IPMSM. For these reasons, IPMSM is more applicable for traction applications in electric-drive vehicle systems, which require flux weakening operation and high output torque.

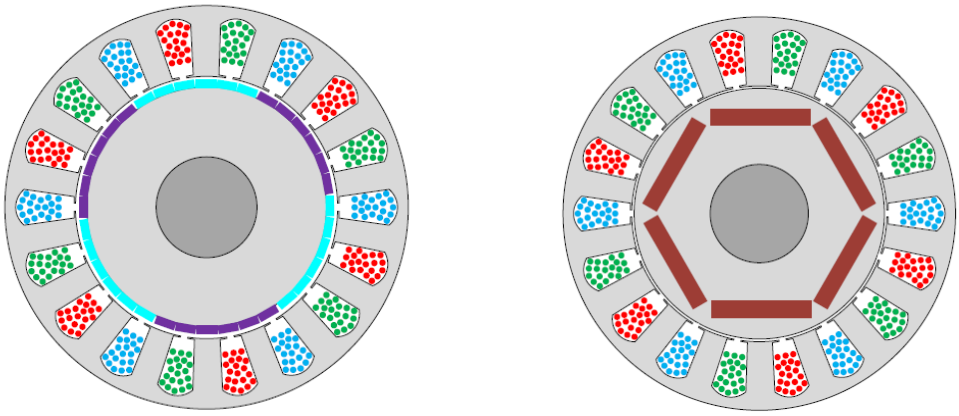

(a) (b)

Fig. 1.2 Illustrations typical PMSMs: (a) a cross-section of SPMSM and (b) a cross sections of IPMSM.

1.2.3 Sensorless Field Oriented Control (FOC) for IPMSM

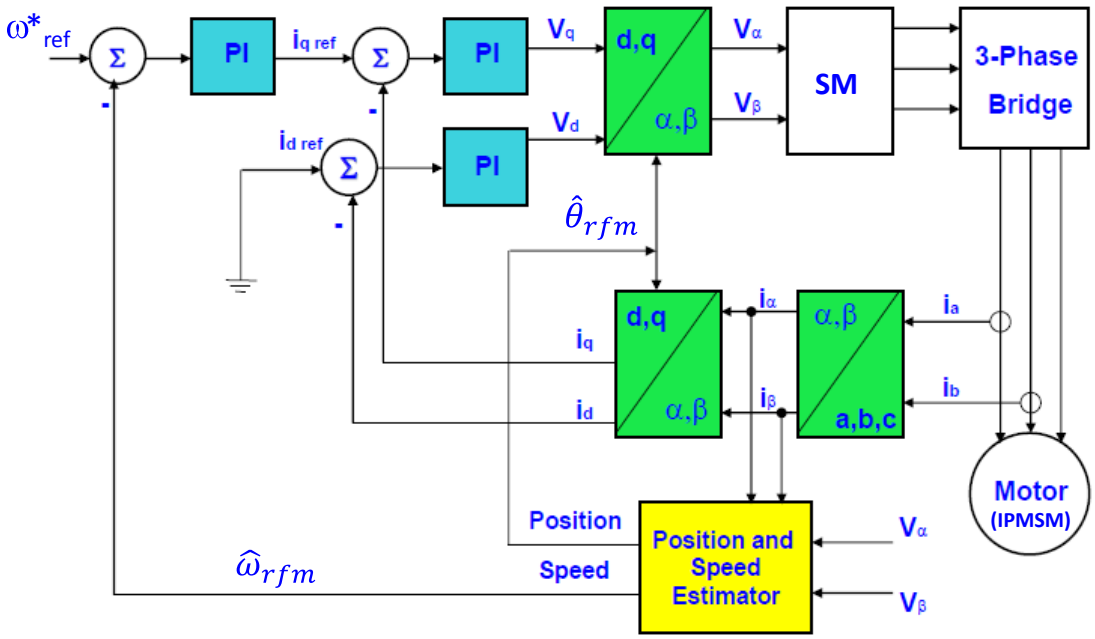

Fig. 1.3 Overall block diagram of a IPMSM drive system using a position and speed estimator.

The entire process with sensorless FOC for IPMSM is illustrated in this block diagram, including coordinate transformations, PI iteration, transforming block and generating PWM. This block diagram also describes the functions required for FOC control. Error signals are formed by I_d, I_q and reference values. The Id reference controls rotor magnetizing flux. The flux vector must be kept in alignment with the rotor magnetic poles at all times so that the motor can produce the maximum torque. This is accomplished by a flux reference of zero. I_d and I_q (representing torque and flux) are only time-invariant under steady-state load conditions. The I_q reference controls the torque output of the motor. The outputs of the PI controllers provide V_d and V_q, which is a voltage vector that is sent to the motor. A new coordinate transformation angle is calculated based on the motor speed, rotor electrical time constant, Id and I_q. The FOC algorithm uses the new angle to place the next voltage vector, to produce an amount of torque needed to keep the rotor spinning. The V_d and V_q output values from the PI controllers are rotated back to the stationary reference frame, using the new angle. This calculation provides quadrature voltage values v_α and v_β. Next, the v_α and v_β values are transformed back to 3-phase values v_a, v_b and vc. The 3-phase voltage values are used to calculate new PWM duty-cycle values that generate the desired voltage vector.

As this block diagram shows, field oriented control block diagrams add a new block to calculate position and speed of the motor. As the yellow block shows, there is no position or speed sensor as input. Current sensors and software voltages are used to estimate position and speed of the motor. I_α and I_β are derived by current measurements from motor windings. v_α and v_β are variables that we calculate during FOC.

These are some applications where PMSM motors are used.
1. In order to boost the efficiency of air conditioning compressors, PMSM motors are used. Also, physical conditions of a compressor, where the motor is flooded in oil, position sensors are not allowed. Sensorless algorithms are required for compressors in general.
2. PMSM are also becoming popular in Direct Drive washing machine due to their torque available at low speed regions. FOC enables better dynamic response in a washing machine without increasing the overall system cost.
3. Refrigerator compressors also require better efficiency and torque performance at low speed. These requirements are covered by PMSM motors as well.
4. Pumps and Air Conditioner compressors in the automotive applications are also transitioning to PMSM motors due to efficiency gains, increased lifetime compared to DC motors, and high torque at low speeds.

1.2.4 Rotor Position Sensorless Vector Control of PMSM Drives

In the vector control scheme, there are three blocks with the rotor position information: 1) calculate i_d and i_q by the Park transformation, 2) calculate v_α and v_β by the inverse Park transformation, and 3) rotor speed calculation. Therefore, the rotor position is indispensable for high-performance space vector control of PMSM drives. Inaccurate rotor position information will not only degrade the control performance but also cause instability in the control system. Electromechanical position sensors, e.g., resolvers, optical encoders, and hall effect sensors are commonly used to obtain rotor position/speed in PMSM drives. The use of these sensors increases the cost, size, weight, and hardware wiring complexity of drive systems. From the viewpoint of system reliability, mounting electromechanical sensors on rotor shafts will degrade mechanical robustness of the electric machines. The electromagnetic interference (EMI) noise in the wiring harness, due to switching events and broken wires, may be fatal to the controller's operation. Moreover, sensors are often subject to high failure rates in harsh environments, such as excessive ambient temperature, super high-speed operation, and other adverse or heavy load conditions. To overcome these drawbacks of using position sensors, quite a lot research effort has gone into the development of sensorless drives that have a comparable dynamic performance with respect to the sensor-based drives during the last decades [14].

1.3 Control fundamentals of PMSMs

In [15], it detects the vibration by the acceleration sensor for SPMSM under torque control and generates a compensation signal by inputting to the repetitive controller. The compensation signal is superimposed to the q-axis current command value, the vibration is suppressed. Moreover, subjected to stability analysis in the vicinity of the operating point using the linear approximation has proposed a repetitive controller parameter automatic adjustment algorithm for stabilizing the system. However, if the sharp resonance occurs in the mechanical system, there are problems such as the inability to learn compensation signal in its vicinity.

Therefore [16], shows that can perform vibration suppression by performing linear interpolation using the compensation signal learned before and after the resonance point even at the resonance point. However, the method of [15] and [16] is in need of two position sensors and acceleration sensors. In addition to the use of these sensors is an increase in cost, problems such as securing of lowering and installation space of the reliability due to noise occurs.

To above-mentioned problems, by applying the method of [15], the vibration suppression control method that does not require a position sensor have been proposed in the position sensorless speed control system of PMSM [17], using the vibration detection sensor (acceleration sensor) generated only the compensation current signal, and generates a polynomial of the compensation current signal in the steady state. Thereafter, by performing feed-forward compensation using the generated compensating current signal is realized the position and acceleration sensorless vibration suppression control. However, still the device itself, such as compressor there is a problem that the application is difficult, such as equipment that becomes a high temperature.

It should be noted that, in the method that has been described so far, the vibration generated due to incomplete motor structure and control system (The frequency of such torque ripple are 6 times, 12 time, and 18 time of the electrical angular speed) of the vibration suppression target. I have been with. On the other hand, such as in the compressor of interest in this study, the vibration caused by the torque ripple of the load side (the electrical angular velocity are 1/3 times, 1/2 times, and 1 time has relatively low order of frequency) is generated.

The compressor, etc. is often operated a long time at a constant rate and do not require a high-speed response. Further, since the vibration of interest in this study is a relatively low frequency, without using the vibration detected by the acceleration sensor, even by using the estimated speed by the observer is believed to be possible vibration suppression.

As a method for compensating for periodic torque ripple without a repetitive controller superposed method using periodic disturbance observer [18], the method using the load torque table [19], and the speed ripple attenuation method was proposed by injecting a compensating sinusoidal *q*-axis current. Then the problem is reduced to select two parameters; phase offset and amplitude. The offset angle is roughly calculated from a zero crossing point of the speed ripple. A searching algorithm which resembles the maximum power point tracking (MPPT) [20] is developed. However, it also requires the data measured by the torque sensor and advance for detecting the torque ripple either approach. Therefore, the technique proposed in this thesis can be said to be superior in terms of the fact that the compensation can be performed without using such a sensor and the data.

1.4 Objectives of the Research

In earlier research, a method to reduce the mechanical vibration due to cogging torque has been proposed, where the vibration has been detected by the acceleration sensor [15] - [17], a compensation signal has been generated using Fourier series expansion and the repetitive controller and vibration suppression control is performed by superimposing the q-axis current command value. However, this method requires the position sensor or an acceleration sensor.

Therefore, the predecessor proposed the position and acceleration sensorless vibration suppression control method [21]. Its effectiveness is shown by simulation. In this approach, the position sensorless method is extended electromotive force observer [22]. Fourier Transform extracts the target frequency vibration components from the estimated speed of the motor to generate compensation signals. These compensation signals are added to q-axes current at last. This method performs vibration suppression by eliminating the torque ripple. As a result, the whole system can achieve vibration suppression control without position and acceleration sensor.

However, the repetitive controller which has been used in the compensation signal generation process in the previous method only has targeted at the desired frequency. Besides that, this controller may have amplified high-frequency components. Therefore, a new vibration suppression control method is proposed instead of the repetitive controller. In this thesis, SCRS(Specific Component Reduction System) is proposed. In SCRS, the target vibration frequency components are extracted by the Fourier series expansion and learned by the integrator to generate a compensation signal for suppression of the vibration estimated from the position information, and therefore it is quite difficult to amplify the noise that is high frequency vibration components included in the estimated speed during the compensation signal generation process. Then, a stability analysis of the

proposed method by a linear approximation is performed to design the most two important parameters in SCRS. The experimental results show the effectiveness of the proposed method.

The main objectives of this research includes:

1. A position/speed estimation scheme and sensorless control for salient-pole PMSMs for medium- and high-speed region applications is developed. The sensorless control systems should be robust to operating conditions and have zero phase lag in both steady-state and transient conditions. In addition, the sensorless control systems should be robust to the variations of machine parameters.

2. An anti-vibration controller derived from the repetitive controller with the EEMF observer, which is hard to amplify high-frequency components is developed. This novel controller is named Specific Component Reduction Controller (SCRC). The SCRC learns the Fourier coefficients extracted by FT. The coefficients are integrated to generate a compensation signal which is exploited to carry out the proper compensation. The analysis is shown to study the stability of the proposed system. But SCRC only aims at one frequency component.

3. The vibration suppression controller named as Multipled Specific Component Reduction Controller(M-SCRC) has been developed, where not only the first-order frequency component, but also the second-order one are involved in the controller. It is shown that SCRC can be taken into practice of multipled components application.

1.5 Thesis Organization

The thesis is organized as follows: This thesis is composed a total of Chapter 8.

Chapter 1 shows the background of this study, the control fundaments of PMSM, the purpose, and objectives of the research**.**

Chapter 2 describes that the voltage equation is a mathematical model of the PMSM to be handled in this study. In addition, the torque pulsation and vibration model is handled in the present study.

Chapter 3 explains the position sensorless control method by the extended induced voltage model and a disturbance observer to be used in the present study.

Chapter 4 describes vibration suppression control method by a repetitive control, which is a conventional one.

Chapter 5 describes vibration suppression control method using the SCRS proposed in this study. In addition, a description is given to explain the position and acceleration sensorless vibration suppression system using the SCRS.

Chapter 6 describes the frame vibration suppression method for a sensorless PMSM-Drive application and showns the stability analysis and experimental results of the proposed method.

In Chapter 7 shows the Simulataneous Vibration Suppression Control for Sensorless PMSM Driven by Utilizing Multiple-Specific Conponent Reduction Control Method.

Chapter 8 describes the conclusions and future challenges of the results obtained in the list of publications.

Reference

[1] S.-K. Sul, *Control of Electric Machine Drive Systems*, 1st Edition, John Wiley & Sons, Inc., Hoboken, New Jersey, 2011.

[2] D. W. Novotny and T. A. Lipo, *Vector Control and Dynamics of AC Drives*, Oxford University Press Inc., New York, 1996.

[3] W. Leonhard, *Control of Electrical Drives*, 3rd Edition, Springer, Berlin, 2001.

[4] D.-H. Lee J.H. Lee J.-W. Ahn, " Mechanical vibration reduction control of two-mass permanent magnet synchronous motor using adaptive notch filter with fast Fourier transform analysis" Published in IET Electric Power Applications,Received on 20th October 2011,Revised on 9th January 2012.

[5] . D. J. Phillips and E. G. Collins, Jr., "Four Experimental Demonstrations of Active Vibration Control for Flexible Structures," Proc. AIAA Guid. Nay. Contr. Conf., pp. 1625-1633, Portland, OR, August 1990.

[6] D. C. Hyland, "An Experimental Testbed for Validation of Control Methodologies in Large Space Optical Structures," in Structural Mechanics of Optical Systems II, pp. 146-155, A. E. Hatheway, Ed., Proceedings of SPIE, Vol. 748, Optoelectronics and Laser Applications Conference, Los Angeles, CA, January 1987.

[7] Muragishi Y. Active damper unit driven by RECIPROCATION MOTOR. J Japan Soc for Precision Eng. 2007;73:414–417.

[8] A. SHIMADA and M. ISHIDA, "Sensorless Suppression Control for Frame Vibration of PMSM" Electrical Engineering in Japan, Vol. 128-D, No. 11, pp. 1246–1253 November 2008.

[9] M. Yimin Gao, and John M. Miller, "Hybrid Electric vehicles: Architecture and Motor drive," *Proceedings of the IEEE*, vol. 95, issue 4, Apr. 2007, pp. 719 – 728.

[10] M. Ehsani, G. Yimin, and S. Gay, "Characterization of electric motor drives for traction applications," *Industrial Electronics Society, 2003. IECON '03. The 29th Annual Conference of the IEEE*, vol. 1, Nov. 2003, pp. 891 – 896.

[11] R. Krishnan, Permanent Magnet Synchronous and Brushless DC motor Drives, 1st Edition, CRC press, Taylor & Francis Group, FL, 2009.

[12] A. Vagati, G. Pellegrino, and P. Guglielmi, "Comparison between SPM and IPM motor drives for EV application," in Proc. International Conference on Electrical Machines, pp. 1-6. 172, Sept. 2010.

[13] A. M. EL-Refaie and T. M. Jahns, "Comparison of synchronous PM machine types for wide constant-power speed range operation," in Proc. IEEE Industry Applications Society Annual Meeting, vol. 2, pp. 1015-1022, Oct. 2005.

[14] M. Pacas, "Sensorless drives in industrial applications," *IEEE Industrial Electronics Magazine*, vol. 5, no.2, pp. 16-23, Jun. 2011.

[15] Hattori, Ishida, Hori:. "Torque vibration suppression control of brushless DC motor according to the repetition control using the Fourier transform", Instrument and Control Society Papers, Vol 36, No. 5, pp.438 / 447, 2000 .
[16] Hattori, Ishida, Hori: "vibration suppression control of PMSM by the parameter automatic adjustment function with repeated control using the Fourier transform", the Institute of Electrical Engineers theory D, vol.121-D, No.3, pp.347-355 , 2001.
[17] Shimada, Kawai, Zankan, road tree, Ishida: "frame vibration suppression control method in sensorless control system of PMSM", the Institute of Electrical Engineers theory D, Vol.128, No.11, pp.1246-1253, 2008.
[18] M. Zhang; Y. Li; T. Zhao; Z. Liu; L. Huang, "A speed fluctuation reduction method for sensorless PMSM-compressor system," in Industrial Electronics Society, 2005. IECON 2005. 31st Annual Conference of IEEE , vol., no., pp.5 pp.-, 6-10 Nov. 2005.
[19] J. Kim; K. Nam, "Speed ripple reduction of PMSM with eccentric load using sinusoidal compensation method," in Power Electronics and ECCE Asia (ICPE & ECCE), 2011 IEEE 8th International Conference on , vol., no., pp.1655-1659, May 30 2011-June 3 2011.
[20] T. Yamaguchi, Y. Tadano, N. Hoshi, “Torque Ripple Suppression Control by Periodic Disturbance Observer with Model Error Correction,” IEEJ Trans., vol.134, no. 2, pp.185-192, 2014.

[21] Kato, Ishida: "vibration suppression control by the estimated velocity pulsation suppression using repetitive control in PMSM position sensorless control system" Institute of Electrical Engineers of motor drive linear drive Joint Study Group, MD-13-62 LD-13-124, pp.115-119, 2013.
[22] Z. Chen, M. Tomita, S. Doki and S. Okuma, ”An Extended Electromotive Force Model for Sensorless Control of Interior Permanent-Magnet Synchronous Motors”, IEEE Trans. IE, Vol.50, No.2, pp.288-295, 2003.

Chapter 2

Basic Characteristics of Permanent Magnet Synchronous Motor (PMSM)[1]

2.1 Mathematical Model of Permanent Magnet Synchronous Motor

The aim of this chapter is to systemically review mathematic models of the two major varieties of permanent-magnet synchronous machines, namely interior PM motors and surface-mounted PM motors, before proceeding to design of the control and observation algorithms for them. Transformations of variables are used to deal with the time-varying
machine inductances, referring to the coefficients of differential equations (e.g., voltage equations) that describe the performance and behavior of the PM motors. Moreover, basic operation principles of PM synchronous machines are discussed whereupon vector control is briefly investigated. All the analysis and control methods presented in later chapters are based on these models.

2.1.1 Structure

Different rotor configurations exist for PMSMs depending on how the magnetics are placed in the rotor [2] and [3]. The two common type, namely, surface magnets type and interior magnets type are shown in Fig. 2.1. In surface magnets type the magnets are mounted on the surface of the rotor, whereas in interior magnets type of the magnets are placed inside the rotor core. Hereinafter the PMSMs with surface magnets configuration are referred to as SPMSMs and PMSMs with interior magnets rotor configuration are referred to as IPMSMs.

The interior magnets type rotor configurations bring saliency characteristics to the machine which is not present in a machine with surface magnets type rotor [4]. As shown in Fig. 1.2 (a) and (b), the magnets flux induced by the magnets defines the rotor director q^r-axis is orthogonally (90 electrical degrees) placed with rotor d^r-axis (Note that for four-pole design this is 45 mechanical degrees as shown in Fig. 1.2 (b). Since the permeability the effective airgap of d^r-axis is increased compared to the q^r-axis. Therefore d^r-axis reluctance inductance is higher than the q^r-axis reluctance. This results in the q^r-axis inductance is higher than the d^r-axis inductance, i.e. $L_d > L_q$, in IPMSMs.

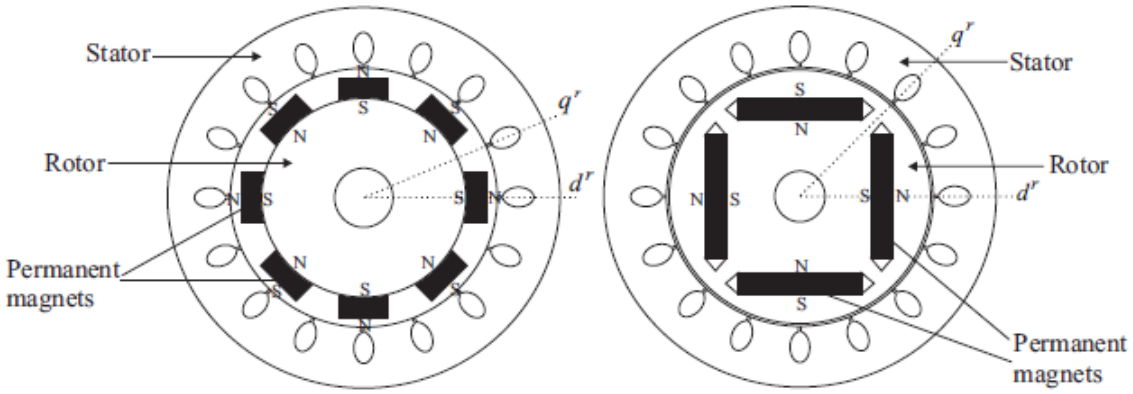

(a) (b)

Fig.2.1 Motor cross sections showing different rotor configurations for PMSMs: (a) Surface magnets type (b) Interior magnets type.

2.1.2 Voltage and current equation and torque equation.

(1) *u*-*v*-*w* coordinate system

In Fig.2.2, idealized three-phase, the dynamic machine model is very simple compared that of a sinusoidal machine. It can be given in the following general from [5]:

$$\begin{bmatrix} v_u \\ v_v \\ v_w \end{bmatrix} = \begin{bmatrix} R_a + pL_a' & -\frac{1}{2}pM_a' & -\frac{1}{2}pM_a' \\ -\frac{1}{2}pM_a' & R_a + pL_a' & -\frac{1}{2}pM_a' \\ -\frac{1}{2}pM_a' & -\frac{1}{2}pM_a' & R_a + pL_a' \end{bmatrix} \begin{bmatrix} i_u \\ i_v \\ i_w \end{bmatrix} + \begin{bmatrix} e_u \\ e_v \\ e_w \end{bmatrix} \quad (2.1\text{-}1)$$

Here, *u-v-w* is three-phase armature L_a = armature winding self inductance, Ra = armature winding resistance, M_a = mutual inductance of the armature wind between phase, *e* = phase EMF, *v* = applied phase voltage, *i* = applied phase current, and *p(d/dt)* = Laplace operator. Since

$$i_a + i_b + i_c = 0 \quad (2.1\text{-}2)$$

That is,

$$Mi_b + Mi_c = -Mi_a \quad (2.1\text{-}3)$$

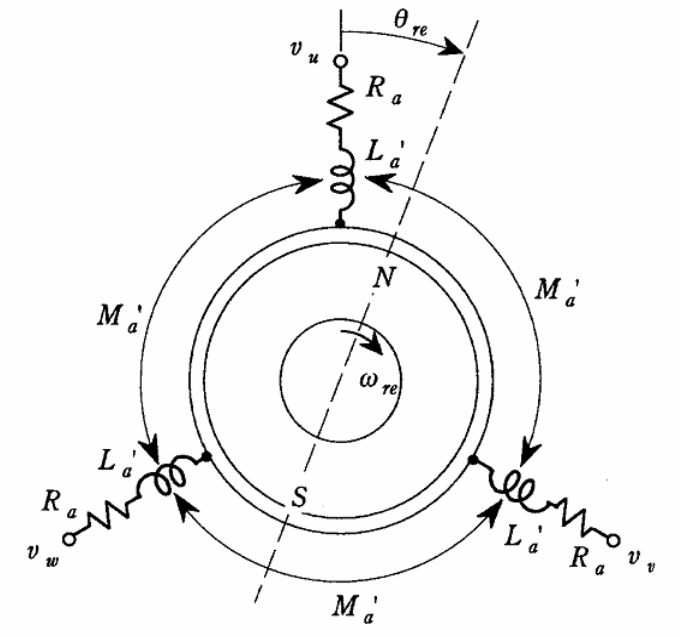

Fig. 2.2 Idealized three-phase, two-pole Synchronous Machine (salient pole).

The magnetic field e_u, e_v, e_w to induce *u, v, w*-phase armature winding flux linkage number of $\emptyset_{fu}$, $\emptyset_{fv}, \emptyset_{fw}$ with the maximum value located at Φ'_f , as follow

$$\begin{aligned}
\phi_{fu} &= \Phi'_f \cos\theta_{re} \\
\phi_{fv} &= \Phi'_f \left(\cos\theta_{re} - \frac{2\pi}{3} \right) \\
\phi_{fw} &= \Phi'_f \left(\cos\theta_{re} + \frac{2\pi}{3} \right)
\end{aligned} \tag{2.2}$$

Here, θ_{re} shows the rotor angle position, and it can be obtained from the integration of the rotor angle speed ω_{re} as given

$$\theta_{re} = \int \omega_{re} dt \tag{2.3}$$

In this case, e_u, e_v, e_w can be given

$$\begin{aligned}
e_u &= p\phi_{fu} = -\omega_{re}\Phi'_f \sin\theta_{re} \\
e_u &= p\phi_{fv} = -\omega_{re}\Phi'_f \sin\left(\theta_{re} - \frac{2\pi}{3} \right) \\
e_u &= p\phi_{fw} = -\omega_{re}\Phi'_f \sin\left(\theta_{re} + \frac{2\pi}{3} \right)
\end{aligned} \tag{2.4}$$

The armature winding, there is also a leakage in the l_a- inductance.

$$L'_a = l_a + M'_a \tag{2.5}$$

Note, the rotation angular speed ω_{rm} (mechanical angle) is calculated from the number pole pairs *Ps* and rotor angle speed ω_{re} can be derived by ω_{re} / P_s .

（2）α-β transformation.

3-phase AC is converted into two-phase alternating current, finds the circuit equation represented by the two-phase alternating current. Fig.2.3 to show such a three-phase alternating current coordinates (*uvw*) 2-phase alternating current coordinates from the system (α-β) by transformation matrix to the system [c], and three-phase AC coordinate system is $vu + vv + vw = 0$, $iu + iv + iw = 0$, assuming that there is not zero-phase-sequence component, can be expressed by

$$[c]=\sqrt{\frac{2}{3}}\begin{bmatrix} 1 & -\frac{1}{2} & -\frac{1}{2} \\ 0 & \frac{\sqrt{3}}{2} & -\frac{\sqrt{3}}{2} \end{bmatrix} \tag{2.6}$$

Eq. (2.1) to represented by the formula, applying to the transformation matrix expressed in eq. (2.6) can be derived, as follow

$$\begin{bmatrix} v_\alpha \\ v_\beta \end{bmatrix}=\begin{bmatrix} R_\alpha + pL_\alpha & 0 \\ 0 & R_\alpha + pL_\alpha \end{bmatrix}\begin{bmatrix} i_\alpha \\ i_\beta \end{bmatrix}+\begin{bmatrix} e_\alpha \\ e_\beta \end{bmatrix} \tag{2.7}$$

Get the circuit equation of. It shows an equivalent circuit in Fig.2.4.

Here, the phase armature voltage v_α, v_β, the phase armature current i_α, i_β, and the permanent magnet field e_α, e_β, the speed electromotive force induced in the phase armature winding, Ra is armature winding resistance, *La* is Electric is a self-inductance of winding. Further Ra are the same as those of the eq. (2.1) equation, *La* is the use small of la (in eq. 2.1), and M'_a also used, as follow

$$L'_a = l_a + \frac{3}{2}M'_a \tag{2.8}$$

The magnetic field e_α, e_β, two orthogonal axes called (α, β) to induce winding flux linkage number of $\emptyset_{f\alpha}$, $\emptyset_{f\beta}$ with the maximum value located at Φ_f, as follow

$$\begin{aligned} \phi_{f\alpha} &= \Phi_f \cos\theta_{re} \\ \phi_{f\beta} &= \Phi_f \sin\theta_{re} \end{aligned} \tag{2.9}$$

In eq. (2.3), the winding flux linkage Φ'_f can be used in term of Φ_f, as expressed by

$$\phi_f = \sqrt{\frac{3}{2}}\Phi'_f \tag{2.10}$$

The back EMF in the stationary α- β frame is derived as follows

$$\begin{aligned} e_\alpha &= p\phi_{f\alpha} = -\omega_{re}\Phi_f \sin\theta_{re} \\ e_\beta &= p\phi_{f\beta} = \omega_{re}\Phi_f \cos\theta_{re} \end{aligned} \tag{2.11}$$

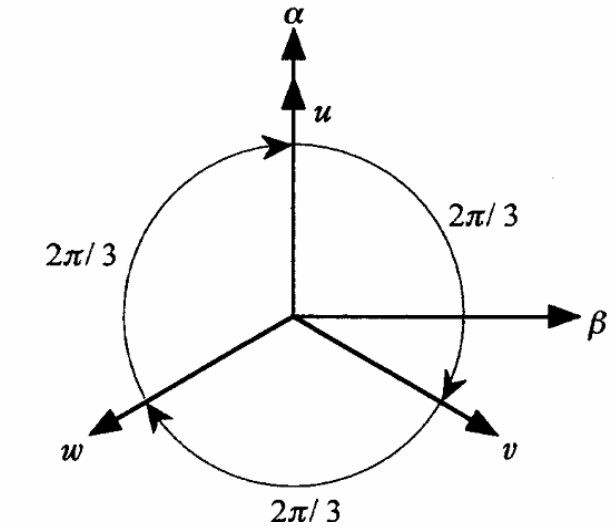

Fig.2.3 Station frame three-phase *u* -*v*-*w* to and two-phase α-β axes transformation.

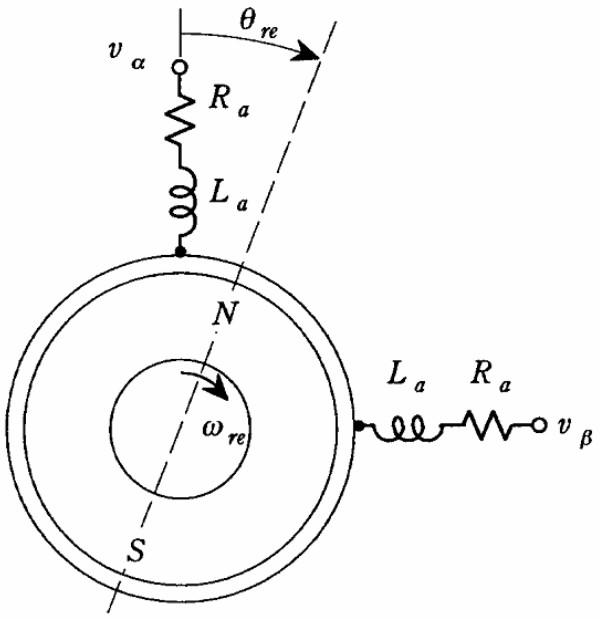

Fig.2.4 Equivalent circuit shown in two-phase α-β axes.

（3） $d-q$ transformation

The motor has a portion of the rotation(rotor) and the fixed portion(stator). Them in the conversion of the d-q transform both to fixed orthogonal coordinate system or orthogonal coordinate system that rotates, the coordinate system is a d-q transform system. q-axis is in the $\pi / 2$ an advanced phase with respect to the d-axis.

For the synchronous motor, d-axis common to take the direction of the magnetic flux formed by the field, the rotating field type synchronous motor provided with this, d-q axes become rotated coordinates.

The Park transformation convert the stationary 2-phase AC current i_α, i_β system into rotating 2-phase current i_d, i_q system, shown in Fig. 2.5

$$[c]=\begin{bmatrix} \cos\theta_{re} & \sin\theta_{re} \\ -\sin\theta_{re} & \cos\theta_{re} \end{bmatrix} \tag{2.12}$$

The transform matrix can be derived by a trigonometric function from Fig. 2.5. The voltage equation in the rotating d-q reference frame is expressed as follow by transforming eq. 2.7, applying the transform matrix represented by (2.12) can be rewritten as follows

$$\begin{bmatrix} v_d \\ v_q \end{bmatrix}=\begin{bmatrix} R_\alpha + pL_\alpha & -\omega_{re}L_a \\ \omega_{re}L_a & R_\alpha + pL_\alpha \end{bmatrix}\begin{bmatrix} i_d \\ i_q \end{bmatrix}+\begin{bmatrix} 0 \\ \omega_{re}\Phi_f \end{bmatrix} \tag{2.13}$$

The second term on the right side of this equation by a permanent magnet field, and the speed electromotive force e_d, e_q represents the to induce the dq-axis armature winding, eq, a e_d=0, $e_q=\omega_{re}\Phi_f$. It shows an equivalent circuit in Fig.2.6. Here, *d, q*-axis armature voltage and *d , q* -axis armature current, Φ_f as same in eq. (2.11) where, *Ra*, *La* in eq. (2.7) is the same as the thing.

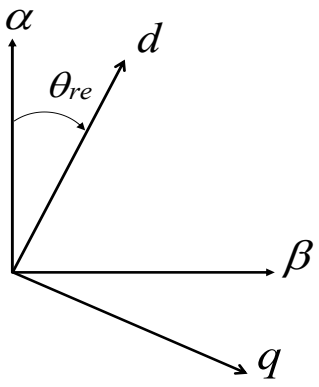

Fig.2.5 2-phase relationship of the AC current coordinate and d-q coordinate.

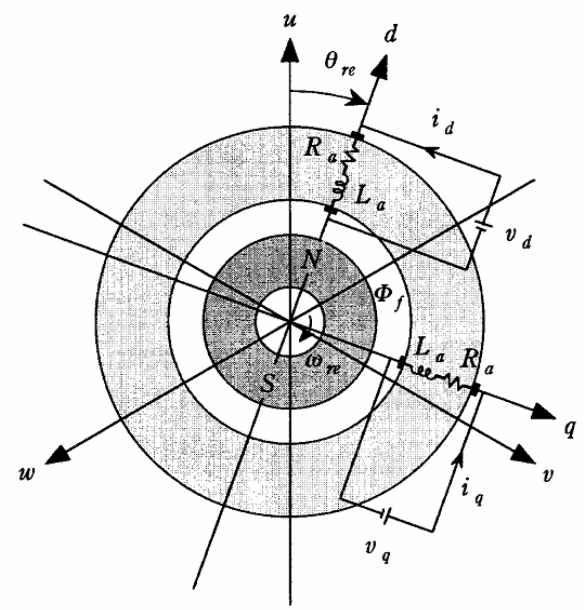

Fig.2.6 General rotating reference frame of d-q coordination

Using an encoder and the inverter is a position detector, *vd, vq* into a direct voltage *and id, iq* also becomes a direct current. It can be handled in two axes direct. Incidentally, in eq. (2.13) where the second term on the right side already by the permanent magnet field, as described, q-axis is a speed electromotive force induced in the armature winding, so the field is in the d-axis. π/ 2 has been induced only to the q-axis advanced, it is a DC voltage.

As an equivalent circuit of SPMSM, it is often used one phase equivalent circuit shown in Fig.2.7. This equivalent circuit applies a three-phase symmetrical voltage in Fig.2.2 is obtained in eq.(2.1). As below, represents one phase when volume flow is three-phase symmetrical current, the circuit equation, as follow

$$v_u = (R_a + pL_a)i_u + e_u \tag{2.14}$$

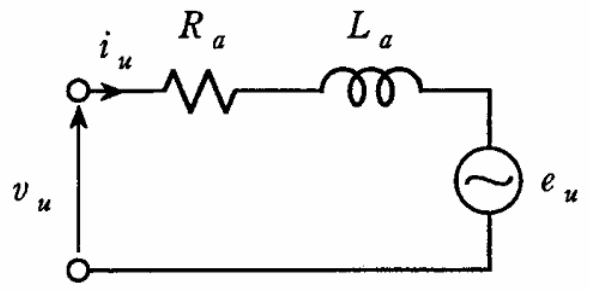

Fig.2.7 Per phase equivalent circuit.

From eq.(2.13), d, q-axis armature inductance is a circuit equation that represents the only equal SPMSM (*Ld* = *Lq* = *La*). But d and q-axis armature inductance are different IPMSM (*Ld* <*Lq*: reverse salient pole) circuit equation also in view, a general PMSM is expressed by

$$\begin{bmatrix} v_d \\ v_q \end{bmatrix} = \begin{bmatrix} R_\alpha + pL_d & -\omega_{re}L_q \\ \omega_{re}L_d & R_\alpha + pL_q \end{bmatrix} \begin{bmatrix} i_d \\ i_q \end{bmatrix} + \begin{bmatrix} 0 \\ \omega_{re}\Phi_f \end{bmatrix} \tag{2.15}$$

In the present study, carried out the construction of a control system based on the voltage equation of eq. (2.15).

（4） Torque equation

Torque T_e of the motor is generated by Fleming left-hand rule. However, the torque applied to the field is a motor torque in the rotating field type. In addition, the IPMSM, for also occur reactance torque due to the saliency of the motor, Torque T_e due to the current of IPMSM is given by

$$\begin{aligned} T_e &= P_S\left(\varphi_d i_q - \varphi_q i_d\right) \\ &= P_S\left\{\left(K_e + L_d i_d\right) i_q - L_q i_q i_d\right\} \\ &= P_S\left\{K_e + \left(L_d - L_q\right) i_d\right\} i_q \end{aligned} \tag{2.16-1}$$

In this case, the vector control (Field Oriented Control: FOC) i_d =0, the motor torque T_e is given as

$$T_e = P_S K_e i_q \tag{2.16-2}$$

where, Ps indicate the number of pole pairs. In the present study directed to a IPMSM under the vector control, the torque equation is assumed to be represented by the formula eq. (2.16 -2).

2.2 Mechanical system model of the compressor dirven by the Permanent Magnet Synchronous Motor(PMSM).

In the previous section, the electrical characteristics of the permanent magnet synchronous motor was described by the voltage equation coordinate transformation viewed from the synchronous rotating coordinate system by the represents. In this section, I describe the frame vibration mechanism generated by the torque pulsations to be handled by the mechanical system model and the present study of the device utilizing the motor.

2.2.1 Generation of the torque ripple

In motor drive application, causes of torque ripple are roughly categorized as either motor-based or load-based one. The factors based on motor include cogging torque and spatial harmonics of flux. They present a high-frequency torque ripple such as 6^{th} harmonics of motor electrical speed.

On the other hand, torque ripples based on load side consist of load torque ripple $\Delta\tau_{Lrip}$ such as load structure. For example, structure of the compressor of an air-conditioner is shown in Fig. 2.8 (a) They generate torque ripples with relatively low-frequency such as *1/P, 2/P, 3/P,...* (*P* = number of motor pole pair).

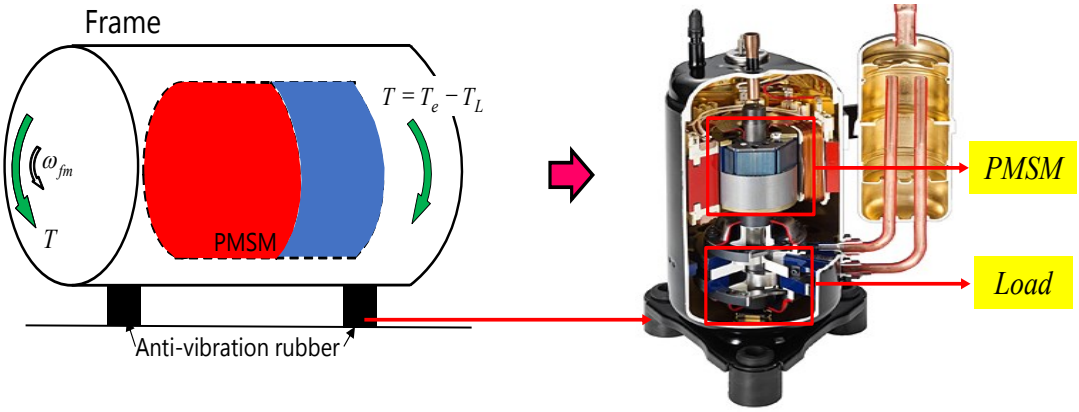

Fig. 2.8(a) The structure of the compressor of an air-conditioner.

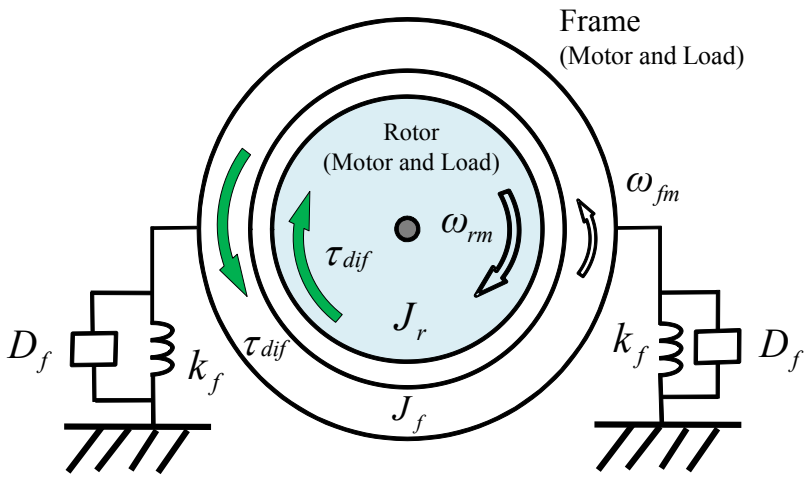

・Rotor

J_r : Inertia

ω_{rm}: Rotor speed

・Frame

J_f : Inertia

D_f : Viscos friction coefficient

k_f : Spring coefficient

ω_{fm}: Frame speed

Fig. 2.8(b) Motor-Load mechanical model around the motor shaft.

2.2.2 Mechanical system model of the rotor frame

Fig. 2.8(b) shows the Motor-Load mechanical model (frame vibration model) of the compressor shown in Fig.2.8(a), where rotor and frame is rotated around the motor shaft while the motor frame is suspended by the rubber etc. Here, J_r is the rotor inertia, J_f is the

frame inertia, D_f is the frame viscous coefficient, K_f is the frame spring coefficient, ω_{rm} is the rotor mechanical speed, ω_{fm} is the frame mechanical speed, θ_{rm} is the rotor mechanical position,and $\omega_{rfm}\ (=\omega_{rm}+\omega_{fm})$ and $\theta_{rfm}\ (=\theta_{rm}+\theta_{fm})$ are the rotor speed and position referred to the frame, respectively. Fig. 2.9 shows the block diagram of the mechanical model shown in Fig.2.8(b), where Ω_{rfm} and Θ_{rfm} are the motor mechanical speed and the motor mechanical position referred to the motor frame, respectively, T_e is the motor driving torque, T_L is the load torque, and T_{dif} is the total torque of motor and load in the complex after Laplace transformation, and s is Laplace operator. The rotation angle of the motor is represented as the phase difference between rotor coordinates and stator coordinates in the model. In general applications, the frame on the stator side is considered as a standstill. However, In our target system, the position detected by a position sensor θ_{rfm} includes the error due to the frame vibration, when the torque ripple causes the fluctuation of frame mechanical speed.

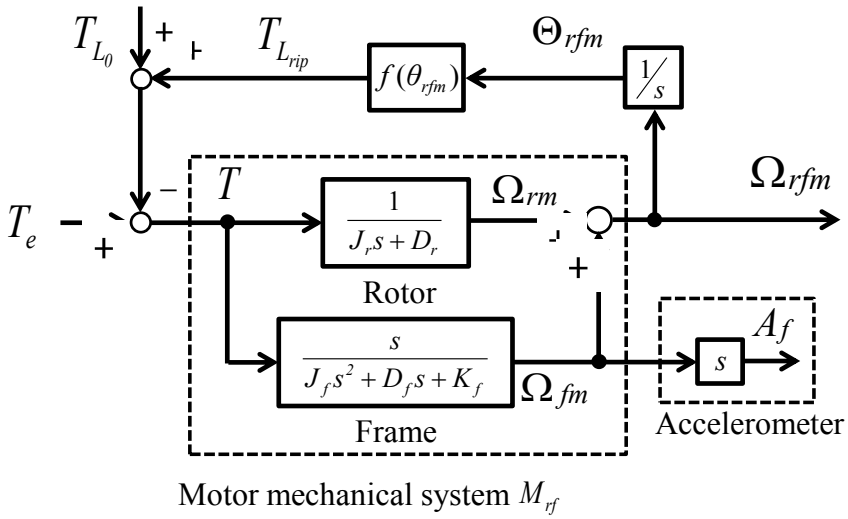

Fig.2.9 Block diagram of Motor-Load mechanical model.

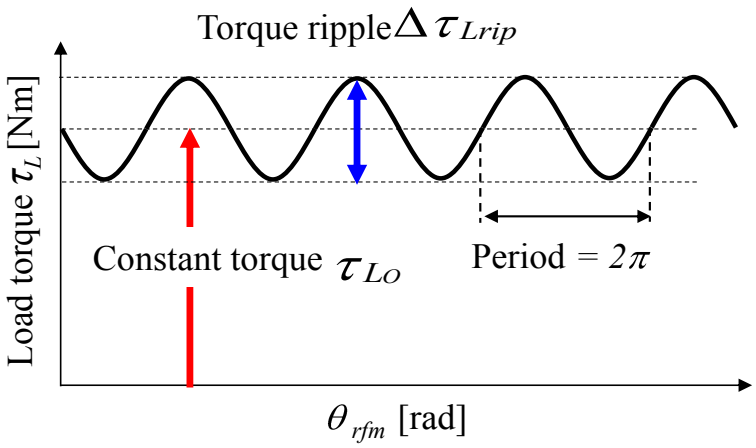

Fig. 2.10 Load torque.

2.2.3 Load torque ripple mechanism

This study targets the system in which the motor and load are integrated, for example, in compressor applications. In this system, the frame vibration is caused by the load torque ripple $\Delta\tau_{Lrip}$ generated by the compressor action which is described as a function of the motor position θ_{rfm}, as in Fig.2.10. The mechanical dynamics of motor frame and rotor in PMSM and load are given as

$$\Omega_{rfm} = M_{rf}(T_e - T_L) = M_{rf}\ T_{dif}. \tag{2.17}$$

$$M_{rf}(s) = \frac{(J_r + J_f)s^2 + D_f s + K_f}{J_r s(J_f s^2 + D_f s + K_f)}. \tag{2.18}$$

$$\tau_L = \tau_{L0} + \Delta\tau_{Lrip}. \tag{2.19}$$

$$\Delta\tau_{Lrip} = A_{\tau Lrip}\sin(n\theta_{rfm}). \tag{2.20}$$

where $A\tau_{Lrip}$ is the amplitude of the load torque ripple, and s is Laplace operator. The load torque ripple $\Delta\tau_{Lrip}$ is the *nth.* order sinusoidal wave. As a result, the periodic speed ripple $\Delta\omega_{rip}$ shown in Fig.2.9 is expressed as

$$\Delta\omega_{rip} = A_{\omega rip}\sin(n\theta_{rfm} + \varphi_{\omega rip}). \tag{2.21}$$

where $A_{\omega rip}$ is the amplitude of the speed ripple, and $\varphi_{\omega rip}$ is the phase of the speed ripple.

Reference

[1] Sugimoto, Koyama, Tamai: "AC theory of the servo system and the design of the actual" comprehensive electronic publishing company, 1990

[2] Thom M. Jahns, Variable Frequency Permanent Magnet AC Machine Drives, Chapter6 in Power Electronics and Variable Frequency Drives, Technology and Applications, B.K. Bose, Ed., IEEE Press, 1997.

[3] Gordon R. Slemon, M. Jahns, Electronic Machine for Drives, Chapter 2 in Power Electronics and Variable Frequency Drives, Technology and Applications, B.K. Bose, Ed., IEEE Press, 1997.

[4] Thomas M. Jahns, Gerald B. Kliman and Thomas W. Neumann, Interior permanent-Magnet Synchronous Motors for Adjustable-speed Drives, IEEE Trans-actions on Industry Applications, Vol. IA-22, No. 4, pp.738-747, July/August 1986.

[5] P. Pillay and R. Krishnan, " Modeling, simulation, and analysis of permanent-magnet motor drives, Part II: the brushless dc motor drive", IEEE trans. On Ind. Appl., vol. 25, pp. 274-279, Mar./Apr.,1989.

Chapter 3

Extended electromotive force voltage model and the position sensorless control by disturbance observer

3.1 Introduction

As discussed before, to drive the IPMSM, coordinate transformation is adopted. In coordinate transformation, the position information is necessary. In normal cases, the encoder has been taken into Field Oriented Control(FOC) system [1]. Since the encoder has some problems, such as making the system more expensive, decrease the robustness etc., a position sensorless control method is necessary.

This research is aimed at low-frequency vibration control. And the compressors almost work at a constant speed for a long times, there is no need to high speed response. For this reason, the position sensorless control method by Extended Electromotive Force Model in [2] has been taken in this research.

In this chapter, the position sensorless control method by Extended Electromotive Force Model is shown. And then, the rotor position and speed estimation method with disturbance observer is proposed. The characteristics of the observer estimation is also shown.

3.2 Mathematical models:the definition of Extended Electromotive Force Model

In this chapter, circuit equations of PMSMs, which are used as mathematical models for sensorless control, are discussed on two kinds of coordinates. These coordinates are the d-q rotating coordinate and the α-β fixed coordinate, which are defined in Fig. 3-1.

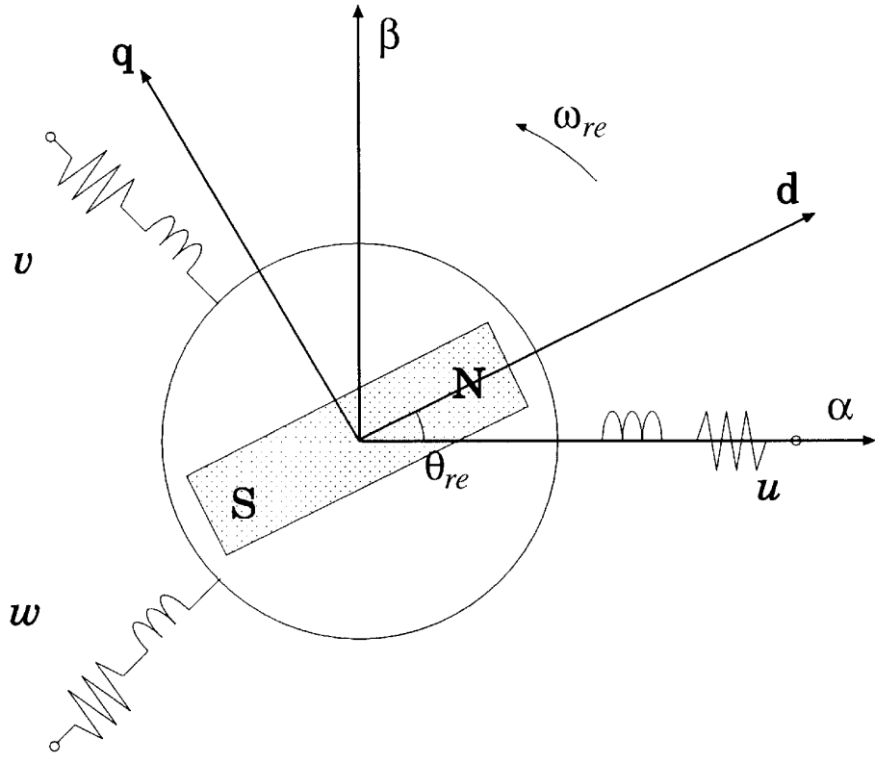

Fig. 3.1 Coordinates of PMSMs.

The voltage equation of PMSM is shown as eq.(3.1).

$$\begin{bmatrix} v_d \\ v_q \end{bmatrix} = \begin{bmatrix} R_\alpha + pL_d & -\omega_{rfe}L_q \\ \omega_{rfe}L_d & R_\alpha + pL_q \end{bmatrix} \begin{bmatrix} i_d \\ i_q \end{bmatrix} + \begin{bmatrix} 0 \\ \omega_{rfe}\Phi_f \end{bmatrix} \tag{3.1}$$

By transforming matrix [c], the voltage equation of PMSM in the statistic axis $(\alpha-\beta)$ is shown as eq. (3.2),

$$\begin{bmatrix} v_\alpha \\ v_\beta \end{bmatrix} = R\begin{bmatrix} i_\alpha \\ i_\beta \end{bmatrix} + pL_0\begin{bmatrix} i_\alpha \\ i_\beta \end{bmatrix} + pL_1\begin{bmatrix} \cos 2\theta_{rfe} & \sin 2\theta_{rfe} \\ \sin 2\theta_{rfe} & -\cos 2\theta_{rfe} \end{bmatrix}\begin{bmatrix} i_\alpha \\ i_\beta \end{bmatrix} + \omega_{rfe}K_E\begin{bmatrix} -\sin\theta_{rfe} \\ \cos\theta_{rfe} \end{bmatrix} \tag{3.2}$$

where,

$L_0=(L_d+L_q)/2$, $L_1=(L_d-L_q)/2$.

In IPMSM, as $L_1 \neq 0$, $2\theta_{rfe}$ in eq. (3.2) is left. And it will make the PMSM voltage equation more complicated. To solve this problem, a voltage equation in [2] with Extended Electromotive Force Model is shown as eq. (3.3).

$$\begin{bmatrix} v_\alpha \\ v_\beta \end{bmatrix} = R\begin{bmatrix} i_\alpha \\ i_\beta \end{bmatrix} + \begin{bmatrix} pL_d & \omega_{rfe}(L_d - L_q) \\ -\omega_{rfe}(L_d - L_q) & pL_d \end{bmatrix}\begin{bmatrix} i_\alpha \\ i_\beta \end{bmatrix} + \left\{(L_d - L_q)\left(\omega_{rfe} i_d - \dot{i}_q\right) + \omega_{rfe} K_E\right\}\begin{bmatrix} -\sin\theta_{rfe} \\ \cos\theta_{rfe} \end{bmatrix} \tag{3.3}$$

Here, the third part in the right the eq. (3.3) is defined as Extended Electromotive Force e. And it is shown as eq. (3.4).

$$e_{\alpha\beta} = \begin{bmatrix} \mathrm{e}_\alpha \\ \mathrm{e}_\beta \end{bmatrix} = \left\{(L_d - L_q)(\omega_{rfe} i_d - \dot{i}_q) + \omega_{rfe} K_E\right\}\begin{bmatrix} -\sin\theta_{rfe} \\ \cos\theta_{rfe} \end{bmatrix} \tag{3.4}$$

With eq. (3.4), the Extended Electromotive Force vector can be got. In this way, the rotor position estimation can also be achieved.

3.3 The position estimation with disturbance observer[2]-[6]

As discussed in the previous section, the Extended Electromotive Force Model includes the position information θ_{re}. In this way, it is possible to get the position information. In this section, the explain of the disturbance observer with the Extended Electromotive Force will be given. And then, the pole design and estimated characteristics of disturbance observer will be shown.

3.3.1 Linear state equation

From the new model of (3.3), the IPMSM can be described by a linear state equation as (3.5). Here, the state variables are stator current i and EEMF e. The system's input is the stator voltage v and output is the stator current i. Assuming that the electrical system's

time constant is smaller enough than the mechanical one, the velocity ω_{rfe} is regarded as a constant parameter

$$\frac{d}{dt}\begin{bmatrix} i_{\alpha\beta} \\ e_{\alpha\beta} \end{bmatrix} = \begin{bmatrix} A_{11} & A_{12} \\ 0 & A_{22} \end{bmatrix}\begin{bmatrix} i_{\alpha\beta} \\ e_{\alpha\beta} \end{bmatrix} + \begin{bmatrix} B_1 \\ 0 \end{bmatrix} v_{\alpha\beta} + \begin{bmatrix} 0 \\ W \end{bmatrix}$$
$$i_{\alpha\beta} = C \cdot \begin{bmatrix} i_{\alpha\beta} \\ e_{\alpha\beta} \end{bmatrix} \tag{3.5}$$

where

$$v_{\alpha\beta} = \begin{bmatrix} v_\alpha & v_\beta \end{bmatrix}^T$$
$$i_{\alpha\beta} = \begin{bmatrix} i_\alpha & i_\beta \end{bmatrix}^T$$
$$e_{\alpha\beta} = \begin{bmatrix} e_\alpha & e_\beta \end{bmatrix}^T$$
$$A_{11} = -(\frac{R}{L_d})I + \{\omega_{rfe}(\frac{L_d - L_q)}{L_d}\}J$$
$$A_{12} = (-\frac{1}{L_d})I$$
$$A_{22} = \omega_{rfe} J$$
$$B_1 = (\frac{1}{L_d})I$$
$$C = \begin{bmatrix} I & 0 \end{bmatrix}$$
$$W = (L_d - L_q)(\omega_{rfe}\dot{i}_d - \ddot{i}_q) + ((L_d - L_q)i_d\dot{\omega}_{rfe} + \dot{\omega}_{rfe}k_e)\begin{bmatrix} -\sin\theta_{rfe} \\ \cos\theta_{rfe} \end{bmatrix}$$
$$= (L_d - L_q)(\omega_{rfe}\dot{i}_d - \ddot{i}_q) + \dot{\omega}_{rfe}(k_e + (L_d - L_q)i_d)\begin{bmatrix} -\sin\theta_{rfe} \\ \cos\theta_{rfe} \end{bmatrix}$$
$$I = \begin{pmatrix} 1 & 0 \\ 0 & 1 \end{pmatrix}$$
$$J = \begin{pmatrix} 0 & -1 \\ 1 & 0 \end{pmatrix}.$$

The output equation is shown as eq. (3.6).

$$i_{\alpha\beta} = \begin{bmatrix} I & 0 \end{bmatrix}\begin{bmatrix} i_{\alpha\beta} \\ e_{\alpha\beta} \end{bmatrix} \tag{3.6}$$

The W term in (3.5) is a linearization error. This term appears only when i_d or i_q is changing. However, under the velocity control this happens in a very short time because

of the high response of the current control loop. Besides, the proposed disturbance observer has an embedded low-pass filter which can cut off the effect of W.

3.3.2 Configuration of the disturbance observer

To get the Extended Electromotive Force, the minimum dimension observer with the linear equation eq. (3.5) has been structured.

$$\begin{aligned}\dot{\hat{i}}_{\alpha\beta} &= A_{11} i\alpha\beta + A_{12}\hat{e}_{\alpha\beta} + B_1 v_{\alpha\beta} \\ \dot{\hat{e}}_{\alpha\beta} &= A_{22}\dot{\hat{e}}_{\alpha\beta} + G(\dot{\hat{i}}_{\alpha\beta} - \dot{i}_{\alpha\beta}) \\ &= A_{11}G i_{\alpha\beta} + (A_{12}G + A_{22})\hat{e}_{\alpha\beta} + B_1 G v_{\alpha\beta} - G\dot{i}_{\alpha\beta}\end{aligned} \tag{3.7}$$

Here, " ^ " is the estimation value and G is the observer gain, which is $G = g_1 I + g_2 J$ feedback gain. In eq. (3.7), the current differential $\dot{i}$ is also included. The current detected by the current sensor is directly derivative. To avoid the enlargement of the high-frequency noise, the intermediate variable ξ has been used in the real application.

$$\begin{aligned}\xi &= \hat{e}_{\alpha\beta} + G i_{\alpha\beta} \\ \dot{\xi} &= \dot{\hat{e}}_{\alpha\beta} + G\dot{i}_{\alpha\beta}\end{aligned} \tag{3.8}$$

Take eq. (3.8) into eq. (3.7), eq. (3.9) can be got.

$$\begin{aligned}\dot{\xi} &= (A_{12}G + A_{22})\xi + B_1 G v_{\alpha\beta} + G(A_{11}I - A_{12}G - A_{22}) i_{\alpha\beta} \\ \hat{e}_{\alpha\beta} &= \xi - G i_{\alpha\beta}\end{aligned} \tag{3.9}$$

Eq. (3.9) is the same as eq. (3.7) as the construction of disturbance observer. In a real application, eq. (3.9) is used to calculate the Extended Electromotive Force $\hat{e}$.

3.3.3 The pole arrangement and estimation characteristics of disturbance observer

The Extended Electromotive Force error is defined as $\varepsilon = \hat{e} - e$. With eq. (3.5) and eq. (3.6), eq. (3.10) is got.

$$\begin{aligned} \dot{\varepsilon} &= \dot{\hat{e}}_{\alpha\beta} - \dot{e}_{\alpha\beta} = (A_{22} + A_{12}G)\varepsilon \\ &= \left\{ -\frac{g_1}{L_d} I + \left(\omega_{rfe} - \frac{g_2}{L_d} \right) J \right\} \varepsilon \end{aligned} \tag{3.10}$$

Here, the poles of the observer are arranged as $-\alpha I + \beta J$ and is shown in Fig. 3.1. As a result, eq. (3.11) has been achieved.

$$\dot{\varepsilon} = \dot{\hat{e}}_{\alpha\beta} - \dot{e}_{\alpha\beta} = (-\alpha I + \beta J)\varepsilon \tag{3.11}$$

In this way, the gain of the observer is shown as the following equation.

$$\begin{aligned} g_1 &= \alpha L_d \\ g_2 &= (\omega_{re} - \beta) L_d \end{aligned} \tag{3.12}$$

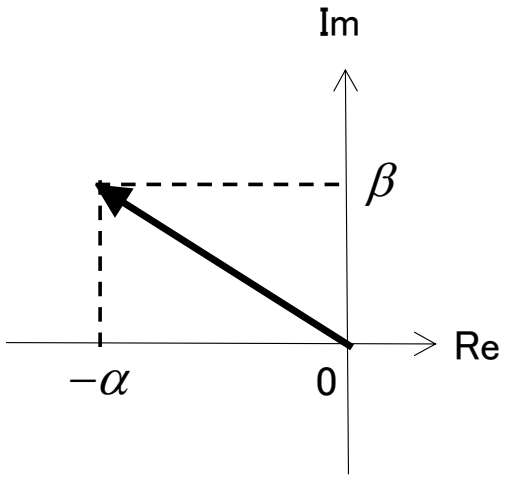

Fig.3.2 The poles arrangement of observer.

To keep the observer stable, $\alpha > 0$, and the poles must be arranged in the left part in Fig. 3.2. To achieve the observer gain like eq. (3.12), the transfer function $F_{\alpha\beta}$(s) related to the real Extended Electromotive Force $e_{\alpha\beta}$ and estimated Extended Electromotive Force $\hat{e}_{\alpha\beta}$ is shown as eq. (3.13).

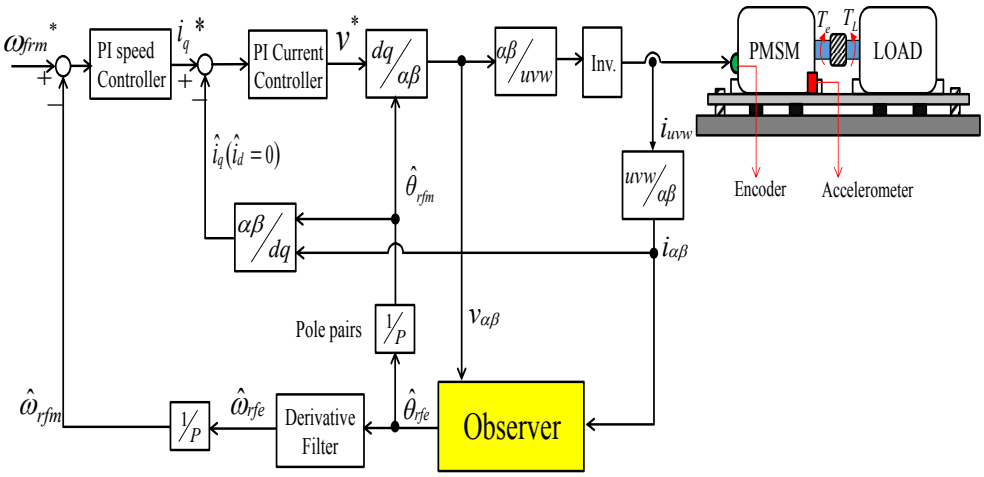

Fig.3.3(a) Position sensorless speed control system of PMSM.

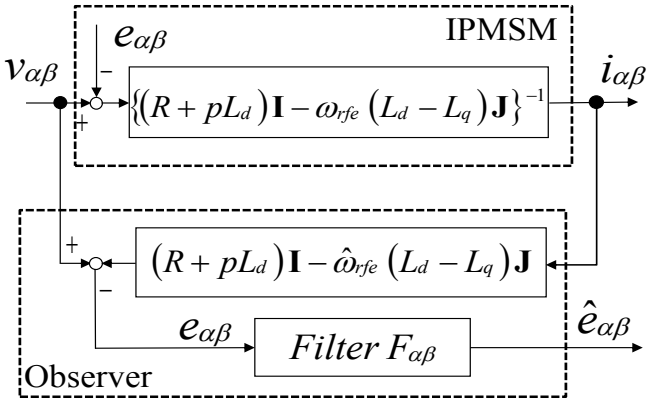

Fig.3.3(b) The construction of disturbance observer EEMF.

$$\hat{e}_{\alpha\beta} = F_{\alpha\beta} e_{\alpha\beta}.$$
$$;F_{\alpha\beta} = \frac{\alpha I - \beta J + \omega_{rfe} J}{(p+\alpha)^2 + \beta^2}\{(p+\alpha)I + \beta J\} \quad (3.13)$$

Fig. 3.3(a) shows the position sensorless speed control system of PMSM using the position observer shown in Fig. 3.3(b) which includes the filter $F_{\alpha\beta}$ to remove noise caused by modeling errors, arrange the pole $\beta = \omega_{rfe}$, The filter characteristics is given as

$$\hat{e}_{\alpha\beta} = \alpha I\{(p+\alpha)I - \omega_{rfm}J\}^{-1} e_{\alpha\beta} = F_{\alpha\beta} e_{\alpha\beta}, \tag{3.14-1}$$

where

$$F_{\alpha\beta} = \alpha I\{(p+\alpha)I - \omega_{rfe}J\}^{-1}. \tag{3.14-2}$$

3.3.4 Construction of Position Sensorless Control System.

This paper utilizes the Extended Electromotive Force (EEMF) observer as a position estimator to construct the sensorless control system [2]. The voltage equation for IPMSM on the stator frame coordinate (α-β axis) is given by

$$v_{\alpha\beta} = \{(R + pL_d)I - \omega_{rfe}(L_d - L_q)J\} i_{\alpha\beta} + e_{\alpha\beta}. \tag{3.15-1}$$

$$e_{\alpha\beta} = \{(L_d - L_q)(\omega_{rfe} i_d - p i_q) + \omega_{rfe} K_e\} J\varepsilon^{J\theta_{rfe}}, \tag{3.15-2}$$

where

$$\varepsilon^{J\theta_{rfe}} \equiv \begin{bmatrix} \cos\theta_{rfe} & -\sin\theta_{rfe} \\ \sin\theta_{rfe} & \cos\theta_{rfe} \end{bmatrix} ; \omega_{rfe} = \frac{d\theta_{rfe}}{dt}. \tag{3.15.3}$$

where eq. (3.15-2) is defined as EEMF $\boldsymbol{e_{\alpha\beta}} = [e_\alpha \ \ e_\beta]^T$. In eq. (3.15-1), v_α and v_β are the voltages on α-β axis, i_α and i_β are the currents on α-β axis, R is the stator resistance, L_d and L_q are the inductances on d-q axis, and p is the differential operator. Since EEMF has information on the real motor position θ_{rfm}, the estimated motor position $\hat{\theta}_{rfm}$ is obtained by EEMF observer shown in Fig. 3.2 and eq. (6-16-1) and (6-18-2).

$$\theta_{rfm} = \frac{1}{P}\arctan\left(-\frac{e_\alpha}{e_\beta}\right), \tag{3.16-1}$$

where

$$I = \begin{bmatrix} 1 & 0 \\ 0 & 1 \end{bmatrix}, \ J = \begin{bmatrix} 0 & -1 \\ 1 & 0 \end{bmatrix}. \tag{3.16-2}$$

Fig. 3.2 shows the observer which includes the filter $F_{\alpha\beta}$ to remove noise caused by modeling errors. The filter characteristics is given as

$$\hat{e}_{\alpha\beta} = \alpha I\{(p+\alpha)I - \omega_{rfm}J\}^{-1} e_{\alpha\beta} = F_{\alpha\beta} e_{\alpha\beta}, \tag{3.17-1}$$

where

$$F_{\alpha\beta} = \alpha I\{(p+\alpha)I - \omega_{rfe}J\}^{-1}. \tag{3.17-2}$$

and -α is the designed real axis pole of EEMF.

$$\hat{\theta}_{rfe} = \arctan\left(-\frac{\hat{e}_\alpha}{\hat{e}_\beta}\right). \tag{3.18-1}$$

$$\hat{\theta}_{rfm} = \frac{1}{P}\arctan\left(-\frac{\hat{e}_\alpha}{\hat{e}_\beta}\right) = \frac{\hat{\theta}_{rfe}}{P}. \tag{3.18-2}$$

Thus, $\hat{e}_{\alpha\beta}$ is estimated by the EEMF observer.

The estimated speed $\hat{\omega}_{rfm}$ is obtained with the derivative filter as follows:

$$\hat{\omega}_{rfm} = \frac{p}{\tau p + 1}\hat{\theta}_{rfm}. \tag{3.18-3}$$

where τ is a time constant of the derivative filter.

3.4 The observer for estimating *d-q* axis component of EEMF

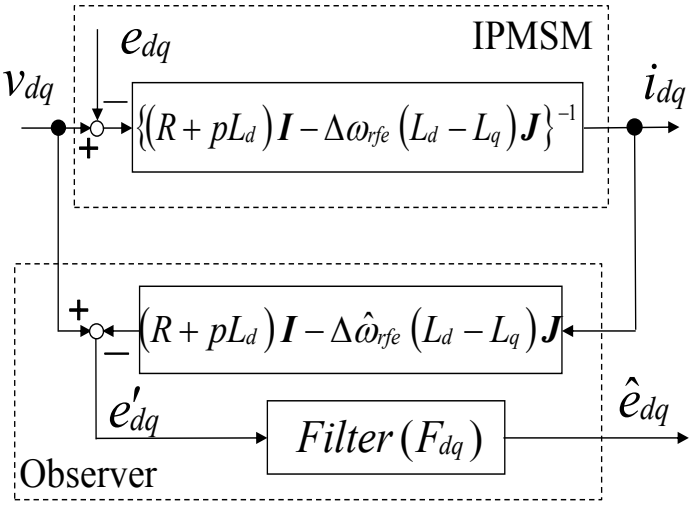

Fig. 3.4 The observer for estimating *d-q* axis component of EEMF.

Fig. 3.4 shows the observer in *d-q* axes, the model in the *d-q* axes is obtained by transforming eq. (3.15-1) and (3.15-2). Considering eq. (3.19-1) into *d-q* axes, the voltage equation and the EMF equation can be shown as follows

$$\varepsilon^{J\Delta\bar{\omega}_{rfe}t} \equiv \begin{bmatrix} \cos\Delta\bar{\omega}_{rfe}t & -\sin\Delta\bar{\omega}_{rfe}t \\ \sin\Delta\bar{\omega}_{rfe}t & \cos\Delta\bar{\omega}_{rfe}t \end{bmatrix}; \Delta\bar{\theta}_{rfe} = \Delta\bar{\omega}_{rfe}t \tag{3.19-1}$$

$$v_{dq} = \{(R + pL_d)I - \Delta\omega_{rfe}(L_d - L_q)J\}i_{dq} + e_{dq}, \tag{3.19-2}$$

$$e_{dq} = \{(L_d - L_q)(\omega_{rfe}i_d - pi_q) + \omega_{rfe}K_e\}J\varepsilon^{J\,\Delta\bar{\omega}_{rfe}t)}.$$

$$v_{dq} = \{(R + pL_d)I - \Delta\hat{\omega}_{rfe}(L_d - L_q)J\}i_{dq} + e'_{dq}. \tag{3.19-3}$$

From eq. (3.19-2) and eq. (3.19-3) as flowing equation is derived

$$e'_{dq} = (\Delta\hat{\omega}_{rfe} - \Delta\omega_{rfe})(L_d - L_q)Ji_{dq} + e_{dq}. \tag{3.19-4}$$

Because in eq.(3.19-4), $\Delta\hat{\omega}_{rfe}$ includes high -frequency noise due to imperfection of motor model, which means e'_{dq} will not be equal to e_{dq}, the filter F_{dq} is applied to observer. As the a result, high-frequency noise of $\Delta\hat{\omega}_{rfe}$ will be reduced, which means $e'_{dq} \cong e_{dq}$.

The position error $\delta\theta_{rfe} = \theta_{rfe} - \bar{\omega}_{rfe}t$ (where $\bar{\omega}_{rfe}$ is the speed average of ω_{rfe}, $\bar{\omega}_{rfe} = \frac{1}{T_r}\int_{ta}^{ta+T_r}\omega_{rfe}dt$, t_a is arbitrary time in one period T_r, and $\bar{\theta}_{rfe} = \bar{\omega}_{rfe}t$) by torque ripple ΔT_{Lrip} is given as

$$\delta\theta_{rfe} = \arctan\left(-\frac{e_d}{e_q}\right) = \arctan(-\xi). \tag{3.20-1}$$

$$\Delta(\delta\theta_{rfe}) = \left(\arctan(-\xi)\right)'\Delta\xi = \frac{1}{1+\xi^2}\Delta\xi;$$

$$\Delta\xi = \frac{e_{qo}\Delta e_d - e_{do}\Delta e_q}{e_{qo}^{\,2}}. \tag{3.20-2}$$

$$= \frac{e_{qo}\Delta e_d - e_{do}\Delta e_q}{e_{do}^{\,2} + e_{qo}^{\,2}} = K_d\Delta e_d - K_q\Delta e_q.$$

In the same way,

$$\Delta(\delta\hat{\theta}_{rfe}) = \frac{\hat{e}_{qo}\Delta\hat{e}_d - \hat{e}_{do}\Delta\hat{e}_q}{\hat{e}_{do}^{\,2} + \hat{e}_{qo}^{\,2}} = \hat{K}_d\Delta\hat{e}_d - \hat{K}_q\Delta\hat{e}_q. \tag{3.20-3}$$

where θ_{rfe} and $\hat{\theta}_{rfe}$ are the real position and estimated position by providing the perturbation, respectively.

Assuming that at the steady state operation point estimated on *d-q axis* coincides with the real *d-q axis*, eq. (3.21-1) can be got. As a result, eq.(3.21-2) can be given

$$\hat{e}_{do} = e_{do},\ \hat{e}_{qo} = e_{qo}. \tag{3.21-1}$$

$$\hat{K}_d = K_d,\ \hat{K}_q = K_q. \tag{3.21-2}$$

From the eq. (3.14-1), and with the eq.(3.16-2), the filter in the rotation coordinate (*d-q* axis) is given by

$$\varepsilon^{-J\bar{\omega}_{rfe}t}\{(p+\alpha)I - \bar{\omega}_{rfe}J\}\varepsilon^{J\bar{\omega}_{rfe}t}\varepsilon^{-J\bar{\omega}_{rfe}t}\hat{e}_{\alpha\beta} = \varepsilon^{-J\bar{\omega}_{rfe}t}\alpha I e_{\alpha\beta}. \quad (\text{3-22-1})$$

$$\varepsilon^{-J\bar{\omega}_{rfe}t}\{\bar{\omega}_{rfe}J + (p+\alpha)I - \bar{\omega}_{rfe}J\}\varepsilon^{J\bar{\omega}_{rfe}t}\hat{e}_{dq} = \alpha I e_{dq}. \tag{3-22-2}$$

Where $e^{J\bar{\omega}_{rfe}t}$ is rotation vector. As mentioned above, the vibration of $\Delta\omega_{rfe} = \omega_{rfe} - \bar{\omega}_{rfe}$ is very small, the rotation vector can also be used.

The estimated back EMF from eq.(3.22-2) is shown as

$$\begin{aligned}\begin{bmatrix}\hat{e}_d\\ \hat{e}_q\end{bmatrix} &= I\hat{e}_{dq} = \frac{\alpha}{(p+\alpha)}Ie_{dq} = \frac{\alpha}{(p+\alpha)}\begin{bmatrix}e_d\\ e_q\end{bmatrix}\\ &= F_{dq}\begin{bmatrix}e_d\\ e_q\end{bmatrix}.\end{aligned} \tag{3-22.3}$$

$$F_{dq} = \frac{\alpha}{p+\alpha}. \tag{3.22-4}$$

The giving perturbation to the eq. (6.22-3), eq. (3.23) is driven.

$$\begin{bmatrix}\Delta\hat{e}_d\\ \Delta\hat{e}_q\end{bmatrix} = \frac{\alpha}{p+\alpha}\begin{bmatrix}\Delta e'_d\\ \Delta e'_q\end{bmatrix} \cong \frac{\alpha}{p+\alpha}\begin{bmatrix}\Delta e_d\\ \Delta e_q\end{bmatrix}. \tag{3.23}$$

From eq. (3.20-2), (3.20-3), (3.21-1), (3.21-2) and (3.23), the relationship between real position and estimated one is given as

$$\frac{\Delta\hat{\theta}_{rfe}}{\Delta\theta_{rfe}} = \frac{P\Delta\hat{\theta}_{rfm}}{P\Delta\theta_{rfm}} = \frac{\alpha}{p+\alpha}. \tag{3.24}$$

Assuming that : the position angle error $\delta\theta_{rfm} = \hat{\theta}_{rfm} - \theta_{rfm}$ is sufficiently small ($cos\delta\theta_{rfm} \cong 1$); the current controller on $\hat{d}$-$\hat{q}$ axis is performed as an ideal state because current controller loop gain is high enough when the SCRC is operated in the relatively low frequency region; and $\hat{\imath}_d = 0$, the motor torque T_e is given as eq. (3.25) where $\hat{\imath}_q$ is the current on the estimated q-axis calculated by $\hat{\theta}_{rfm}$. As a result, the relationship between the real speed and the estimated speed is given as the first-order low-pass filter shown in eq. (3.22-4).

$$T_e = PK_{ef}i_q = PK_e\hat{i}_q \cos\delta\theta_{rfm} \cong PK_e\hat{i}_q \cong PK_e i_q^{ref} \tag{3.25}$$

References

[1] D. W. Novotny and T. A. Lipo, " Vector Control and Dynamics of AC Drives" , publications in the United States by Oxford University Press Inc. New York, 1996.

[2] Z. Chen, M. Tomita, S. Doki, and S. Okuma, "An extended electromotive force model for sensorless control of interior permanent magnet synchronous motors," IEEE Trans. Ind. Electron., vol. 50, no. 2, pp. 288–295, Apr 2003.

[3] S. Ostlund and M. Brokemper, "Sensorless rotor-position detection from zero to rated speed for an integrated pm synchronous motor drive," *IEEE Trans. Ind. Applicat.*, vol. 32, pp. 1158–1165, Sept./Oct. 1996.

[4] M. J. Corley and R. D. Lorenz, "Rotor position and velocity estimation for a salient-pole permanent magnet synchronous machine at standstill and high speeds," *IEEE Trans. Ind. Applicat.*, vol. 34, pp. 784–789, July/Aug. 1998.

[5] M. J. Corley and R. D. Lorenz, "Rotor position and velocity estimation for a salient-pole permanent magnet synchronous machine at standstill and high speeds," *IEEE Trans. Ind. Applicat.*, vol. 34, pp. 784–789, July/Aug. 1998.

[6] Z. Chen, M. Tomita, S. Doki, and S. Okuma, "The sensorless position estimation of salient-pole brushless dc motors and its stability," in *1998 Nat. Conv. Rec. IEEJ-IAS*, vol. I, Aug. 1998, pp. 179–183.

Chapter 4

Vibration suppression control by the repetitive control (the conventional method) [2] - [5]

The repetitive control is excellent in the learning ability of the periodic signal generation and removal. Moreover, learning control method that can be relatively easy to implement is a repetitive control. In this section, we discuss the repetition control used in the conventional study.

In section 4.1, as a characteristic of the repetitive control system, the basic operation and the frequency response characteristic of the repetitive compensator iis described. In section 4.2, as a stabilizing method to stabilize the repetitive control system, a time lead compensator, is introduce incorporating repeatedly control with the Fourier Transformation expansion processing. Then, taken up the basic repetitive control system, the stability of the vibration suppression control system is dicussed. In section 4.3, actually, when implementing such as in the DSP, we describe the algorithm of repetitive control algorithm and Fourier series expansion process in the discrete-time system is described. In section 4.4, the vibration suppression system in the conventional method will be briefly described on the figures.

4.1 Basic characteristics of the repetitive control system

The repetition control is a control system incorporating a repetitive compensator, a servo system for the purpose of highly accurate tracking of the target input for any period T_r (feedback system). In order to follow without any steady-state error in the cyclic target, the input is prerequisite to contain generation model of the target signal within the closed loop based on an internal model principle. Periodic function generation mechanism of period T_r with respect to the target input of the period T_r is realized by utilizing the dead time element $e^{-s\,Tr}$. If you give a periodic function of any cycle T_r to the system, including

the dead time element $e^{-s\,Tr}$, a periodic function generator, which is repeatedly output for each period Tr. It shows a block diagram of a repetitive control system to Fig.4.1. In the basic configuration of the repetitive control system shown in Fig.4.1, the repetitive compensator has a relatively large dead time T_r as compared to a delay of the control target, the compensator is realized to satisfy the internal model principle by utilizing dead time element $e^{-s\,Tr}$. The transfer function of the repetition compensator is given by (4.1). In addition, it shows the basic operating principle diagram Fig.4.2.

$$G_r(s) = \frac{e^{-sT_r}}{1-e^{-sT_r}} = \frac{1}{e^{-sT_r}-1} \tag{4.1}$$

The internal model principle [5] states that for asymptotically tracking a reference command by the output of a closed-loop system, a realization (model) of the disturbance/reference generating system should be included in the feedback loop. As a well-known example, signals with a DC (ω=0) content can be modeled using an integrator, and the inclusion of integral action in the feedback controller prevents steady-state errors for constant references and disturbances. A discrete time integrator is a positive feedback over one delay, implying that one memory location is used to store the integral value. With zero input the integral value updates itself by the positive feedback loop.

Similarly, for periodic signals, a memory loop can be used which generates an output at frequencies $k\omega_r$, with k integer and ω_r the period frequency. In a memory loop, a signal with period $T_r=2\pi/\omega_r$ is stored in a FIFO buffer (first in/first out). Depending on T_r and the sampling frequency a number of memory locations are needed. If a positive feedback is put over this FIFO buffer, in the steady state no input is needed to generate an output with period time T_r. Such a periodic signal has a discrete frequency spectrum with peaks at $\omega=k\omega_r$. A block diagram of a memory-loop with period time T_r is shown in Fig. 4.2 (a).

The repetitive compensator, a continuous system is a compensator adding the input to the delay by the period T_r of input-output, having a fundamental wave and memory properties with respect to the harmonic components of the cycle T_r. For example, as shown in Fig. 4.2 (b), when a sine wave input of one period of the cycle T_r, and the output y is outputted with a delay period T_r.

Bode diagram of the open loop of repetitive compensator shown in Fig.4.3. From Fig.4.3, the period nT_r the gain of the frequency component of (n = 1,2,3, ...) can set to infinity, can be superior steady-state characteristic. That is an input for a frequency

component of the periodic nT_r, can make the difference to zero. The robustness is ensured against external disturbance having a frequency component of the periodic nT_r.

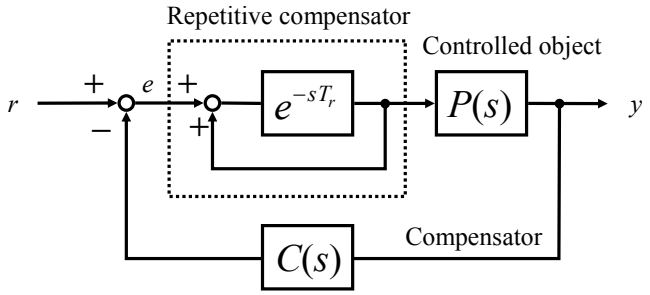

Fig.4.1 Basic configuration of the repetitive control system.

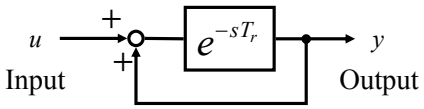

(a) Block diagram of the repetitive compensator[5].

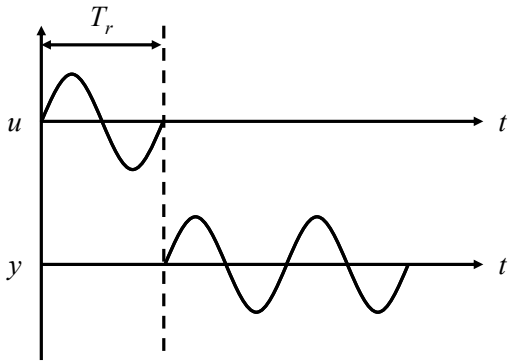

(b) Input and output characteristics of the repetitive compensator.

Fig.4.2 The basic operating principle diagram of the repetitive compensator.

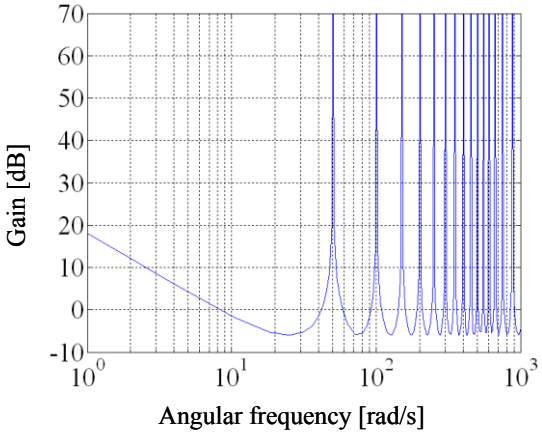

Fig. 4.3 Bode diagram of the repetitive compensator.

4.2 Stabilization technique of the repetitive control system

In the repetitive control system, repetitive compensator has a larger dead time element T_r compared to the delay of the control target, and, since it is a positive feedback, is intact it is difficult to keep the control system stable. Therefore, it is forced to insert a current regulator for maintaining the stability of the control system to the control system. How to determine the stabilization technique is a very important factor for performing the repetitive control stably.

4.2.1 Time lead compensator

The most important factor in suppressing periodic noise or disturbance by repetitive control is the relationship between the phase and noise compensation signal by repetitive compensator or disturbance of phase. The plant to be controlled has its own frequency characteristic compensation signal because the phase is changed by the frequency band while passing through this plant. There is a possibility that it becomes impossible to cancel the external disturbance signal. Therefore, the control system is stabilized by inserting the time lead compensator for adjusting the phase of the compensation signal.

The basic operation principle of the time lead compensator is shown in Fig. 4.4. Time lead compensator may be realized by being placed in a repetitive compensator series with a dead time element e^{-sTr}. However, since it is impossible to actually realize the advance time, Fig 4.4 (a) is converted into an equivalent block diagram of Fig. 4.4 (c),

y_o is delayed from y_o^+ is sun of input signal u and output signal y_o of the repetitive controller by T_r , and y is delayed $T_r(1-k_2/N)$. As a result y is ahead to y_o by T_rk_2/N.

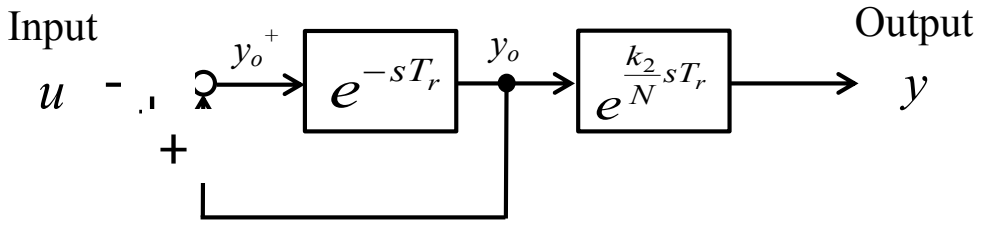

(a) block diagram incorporating a time-lead compensator for a repetitive compensator.

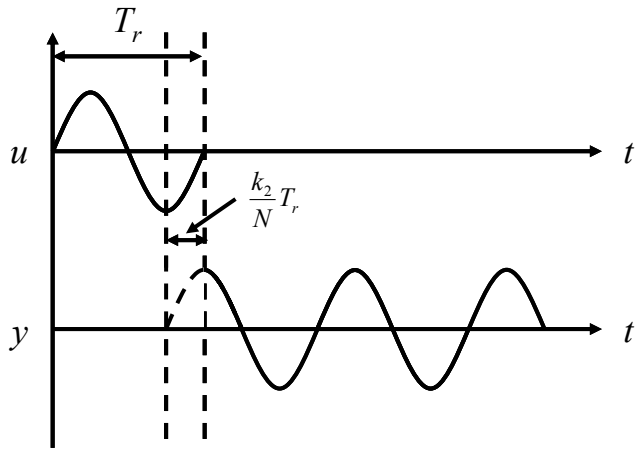

(b) Input and output characteristics of the time lead compensator.

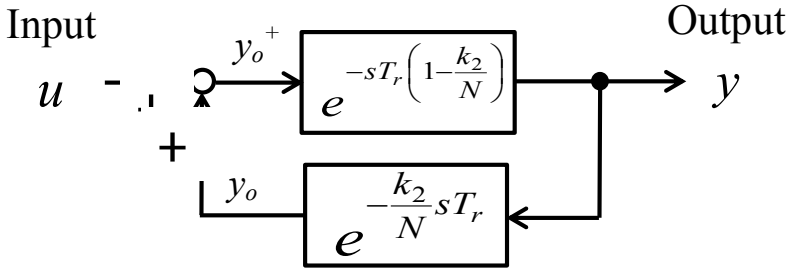

(c) Equivalent block diagram of (a) for repetitive compensator.

Fig. 4.4 The basic operating principle diagram of the time lead compensator.

4.2.2 Repetitive control system incorporating the Fourier transform

As described in Section 4.2.1, the phase characteristics of the control system, depending on the configuration and the control target of the control system because they may vary greatly with frequency, described above with respect to a plurality of disturbance components having different frequencies.When you do repetitive control, a disturbance component sometimes diverge and can not be suppressed. Therefore, in some cases in order to keep surely stabilize the control system performs the phase adjustment to the harmonic components each (set of appropriate k_2), it is necessary to learn the compensation signal.

This can be done by extracting only specific components in the input signal u by using a Fourier transform process as Fig.4.5. The compensation signal is leared by repetitive compensator only for the particular component extracted by FT.

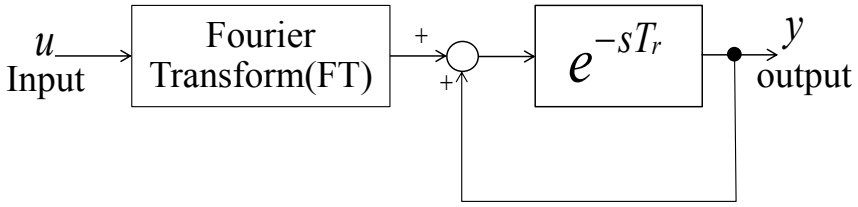

Fig.4.5 The repetition control that incorporates a Fourier transform expansion

Extraction of a specific frequency component by Fourier transformation processing is performed by digital signal processing. Where the detected signal u and a_n arbitrary periodic function $f(t)$ of period T_f [sec], it is expressed by Fourier transformation as shown in eq. (4.2), the coefficients an, bn, are expressed as the eq. (4.4) and eq. (4.5),respectively.

$$u(t) = f(t) = a_0 + \sum_{n=1}^{\infty} a_n \cos(n\omega t) + \sum_{n=1}^{\infty} b_n \sin(n\omega t)$$
$$= A_0 + \sum_{n=1}^{\infty} A_n \sin(n\omega t) + \phi_n \tag{4.2}$$

$$a_0 = A_0 = \frac{1}{T_f}\int_0^{T_f} f(t)dt \tag{4.3}$$

$$a_n = \frac{2}{T_f}\int_0^{T_f} f(t)\cos(n\omega t)dt \tag{4.4}$$

$$b_n = \frac{2}{T_f}\int_0^{T_f} f(t)\sin(n\omega t)dt \tag{4.5}$$

$$A_n = \sqrt{a_n{}^2 + b_n{}^2}\ , \quad \phi_n = \tan^{-1}(\frac{a_n}{b_n}) \tag{4.6}$$

Here, ω is angular frequency corresponding repetitive period T_f, $\omega=2\pi/T_r$, A_0 is the DC component of the detection signal, A_n is the amplitude of *nf* harmonic components. In this paper, since the harmonic components generated by the n times the frequency of the mechanical angle drive frequency *f* of the motor is referred to as *nf* harmonic components. *nf* harmonic component The $u_n(t)$ is expressed by (4.7) , as follows

$$\begin{aligned} u_n(t) &= a_0 + a_n\cos(n\omega t) + b_n\sin(n\omega t) \\ &= A_n\sin(n\omega t + \phi_n) \end{aligned} \tag{4.7}$$

The angular frequency is corresponding to the mechanical angular speed of the motor. From (4.4)and eq. (4.5) above, using eq.(4.7) equation, the harmonic components of different frequencies are mixed in the detection signal *u(t),* the *nf* harmonic component $u_n(t)$ can be extracted.

4.2.3 Stability of repetitive control system

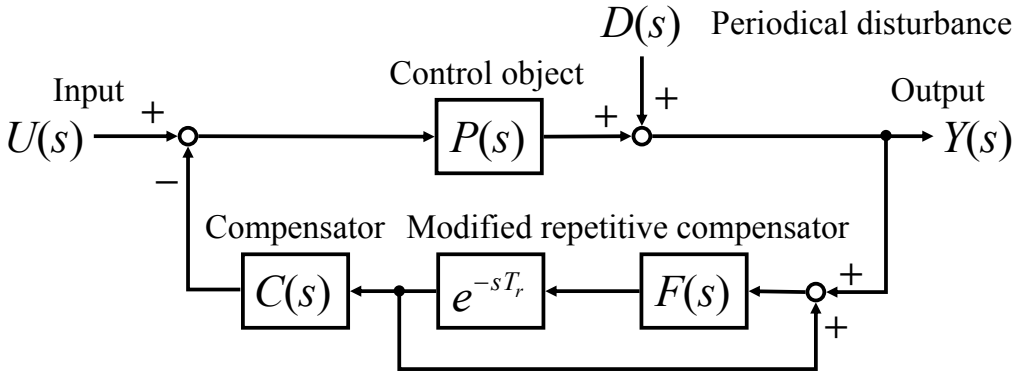

Fig.4.6 The repetitive control system for the periodic disturbance rejection.

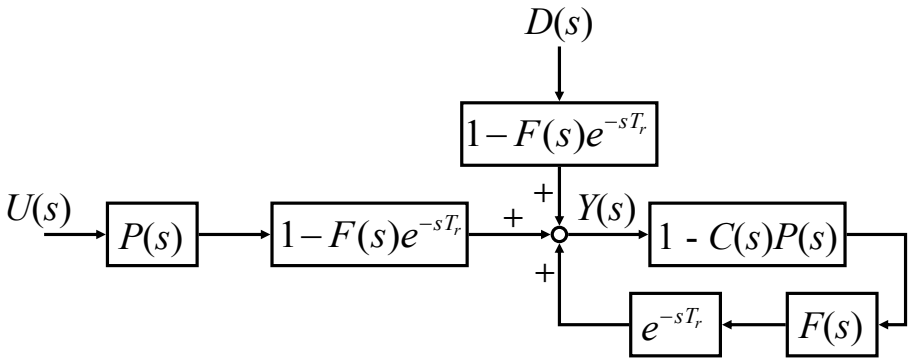

Fig.4.7 Equivalent block diagram of Fig.4.6 focusing on the output *Y (s).*

Now the stability of a repetitive control system is considered. Figure 1 shows a block diagram of a repetitive control system for rejection of periodic disturbances. In the diagram, *Y*(*s*) is the control output, and *P*(*s*), *C*(*s*), *F*(*s*), and *D*(*s*) are, respectively, the transfer function of the controlled object, the transfer function of the repetitive compensator, the transfer function of the repetitive compensator's filter, and the periodic disturbance. Here, the transfer function focusing on output *Y(s)* of the control system is given by

$$Y(s) = e^{-st_r} F(s)\{1 - C(s)P(s)\}Y(s) + \{1 - F(s)e^{-st_r}\}\{D(s) + U(s)P(s)\} \tag{4.8}$$

From the eq. (4.8), if attention is focused to the output *Y(s)*, the equivalent block diagram of Fig.4.6 consists to the equivalent block diagram as shown in Fig.4.7. By virtue of the small-gain theorem, the sufficient condition for stability of the control system in Fig. 4.7 is given by

$$\left\| F(j\omega)\{1 - C(j\omega)P(j\omega)\} \right\|_{\infty} < 1 \qquad \forall \omega \tag{4.9}$$

In eq. (4.9) , a 1-input 1-output in all the frequency domain of the scalar system, if the control system less than one- loop transfer function is stabled. This is a sufficient condition, the system in which the phase is rotated as repetitive control, be close to the requirement in the high-frequency region. In particular, | *F (s)* | = 1, the stability condition of the control system of Fig.4.7 is given by

$$\left| 1 - C(j\omega)P(j\omega) \right| < 1 \qquad \forall \omega \tag{4.10}$$

4.3 Algorithm of the control system in the discrete-time system

4.3.1 Process of the Fourier Transform(FT)

Fourier Transform algorithm in the discrete-time system is shown in Fig.4.9. Since the period T_f of the FT process is changed in synchronization with the drive frequency f of the motor, It is calculated by using the magnetic pole position information obtained by cycle T_f for each cycle of the FT expansion from the estimated $\hat{\theta}_{rfm}$. Incidentally, when outputting the *nf* harmonic component from the FT process is used Fourier coefficients obtained in the previous cycle.

The summary is described of the operation of the cycle j + 1 with an operating principle diagram shown in Fig.4.9.

(a) Signal detection

One period T_f [sec] of the FT expansion and at each of the sampling time (synchronous to the carrier frequency of the inverter), the values obtained by multiplying the cos($n\omega t$) and sin ($n\omega t$) to the input signal f to the DSP (t_{j+1}) are calculated respectively.

(b) Fourier coefficient calculation

Determine the period T_f of the Fourier transform expansion, are obtained by integrated the values calculated in (a), the Fourier coefficient a_n (t_{j+1}) and b_n (t_{j+1}).

(c) Signal output

j th cycle of the FT of a_n (t_j), b_n (t_j) which are outputs f (t_j) of *nf* harmonic component *j + 1* in the cycle by using the eq. (4.7).

4.3.2 Adjusting method of repetitive control parameters [7]

In the section 4.2 was explained the stabilization technique of repetitive control system, the control system in Fig. 4.1 is stable if eq. (4.10) is satisfied. In the proposed control system in Fig. 4.1, only the *nf* components of the frame vibration are input to the repetitive controller, and therefore, the sufficient condition for stability of the control system is given

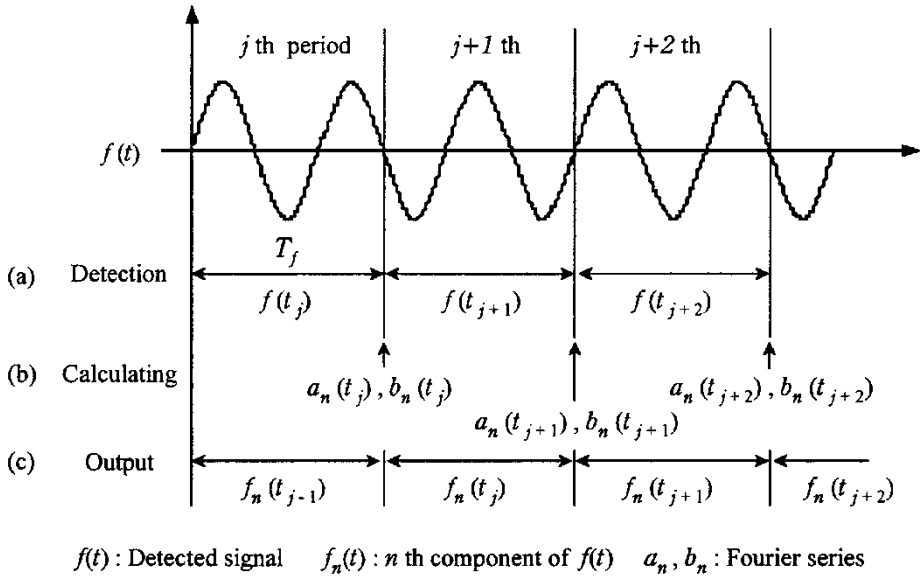

Fig.4.8 Algorithm process of the Fourier Transform

$$\| 1 - C(j\omega_n)P(j\omega_n) \| < 1 \tag{4.12}$$

However, ω_n is the angular frequency of *nf* components of the frame the vibration that has been extracted. For components other than ω_n components to be excluded by the Fourier transform

$$C(j\omega)P(j\omega)=0,$$

Therefore, (4.13)

$$\| 1 - C(j\omega)P(j\omega) \|=1$$

Here ωn is the angular frequency of the *nf* component of the frame vibration. Eq.(4.13) means that the operating point corresponding to $\omega = \omega_n$ on the Nyquist locus lies within the unit circle as shown in Fig. 4.9. Thus, the parameters must be set so that no operating points exist outside the unit circle. Consider, for example, the operating point *A*0 in Fig. 4.9. Since this operating point lies outside the unit circle *k*1 and *k*2 in Fig. 4.11 must be changed so as to move the point into the unit circle. The proportional compensator *k*1 can be varied from $1 + j0$ to the operating point, and the phase compensator $e(k2 / N)sTr$ can be adjusted around $1 + j0$; therefore, the control system can be stabilized by appropriate setting of *k*1 and *k*2. The stability of the control system in Fig. 4.9 is maintained if the

operating point is moved to $A1$, but this is not desirable from the standpoint of convergence. Therefore, the operating point must be moved into a part of the unit circle that offers good convergence.

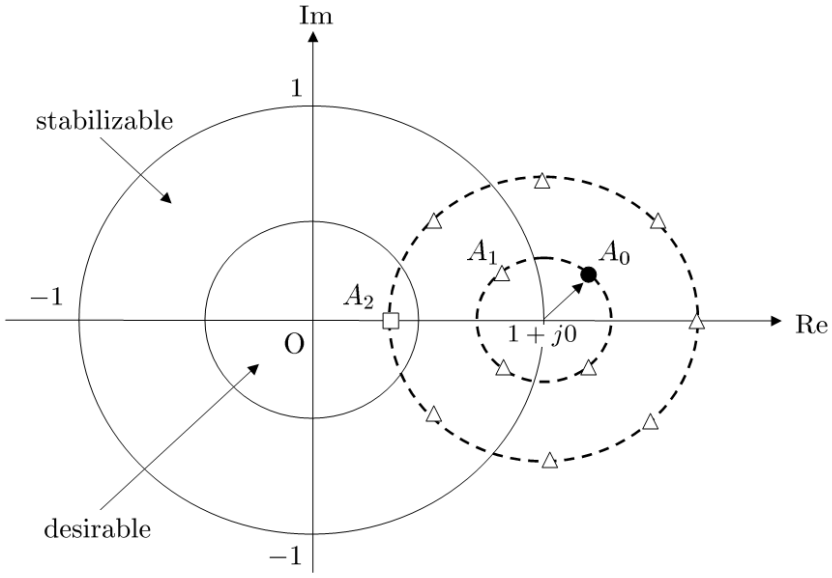

Fig.4.9 Example of a parameter adjustment due to repetitive controller.

4.4 Conventional method: vibration suppression control using the repetitive control

In this section, the literature [2] - [4] in the conventional vibration suppression techniques has been proposed briefly described with reference to the figures.

(1) The method used in the literature [2] - [3]

Fig. 4.10 in the literature [2], shows a system overall view of the techniques that have been proposed in [3]. In these methods, to detect the frame acceleration α_f by the acceleration sensor for SPMSM under torque control, and generates a compensation signal i_c by inputting to the repetitive controller. The compensation signal i_c is superimposed to the q-axis current command value, vibration suppression is performed.

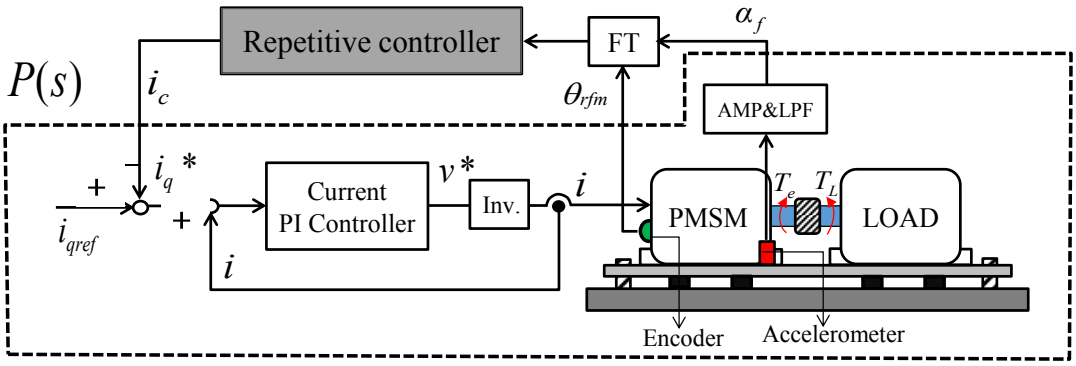

Fig.4.10 Method of the literature [2] and [3].

(2) The method of the literature [4].

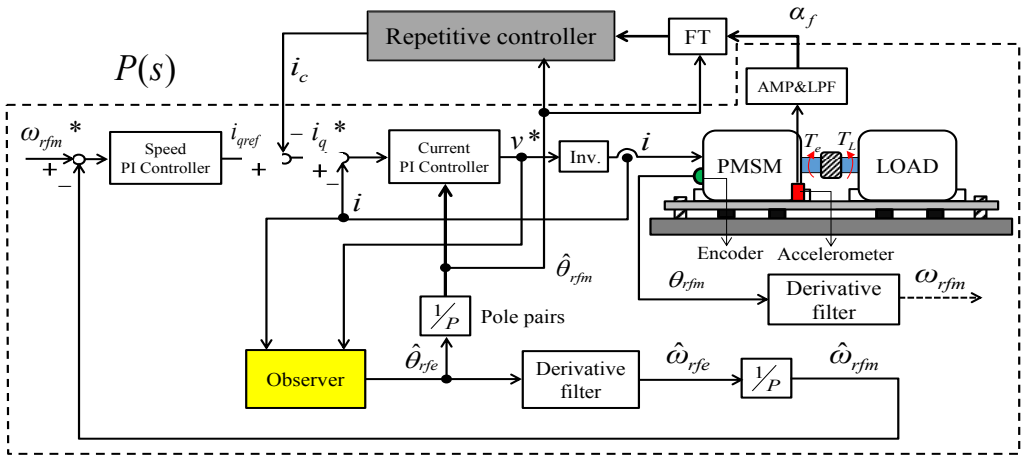

Fig.4.11 Method of the literature [4].

Fig. 4.11 shows the system overall view of the approach that has been proposed in the literature [4]. This technique by applying the technique of [2] to the position sensorless speed control system of the PMSM, the vibration suppression control method that does not require a position sensor have been proposed. In [4], using the vibration detection sensor (acceleration sensor) generated only the compensation current signal, and generates a polynomial of the compensation current signal in the steady state. Thereafter, by performing feed-forward compensation using the generated compensating current signal is realized the position and acceleration sensorless vibration suppression control.

In motor-drive application, causes of torque ripple are roughly categorized as either motor-based or load-based one. The factors based on motor include cogging torque and spatial harmonics of flux, which presents a high-frequency torque ripple such as 6^{th}, 12^{th} and 18^{th} harmonics of motor electrical speed ω_{re}.

Other hand, including in the compressor of interest in this study, the vibration caused by the torque ripples based on load side consist of load torque ripple such as load structure. They present torque ripples with torque ripples relatively low-frequency such as *1/P, 2/P, 3/P* (*P* = number of motor pole pair) or 2nd harmonics of motor electrical speed.

Reference

[1] Hattori, Ishida, Hori: "Torque vibration suppression control of brushless DC motor according to the repetition control using the Fourier transform", Instrument and Control Society Papers, Vol 36, No. 5, pp.438 / 447, 2000 .
[2] Hattori, Ishida, Hori: "vibration suppression control of PMSM by the parameter automatic adjustment function with repeated control using the Fourier transform", the Institute of Electrical Engineers theory D, vol.121-D, No.3, pp.347-355 , 2001.
[3] Shimada, Kawai, Zankan, Ishida: "frame vibration suppression control method in sensorless control system of PMSM", the Institute of Electrical Engineers theory D, Vol.128, No.11, pp.1246-1253, 2008.
[4] Kato, Ishida: "vibration suppression control by the estimated velocity pulsation suppression using repetitive control in PMSM position sensorless control system",
the Institute of Electrical Engineers of motor drive linear drive Joint Study Group, MD-13-62 LD-13-124, pp.115-119, 2013
[5] B.A. Francis, W.M. Wonham," The internal model principle for linear multivariable regulators", Applied Mathematics and Optics, 2 (1975), pp. 170–194.
[6] Nakano M, Inoue T, Yamamoto Y, Hara S. Repetitive control. SICE-Verlag; 1999 (in Japanese).
[7] Shimada, Wai, Zanma, DOKI, Ishida," Sensorless Suppression Control for Frame Vibration of PMSM", Electrical Engineering in Japan, Vol. 174, No. 3, 2011.

Chapter 5

Specific Component Reduction System (SCRS) [(Proposed Method)]

In the previous chapter, the excellent removal ability of the repetitive controller with Fourier Transform for the periodic signal has been described. However, the repetitive compensator has large gains in the frequency and multiples of it as shown in Fig. 4.3, it amplifies high-frequency noise. Hence, under the sensorless control, it is adapted to contain the noise is difficult. Therefore, this chapter discusses the Specific Component Reduction System(SCRS) developed from the repetitive controller, which is a conventional method. The SCRS is composed of the speed controller and Specific Component Reduction Controller (SCRC) which comprises Fourier Transformer(FT) and the compensation signal generator (SG).

In Section 5.1, the characteristics of the SCRS, and the basic operation of the SCRS are described. A comparison of SCRC with the repetitive controller described in Chapter 4 is explained. In Section 5.2, as a method for stabilizing the SCRS, the integral gain and phase adjustment function is described.. In Section 5.3, Actually, the algorithm and Fourier series expansion process of SCRS in the discrete-time system at thetime of implementation installed in the DSP are explained. In Section 5.4, we describe the position and acceleration sensor-less vibration suppression control system is proposed.

5.1 Basic characteristics of the SCRS

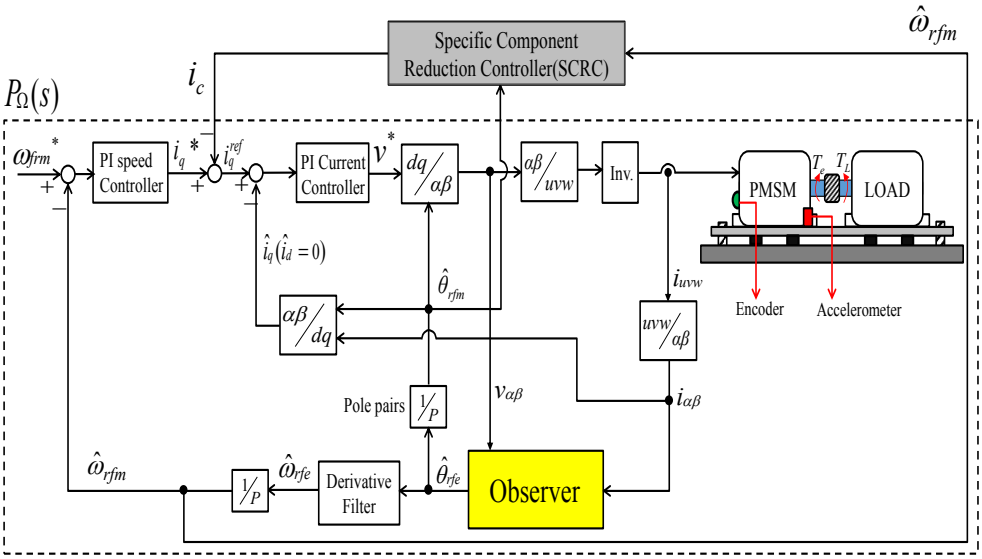

Fig. 5.1 Overall proposed position sensorless vibration suppression system with SCRC.

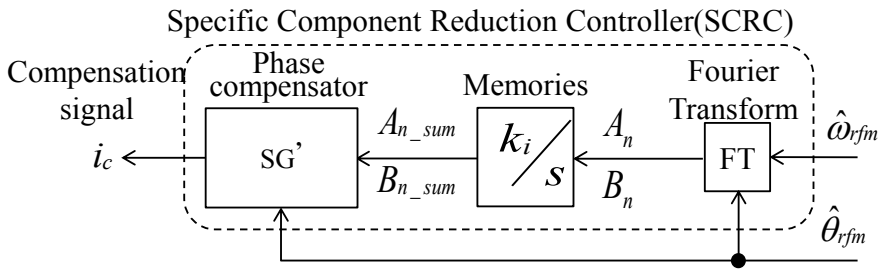

Fig. 5.2 (a) Original form of the SCRC.

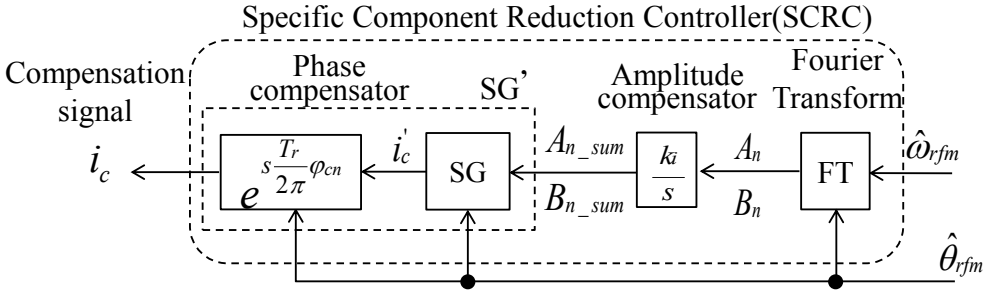

Fig. 5.2 (b) Equivalent form of the SCRC.

The whole speed sensorless anti-vibration control system is shown in Fig. 5.1. A modified anti-vibration controller called SCRC is proposed in Fig.5.2(a) and (b). In the SCRC, Fourier coefficients An and Bn are extracted by FT, and integrated to generate a compensation signal An_sum and Bn_sum. ki is the integration gain, and φcn is the phase compensation gain. The SCRC is unlikely to amplify high frequency noise of $\hat{\theta}_{rfm}$.

As there is only one target fluctuation frequency component $1/T_r$ left after FT in Fig.5.2(b), the output signal of SG and SG' are shown as follows:

$$i_c^{'} = A_{n\_sum}\cos(\hat{\theta}_{rfm}) + B_{n\_sum}\sin(\hat{\theta}_{rfm}) . \tag{5.1}$$

$$\begin{aligned} i_c &= A_{n\_sum}\cos(\hat{\theta}_{rfm} + \varphi_{cn}) + B_{n\_sum}\sin(\hat{\theta}_{rfm} + \varphi_{cn}). \\ &\cong A_{n\_sum}\cos(\frac{2\pi}{T_r}t + \varphi_{cn}) + B_{n\_sum}\sin(\frac{2\pi}{T_r}t + \varphi_{cn}) \end{aligned} \tag{5.2}$$

,where T_r is the cycle time of rotor mechanical angle, which is constant in steady state. A_{n_sum} and B_{n_sum} can be calculated as:

$$A_{n\_sum} = A_{n\_sum}^{(0)} + k_i\int_0^t A_n(t)dt \tag{5.3}$$

$$B_{n\_sum} = B_{n\_sum}^{(0)} + k_i\int_0^t B_n(t)dt .$$

Take eq. (5.3) into a discrete one, which includes the cycle time T_r . It can be expressed as :

$$\begin{aligned} A_{n\_sum}^{(k+1)} &= A_{n\_sum}^{(k)} + k_i T_r A_n^{(k)} \\ B_{n\_sum}^{(k+1)} &= B_{n\_sum}^{(k)} + k_i T_r B_n^{(k)} . \end{aligned} \tag{5.4}$$

The calculation of the signal after SG in Fig.5.2(b) is shown as follows:

$$\begin{aligned} i_c^{(k+1)} &= A_{n\_sum}^{(k+1)}\cos(\frac{2\pi}{T_r}t) + B_{n\_sum}^{(k+1)}\sin(\frac{2\pi}{T_r}t). \\ &= A_{n\_sum}^{(k)}\cos(\frac{2\pi}{T_r}t) + B_{n\_sum}^{(k)}\sin(\frac{2\pi}{T_r}t) \\ &\quad + k_i T_r\{A_n^{(k+1)}\cos(\frac{2\pi}{T_r}t) + B_n^{(k+1)}\sin(\frac{2\pi}{T_r}t)\} \end{aligned} \tag{5.5}$$

In this way, eq.(5.5) can be expressed as eq.(5.6):

$$i_c^{(k+1)} = i_c^{(k)} + k_i T_r \cdot \Delta\hat{\omega}_{rfm} = i_c^{(k)} + \Delta i_c^{(k)} . \tag{5.6}$$

At last, the compensation signal i_c in Fig.5.2(a) is rewritten in discrete form as follows:

$$i_c = A_{n\_sum}^{(k)} \cos\left(\frac{2\pi}{T_r}t + \varphi_{cn}\right) + B_{n\_sum}^{(k)} \sin\left(\frac{2\pi}{T_r}t + \varphi_{cn}\right). \tag{5.7}$$

With eq.(5.5) to eq.(5.7), SCRC in the form of Repetitive Controller can be established. It is shown in Fig.5.2(c).

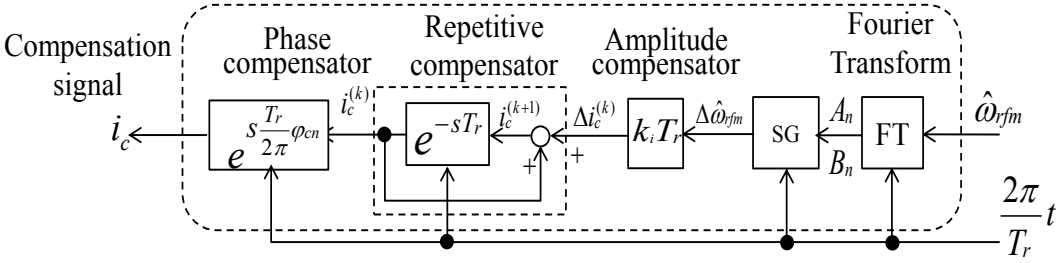

Fig. 5.2 (c) SCRC in the form of Repetitive Controller.

From Fig.5.2(c), it can be known that SCRC has no influence of estimated position $\hat{\theta}_{rfm}$, which includes high-frequency noise. And this form of the SCRC is taken into the system analysis in the next section.

Consequently, the stability criterion for determining compensation gain of k_i and φcn in SCRC can be discussed in the next section.

5.2 Stability analysis of proposed system

5.2.1 System Stability

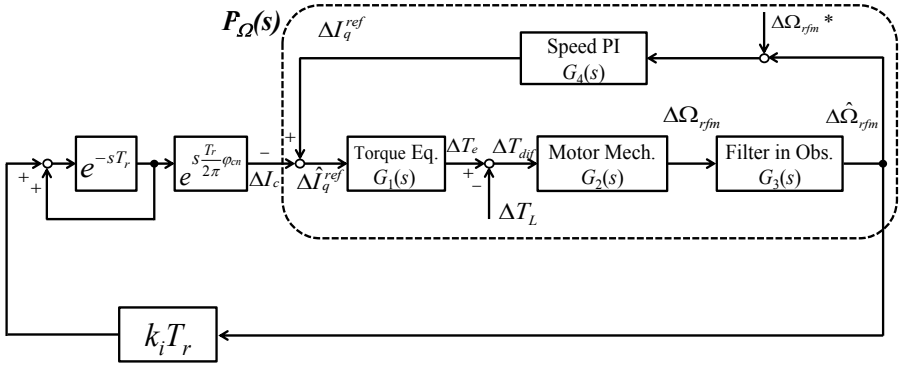

Fig. 5.3 Proposed system diagram of the linear approximation vibration suppression system.

By using the equations (3.25), considering eq. (2.18) and eq. (3.24) with respect to the perturbed variables (ΔI_{dq}, $\Delta\Omega_{rfm}$, *and* $\Delta\hat{\Omega}_{rfm}$) around the steady state operating points (I_{dq0}, Ω_{rfm0}, *and* $\hat{\Omega}_{rfm0}$), $\Delta T_e = L\{\Delta\tau_e\}$, Fig. 5.3 is obtained. In Fig. 5.3, the transformation $G_1(s)$, $G_2(s)$,$G_3(s)$ *and* $G_4(s)$ are given

$$G_1(s) = \frac{\Delta T_e}{\Delta \hat{I}_q^{ref}} = PK_e. \tag{5.8}$$

$$G_2(s) = \frac{\Delta\Omega_{rfm}}{\Delta T_{dif}} = \frac{(J_f + J_r)s^2 + D_f s + K_f}{J_r s(J_f s^2 + D_f s + K_f)}. \tag{5.9}$$

$$G_3(s) = \frac{\Delta\hat{\Omega}_{rfm}}{\Delta\hat{\Omega}_{rfm}} = \frac{\alpha}{s+\alpha}. \tag{5.10}$$

$$G_4(s) = \frac{\Delta I_q^{ref}}{\Delta\hat{\Omega}_{rfm}} = -\frac{K_{ps}s + K_{is}}{s}. \tag{5.11}$$

$$\begin{aligned} P_\Omega(s) &= \frac{\Delta\hat{\Omega}_{rfm}}{\Delta I_c} \\ &= [1 + G_1(s)G_2(s)G_3(s)G_4(s)]^{-1} G_1(s)G_2(s)G_3(s). \end{aligned} \tag{5.12}$$

where $G_1(s)$ is the torque constant by eq. (3.25), $G_2(s)$ is the transfer function of the motor and load mechanical system from eq. (2.18), $G_3(s)$ is that of the filter in observer derived from eq. (3.24), and $G_4(s)$ is the PI speed controller gain. ΔI_c is generated by the repetitive controller to suppress estimated speed ripple $\Delta\hat{\Omega}_{rfm}$ .The load torque ripple ΔT_L is regarded as a disturbance torque.

Because the characteristics of $P_\Omega(s)$ in Fig. 5.3 shows that the $P_\Omega(s)$ decreases high-frequency harmonics or noise, and FT extract only target frequency 10[Hz] into SCRC. As a result, SCRC will not amplify high-frequency noise or harmonics. While in this time, the proposed system doesn't amplify high-frequency harmonics or noise. In this way, the concept of system analysis shown in [4] [5] [7] [8] can be taken in the stability analysis of the proposed system.

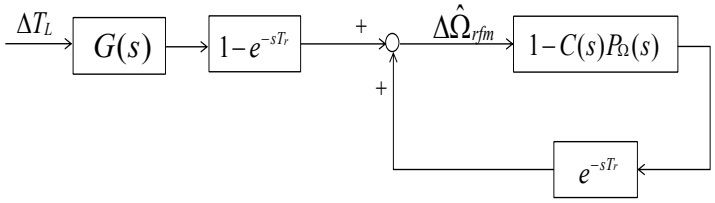

Fig. 5.4 Transformed equivalent block diagram.

With the input signal $\Delta\hat{\Omega}_{rfm}$, the block diagram shown in Fig.5.3 is transformed into one shown in Fig. 5.4. With the small gain theory[5], and [6]-[8], eq. (5.12) can be got

$$\left|1-C(j\omega_n)P_\Omega(j\omega_n)\right|<1. \tag{5.13}$$

The transfer functions in Fig. 9 are shown as follows:

$$C(s)=k_iT_re^{s\frac{T_r}{2\pi}\varphi_{cn}}. \tag{5.14}$$

$$G(s)=\frac{\Delta\hat{\Omega}_{rfm}}{\Delta T_L}=G_2(s)G_3(s). \tag{5.15}$$

Where $P_\Omega(s)$: transfer function of motor and the torque ΔI_c to $\Delta\hat{\Omega}_{rfm}$.

$C(s)$: transfer function of proportional compensator and time leading element.

$G(s)$: transfer function from ΔT_L to $\Delta\hat{\Omega}_{rfm}$.

5.2.2 SCRC parameters k_i, φ_{cn}

Fig. 5.5 shows the Nyquist plot of $1-C(j\omega n)\,P_\Omega(j\omega n)$. The Nyquist analysis is considered according to the criteria expressed in eq. (5.13). If the operation point A" stays out of the unit circle, the SCR-System is unstable at this point. Then, an operating point can be moved into the unit circle by reversing the sign of k_i as shown in Fig. 5.5(a) (A"→A). Reversing the sign of k_i means phase shift by π. However, B" shown in Fig. 5.5(b) can not be moved into the unit circle by reversing k_i. In such a case, the operation point can be moved into the unit circle by using the phase compensator gain φcn (B"→B).

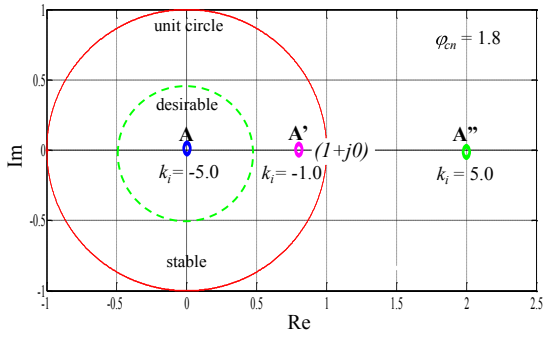

(a) Case A: when the operating point exits outside of the unit circle (φcn = 1.8), and reverse signs of k_i.

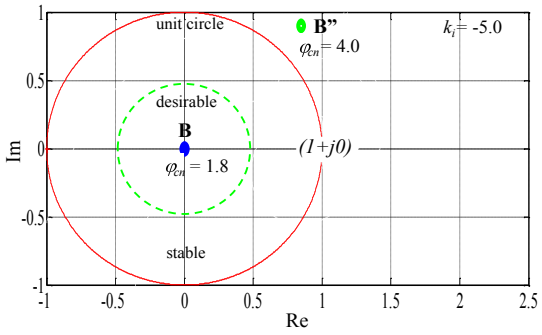

(a) Case B: when the operating point exits outside of the unit circle with the phase control sign of φ_{cn}.

Fig. 5.5 Nyquist plot of transfer function (1-$C(s)\ P_{\Omega}(s)$).

Nyquist operation point stays near the original point, from the view point of faster convergence of the speed vibration, which menas that $H(j\omega_n)$, defined as

$$H(j\omega_n) = 1 - C(j\omega_n)P_{\Omega}(j\omega_n), \tag{5.16}$$

is nearly zero, that is $H(j\omega_n) \cong 0$. Thi s condition is useful from the view point of stability margine. That is, when the parameters of the system is changed and than the position of $H(j\omega_n)$ moves to the complex plane, the $H(j\omega_n)$ still stay inside the unit circle . this meanes that, the original point of $H(j\omega_n)$ is near origin.

From $H(j\omega_n)=0$,

$$C(j\omega_n) \cong \frac{1}{P_{\Omega}(j\omega_n)}. \tag{5.17}$$

$$P_{\Omega}(j\omega_n) = A_{\Omega}e^{(j\varphi_{\Omega})}. \tag{5.18}$$

With eq. (5.17) and eq. (5.18) k_i and φ_{cn} can be got as follows:

$$\begin{cases} k_i = \dfrac{1}{A_{\Omega}T_r} \\ \varphi_{cn} = -\varphi_{\Omega} \end{cases} or \begin{cases} k_i = -\dfrac{1}{A_{\Omega}T_r} \\ \varphi_{cn} = -\varphi_{\Omega} \pm \pi \end{cases}. \tag{5.19}$$

Therefore, the operation point can be moved within the unit circle by adjusting the gain of k_i *and* φcn. This means that the control system will be stable.

Reference

[1] JULIUS O. SMITH III, “Mathematics of the Discrete Fourier Transform (DFT), with Audio Applications --- Second Edition" , ISBN 978-0-9745607-4-8,W3K Publishing, 2007.

[2] Z. Chen, M. Tomita, S. Doki, and S. Okuma, “An extended electromotive force model for sensorless control of interior permanent magnet synchronous motors,” IEEE Trans. Ind. Electron., vol. 50, no. 2, pp. 288–295, Apr 2003.

[3] D. W. Novotny and T. A. Lipo, “ Vector Control and Dynamics of AC Drives” , publications in theUnited Staes by Oxford UniversityvPress Inc. New York, 1996.

[4] T. Su, S. Hattori, M. Ishida, and T. Hori, “Suppression control method for torque vibration of ac motor utilizing repetitive controller with Fourier transform,” IEEE Trans. Ind. Appl., vol. 38, no. 5, pp. 1316–1325, Sep 2002.

[5] A. Shimada, K. Kawai, T. Zanma, S. Doki, and M. Ishida, “Sensorless Suppression Control for Frame Vibration of PMSM,” IEEJ Trans., vol. 128, no. 11, pp. 1246-1253, 2008.

[6] S. Hattori, M. lshida and T. Hori, "Suppression Control Method for Torque Vibration of Brushless DC Motor Utilizing Repetitive Control with Fourier Transform," IEEE Trans. Ind. Electron., pp.427-432, 2000.

[7] M. lshida, Tinghsu Su, Hattori, S. and Hori T., ”Suppression control method for torque vibration of AC motor utilizing repetitive controller with Fourier transformer”, Industry Applications Conference of IEEE, vol.3, pp.1675 – 1682, 2000.

[8] D. S. Naidu, Optimal Control System, Idaho State University Pocatello, Idaho, UAS, 1940.

CHAPTER 6

FRAME VIBRATION SUPPRESSION METHOD FOR SENSORLESS PMSM-DRIVE APPLICATION

There is a significant frame vibration problem which caused by noise in the application of PMSM Sensorless control. In former research, an anti-vibration method called Repetitive Controller has been proposed[1]. But the Repetitive Controller has large gains at desired frequencies. It may amplify high-frequency noise. The accelerometer is also applied into the system.

In this paper, a novel anti-vibration controller called Specific Component Reduction Controller (SCRC) with position sensorless control has been proposed. It can work without accelerometer. This paper consists of the following parts. Firstly, the Conventional Frame Vibration Suppression System will be given. Secondly, Proposed Frame Vibration Model and Load Torque Ripple. Thirdly, the Construction of proposed the frame vibration suppression system using estimated speed will be explained. Fourthly, SCRC will be discussed, and the stability of SCRC will be analyzed. At last, the experimental results show that SCRC can achieve speed variable control and compensate target frequency torque ripple.

6.1 Introduction

Permanent Magnet Synchronous Motors (PMSM) are widely used in industry because of relatively high efficiency and high maintainability. However, in some applications such as compressor, load torque fluctuates due to its structure. The torque ripple generates frame vibration which results in noise and deterioration of control accuracy. One approach to suppress the vibration is the use of anti-vibration rubber (AVR). The advantage of AVR is ease of installation. However, temperature or environment makes the performance worse.

The other approaches are based on the use of proper control techniques [1] -[5]. A good

example is given by the repetitive control, as proposed in [1] and [3]. However, these methods need accelerometer and position sensor which are expensive, delicate, and need extra space.

The position sensor can be eliminated by suitable sensorless control methods. Since the compressors mainly work at a constant (and relatively high) speed, observers based on Extended Electromotive Force (EEMF) have been reported [6]. Therefore, vibration suppression position sensorless control with EEMF observer at target speed has been proposed [7]. However, this method is demonstrated only in simulation. In addition, since the repetitive controller has a large gain at desired frequency and multiples, the controller is not suitable to learn vibration from the speed with high-frequency noise which is generated by the EEMF observer.

In this paper, a modified anti-vibration controller derived from the repetitive controller with the EEMF observer is proposed, which is hard to amplify high-frequency component. This novel controller is named SCRC. The SCRC learns the Fourier coefficients extracted by Fourier Transform(FT). The coefficients are integrated to generate a compensation signal which is exploited to carry out the proper compensation. The analysis is shown to study the stability of the proposed system, and effectiveness of the proposed system is confirmed by experimental results.

6.2 Conventional Frame Vibration Suppression Control System for Sensorless PMSM Drive

6.2.1 Configuration of Control System

Fig. 6.1 shows an overall system of conventional methods in [1] and [3]. In this system, the accelerometer detects frame acceleration caused by the torque ripple T_{Lrip} which is generated by the load torque. The accelerometer is to generate a compensation signal in the repetitive controller. In the conventional methods, the suppression target is the vibration caused by the imperfection of motor structure and control, which has relatively high order frequency. In order to suppress vibration, the compensation signal i_c generated by the repetitive controller is added to q-axis current reference of the position sensorless.

As repetitive compensator is shown in Fig. 6.2 has large gains at 1/ T_r [Hz], where T_r is period of the input signal (torque ripple) and multiples showed in Fig. 3, the repetitive controller is effective to suppress the periodic disturbance, according to the internal model principle as proposed in [1], [3], and [7]. In this system, target harmonics

of the vibration signal α_{rip} is extracted by FT from the vibration signal detected by an accelerator on the motor frame.

$$\alpha_{rip} = A_n \cos\hat{\theta}_{rfm} + B_n \sin\hat{\theta}_{rfm}\,. \tag{6.1}$$

In Fig. 6.2, *An* and *Bn* are Fourier coefficients, and SG is the signal generator shown in eq. (6.1). Parameters k_1 and k_2 are adopted for system stability as explained below. The repetitive controller causes large phase delay and may magnify the harmonics. It is necessary for making the anti-vibration control loop stable to adjust the amplitude and the phase of the compensation signal i_c added to q-axis current on the motor. Amplitude compensator adjusts the amplitude with the parameter k_1, and phase compensator adjusts the phase with the parameter k_2. With these parameters (k_1 and k_2), the compensation signal i_c is adjusted to reduce the extracted target harmonics α_{rip}. As a result the speed ripple is suppressed.

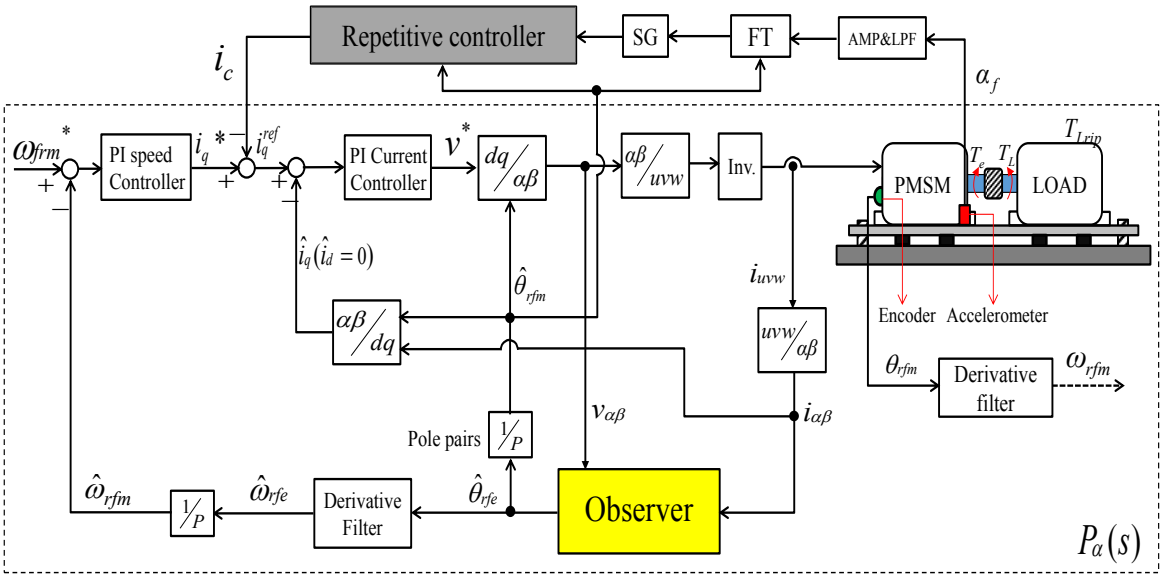

Fig. 6.1 Overall system of the conventional method.

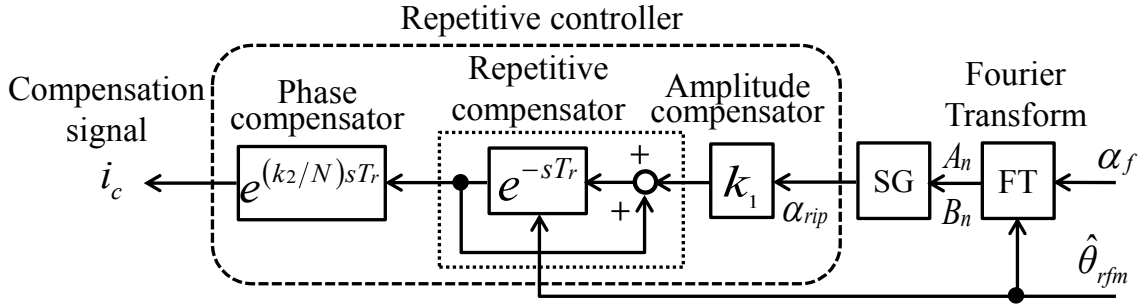

Fig. 6.2 Repetitive controller with Fourier Transform.

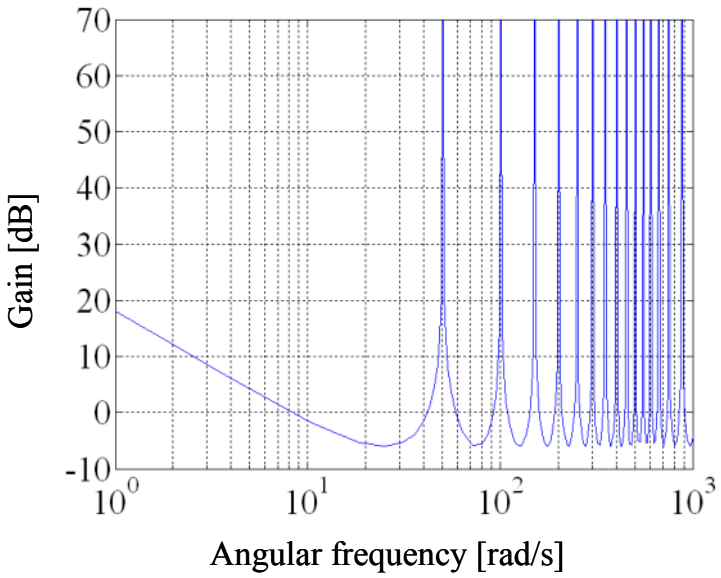

Fig. 6.3 Bode plot of the repetitive compensator.

6.2.2 Concept of System Analysis

Fig. 6.4 is the simplified block diagram of Fig. 6.1 without FT and SG. $P_\alpha(s)$ is the transfer function from the compensation current ΔI_c to suppress target ΔA_f, and $G(s)$ is the transfer function from ΔT_{rip} to ΔA_f. The repetitive controller generates the compensation signal i_c to suppress frame vibration caused by torque ripple ΔT_{rip}.

The repetitive controller has good performance for rejecting periodic noises and disturbances [3]. This kind of control system includes a repetitive compensator and a feedback loop for fast tracking of target signals with an arbitrary period T_r. According to the internal model theorem [3], a general model for the periodic target signal must be incorporated into the closed loop to track the target without stationary errors. A mechanism to generate a periodic function for a target signal with period T_r is implemented by using a time delay element e^{-sT_r} which is reduced by accessing the memory stored with repetitive compensator.

Focusing on the target signal ΔA_f in Fig. 6.4, Fig. 6.5 is obtained where $C(s) = k_1 e^{(k2/N)sTr}$. By virtue of the small gain theorem, the sufficient condition for stability of the control system shown in Fig. 6.5 is given as

$$\left\|1 - C(s)P_\alpha(s)\right\| < 1. \tag{6.2}$$

Fig. 6.5 indicates that if the vector locus of (1-C(jω)P_α(jω)) lies within the unit circle (excluding its circumference), the control system will be stable. The stability of the repetitive control system is determined by the frequency response of the transfer function of (1-C(s)P_α(s)) shown in Fig.6.5. The following condition must be satisfied in order to keep the system stable.

$$\left|1-C(j\omega)P_\alpha(j\omega)\right|<1 \quad for \quad \forall\omega. \tag{6.3}$$

Eq. (6.3) means that whole Nyquist plot of (1-C(jω)P_α(jω)) has to be inside the unit circle for stable operation[8]. On the other hand, since the frequency region of the vibration signal is limited by the Fourier transformer (FT) before the repetitive control in the proposed system, the stability criterion of the system can be expressed below as the sufficient condition:

$$\left|1-C(j\omega_n)P_\alpha(j\omega_n)\right|<1\,. \tag{6.4}$$

where ω_n is the target angular frequency of vibration extracted by the FT. Regarding the other angular frequency components than ω_n, they do not affect the stability of the proposed method in steady-state operation.

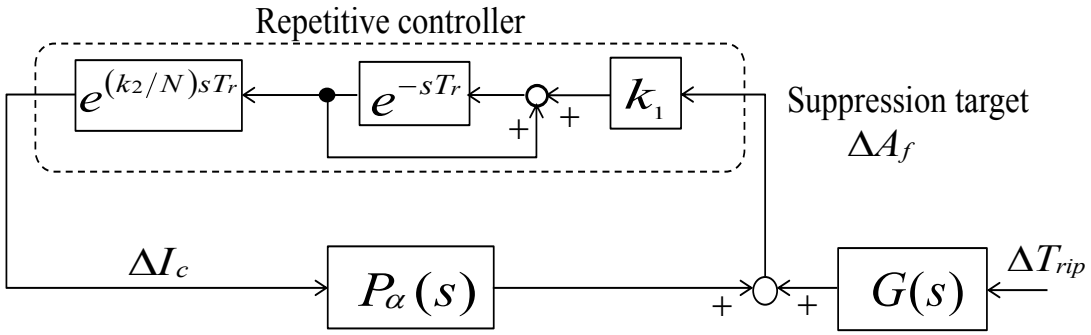

Fig. 6.4 Repetitive control system (FT and SG deleted).

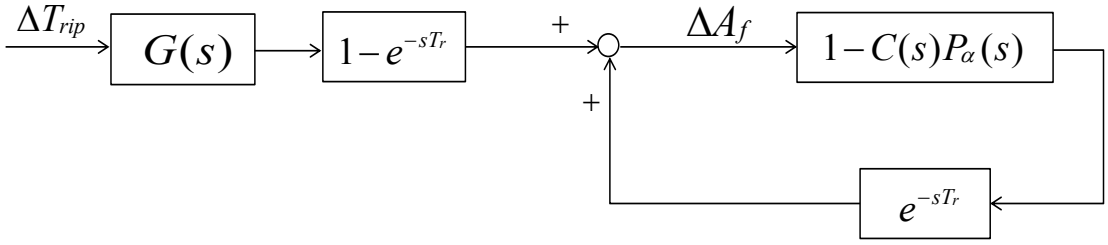

Fig. 6.5 Transformed repetitive control system.

6.3 Proposed Frame Vibration Model and Load Torque Ripple

6.3.1 Motor-Load Mechanical Model around the Shaft

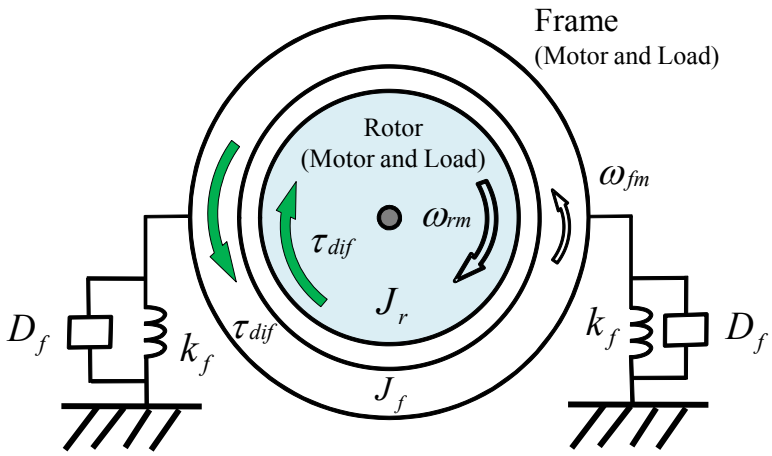

Fig. 6.6 Motor-Load mechanical model around the motor shaft.

Fig. 6.6 shows the Motor-Load mechanical model (frame vibration model) of the rotor and frame around the motor shaft, while the motor frame is suspended by the rubber etc. Here, J_r is the rotor inertia, J_f is the frame inertia, D_f is the frame viscous coefficient, K_f is the frame spring coefficient, ω_{rm} is the rotor mechanical speed, ω_{fm} is the frame mechanism speed, θ_{rm} is the rotor mechanical position, and θ_{fm} is the frame mechanical position, respectively.

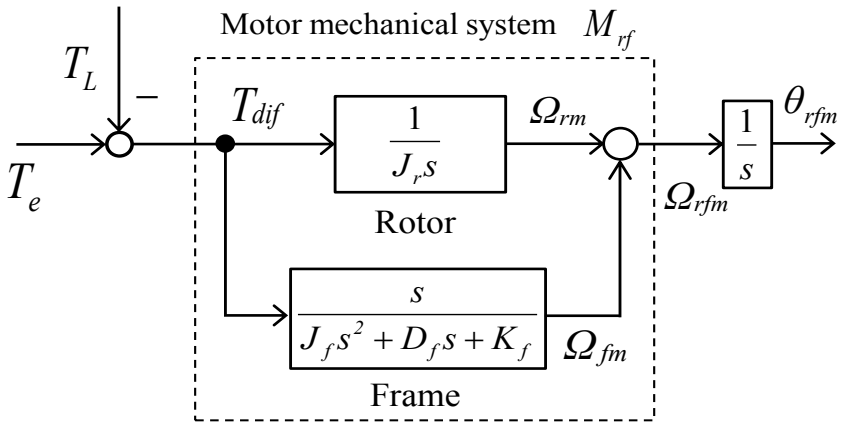

Fig. 6.7 Block diagram of Motor-Load mechanical model.

Fig. 6.7 shows the block diagram of the model shown in Fig. 6.6, where Ω_{rfm} and θ_{rfm} are the motor mechanical speed and the motor mechanical position referred to the motor frame, T_e is the motor driving torque, T_L is the load torque, and T_{dif} is the total torque.

The rotation angle of the motor is represented as the phase difference between rotor coordinates and stator coordinates in the model. In general applications, the frame on the stator side is considered as a standstill. However, In our target system, the position detected by a position sensor θ_{rfm} includes the error due to the frame vibration, when the torque ripple causes the fluctuation of frame mechanical speed. As a result, the motor the motor position θ_{rfm} is described as:

$$\theta_{rfm} = \theta_{rm} + \theta_{fm} . \tag{6.5}$$

6.3.2 Load Torque Ripple

In motor-drive application, causes of torque ripple are roughly categorized as either motor-based or load-based one. The factors based on motor include cogging torque and spatial harmonics of flux, which presents a high-frequency torque ripple such as 6th harmonics of motor electrical speed ω_{re}.

On the other hand, torque ripples based on load side consist of load torque ripple $\Delta\tau_{Lrip}$ such as load structure. They present torque ripples with torque ripples relatively low-frequency such as *1/P, 2/P, 3/P* (*P* = number of motor pole pair) or 2nd harmonics of ω_{re}.

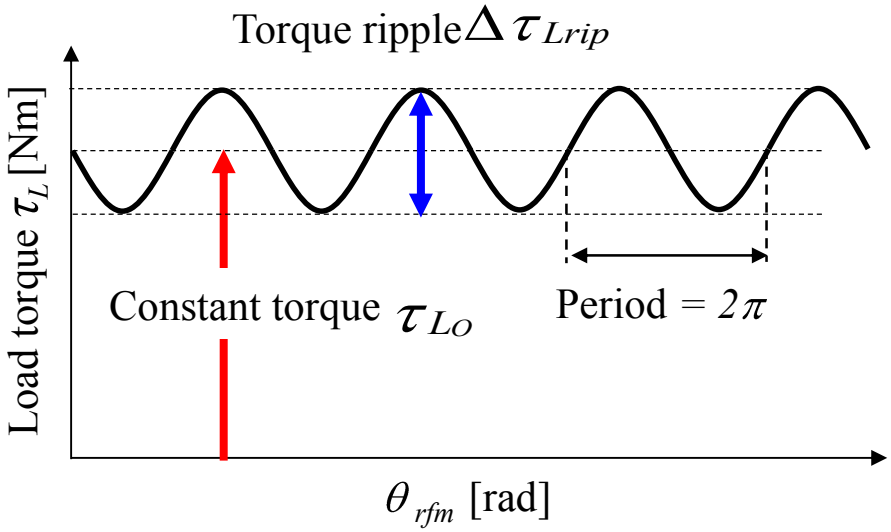

Fig. 6.8 Load torque.

This paper targets the system in which the motor and load are integrated, for example, in compressor applications. In this system, the frame vibration is caused by the load torque ripple $\Delta\tau_{Lrip}$. which is described as a function of the motor position θ_{rfm}, as in Fig. 6.8. The mechanical dynamics of motor frame and rotor in PMSM and load are given as

$$\Omega_{rfm} = M_{rf}(T_e - T_L) = M_{rf}\ T_{dif}. \tag{6.6-1}$$

$$M_{rf}(s) = \frac{(J_r + J_f)s^2 + D_f s + K_f}{J_r s(J_f s^2 + D_f s + K_f)}. \tag{6.6-2}$$

$$\tau_L = \tau_{L0} + \Delta\tau_{Lrip}\ . \tag{6.6-3}$$

$$\Delta\tau_{Lrip} = A_{\tau Lrip}\ \sin(n\theta_{rfm}). \tag{6.6-4}$$

where $A\tau_{Lrip}$ is the amplitude of the load torque ripple, and s is Laplace operator. The load torque ripple $\Delta\tau_{Lrip}$ is the *nth*. order sinusoidal wave. As a result, the periodic speed ripple $\Delta\omega_{rip}$ shown in Fig. 6.7 is expressed as

$$\Delta\omega_{rip} = A_{\omega rip}\ \sin(n\theta_{rfm} + \varphi_{\omega rip}). \tag{6.7}$$

where $A_{\omega rip}$ is the amplitude of the speed ripple, and $\varphi_{\omega rip}$ is the phase of the speed ripple.

6.4 Construction of proposed the frame vibration suppression system using estimated speed

6.4.1 Frame vibration suppression control system using a repetitive controller with FT and SG

The method explained above requires a vibration sensor (accelerometer) as shown in Fig. 6.1, which leads to problems such as high-cost system, noise, and the need for installation space, so the repetitive control system for speed sensorless vibration [7]. In this system, estimated speed $\hat{\omega}_{rfm}$ is used for generating a suppression system (with FT and SG) shown in Fig. 6.9 is proposed compensation signal in repetitive controller. Compensation signal is superposed to q-axis current reference, in order to suppress the vibration. Therefore the position sensor is not necessary. In this system, the suppression target is the vibration caused by the load torque ripple, which has relatively low order

frequency shown in Fig.6.3. However, the system has been validated only by simulation.

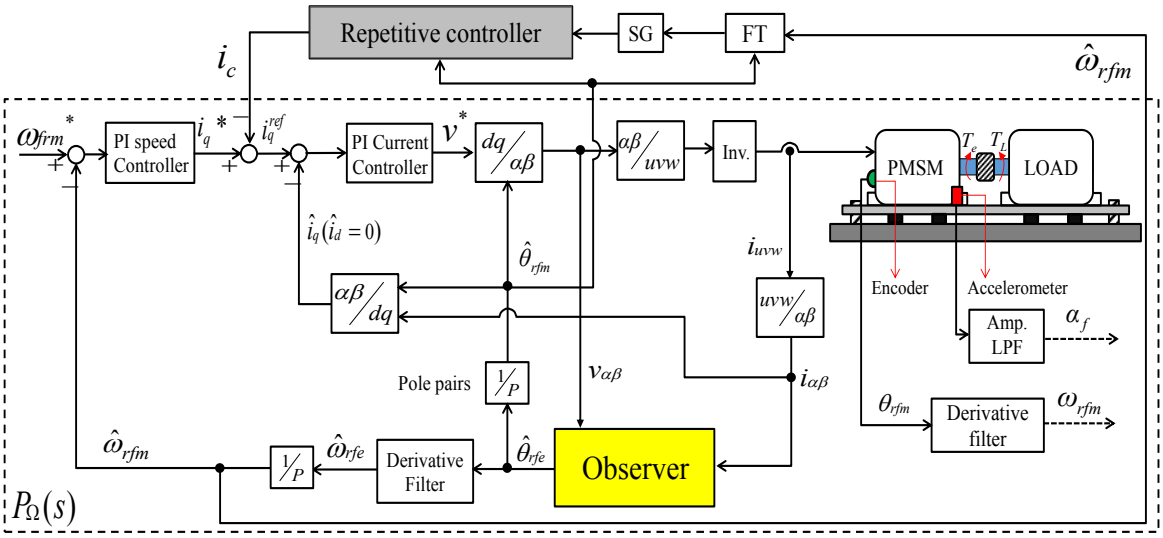

Fig. 6.9 Overall repetitive control system for speed sensorless vibration suppression system (with FT and SG).

6.4.2 Construction of Position Sensorless Control System.

This paper utilizes Field Oriented Control (FOC) system based on EEMF observer, which shown in Fig. 10 (a). the Extended Electromotive Force (EEMF) observer as a position estimator to construct the sensorless control system [6]. The voltage equation for IPMSM on the stator frame coordinate (α-β axis) is given by

$$v_{\alpha\beta} = \{(R + pL_d)I - \omega_{rfe}(L_d - L_q)J\}i_{\alpha\beta} + e_{\alpha\beta}. \quad (6.8\text{-}1)$$

$$e_{\alpha\beta} = \{(L_d - L_q)(\omega_{rfe} i_d - p i_q) + \omega_{rfe} K_e\} J\varepsilon^{J\theta_{rfe}}, \quad (6.8\text{-}2)$$

where

$$\varepsilon^{J\theta_{rfe}} \equiv \begin{bmatrix} \cos\theta_{rfe} & -\sin\theta_{rfe} \\ \sin\theta_{rfe} & \cos\theta_{rfe} \end{bmatrix}; \omega_{rfe} = \frac{d\theta_{rfe}}{dt}. \quad (6.8\text{-}3)$$

where eq. (6.8-2) is defined as EEMF $\boldsymbol{e_{\alpha\beta}} = [e_\alpha \ \ e_\beta]^T$. In eq. (6.8-1), v_α and v_β are the voltages on α-β axis, i_α and i_β are the currents on α-β axis, R is the stator resistance, L_d and

L_q are the inductances on *d-q* axis, and *p* is the differential operator. Since EEMF has information on the real motor position θ_{rfm}, the estimated motor position $\hat{\theta}_{rfm}$ is obtained by EEMF observer shown in Fig. 6.10(b) and eq. (6.9-1) and (6.11-2).

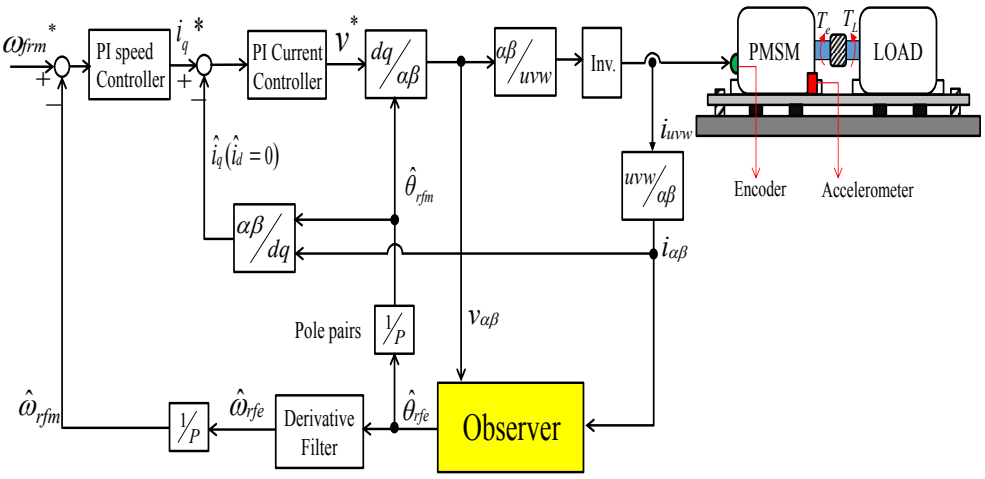

Fig.10(a) Position sensorless drive system of PMSM.

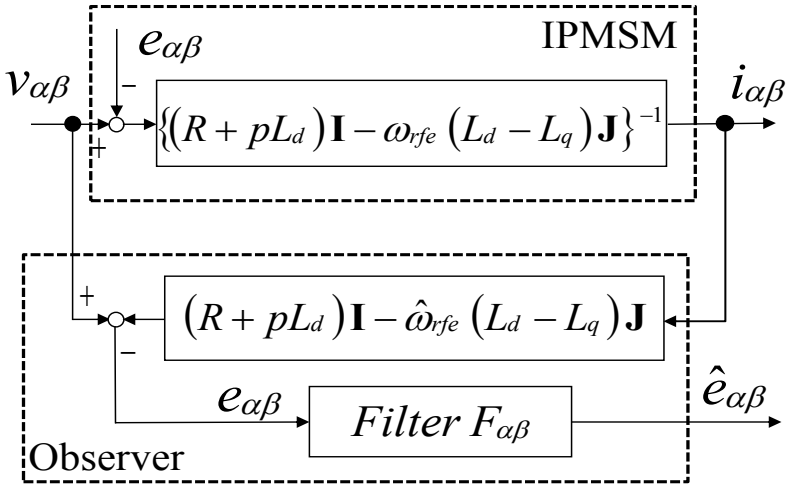

Fig. 6.10 (b) EEMF observer.

$$\theta_{rfm} = \frac{1}{P}\arctan\left(-\frac{e_\alpha}{e_\beta}\right), \tag{6.9-1}$$

where

$$I = \begin{bmatrix} 1 & 0 \\ 0 & 1 \end{bmatrix}, \; J = \begin{bmatrix} 0 & -1 \\ 1 & 0 \end{bmatrix}. \tag{6.9-2}$$

Fig. 6.10 (b) shows the observer which includes the filter $F_{\alpha\beta}$ to remove noise caused by modeling errors. The filter characteristics is given as

$$\hat{e}_{\alpha\beta} = \alpha I\{(p+\alpha)I - \omega_{rfm}J\}^{-1} e_{\alpha\beta} = F_{\alpha\beta} e_{\alpha\beta}, \tag{6.10-1}$$

Where

$$F_{\alpha\beta} = \alpha I\{(p+\alpha)I - \omega_{rfe}J\}^{-1}. \tag{6.10-2}$$

and -α is the designed real axis pole of EEMF.

$$\hat{\theta}_{rfe} = \arctan\left(-\frac{\hat{e}_\alpha}{\hat{e}_\beta}\right). \tag{6.11-1}$$

$$\hat{\theta}_{rfm} = \frac{1}{P}\arctan\left(-\frac{\hat{e}_\alpha}{\hat{e}_\beta}\right) = \frac{\hat{\theta}_{rfe}}{P}. \tag{6.11-2}$$

Thus, $\hat{e}_{\alpha\beta}$ is estimated by the EEMF observer.

The estimated speed $\hat{\omega}_{rfm}$ is obtained with the derivative filter as follows:

$$\hat{\omega}_{rfm} = \frac{p}{\tau p + 1}\hat{\theta}_{rfm}. \tag{6.11-3}$$

where τ is a time constant of the derivative filter.

6.5 Specific Component Reduction Controller (SCRC).

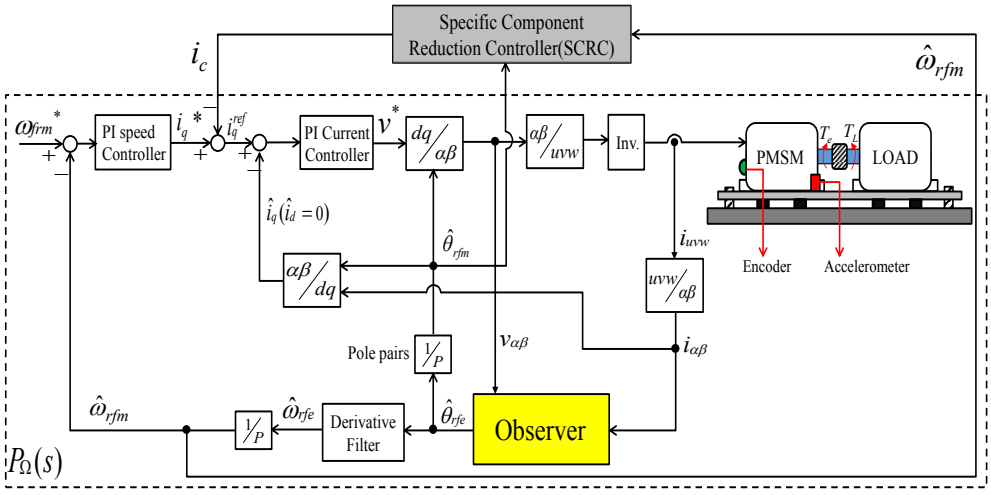

Fig. 6.11 Overall proposed position sensorless vibration suppression system with SCRC.

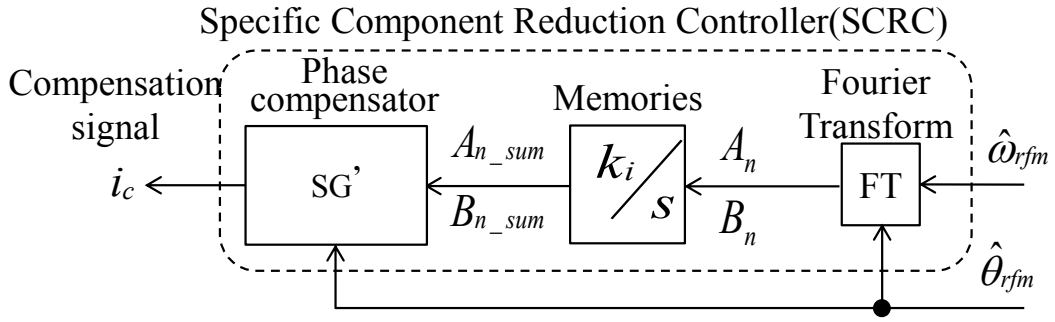

Fig. 6.12 (a) Original form of SCRC.

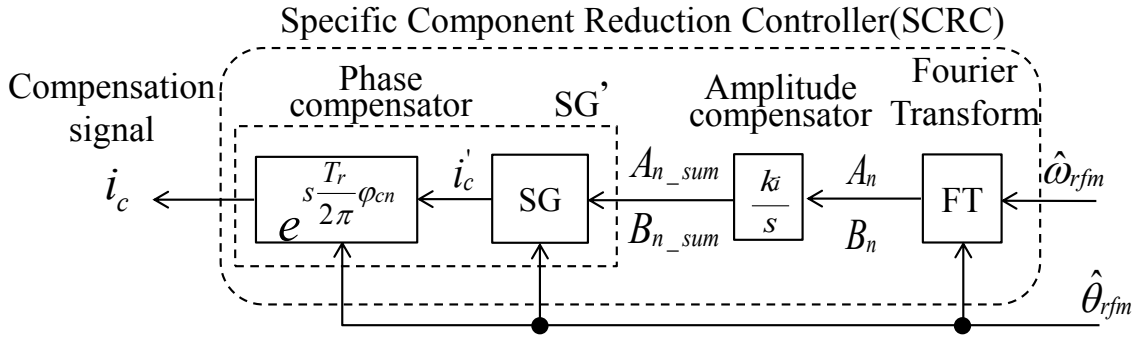

Fig. 6.12 (b) Equivalent form of SCRC.

The whole speed sensorless anti-vibration control system is shown in Fig. 6.4. A modified anti-vibration controller called SCRC is proposed in Fig.6.5(a) and (b). In the SCRC, Fourier coefficients A_n and B_n are extracted by FT, and integrated to generate a compensation signal An_sum and Bn_sum. k_i is the integration gain, and φ_{cn} is the phase compensation gain. The SCRC is unlikely to amplify high frequency noise of $\hat{\theta}_{rfm}$. As there is only one target frequency $1/T_r$ left after FT in Fig.6.5(B), SG_1 is shown as follows:

$$i_c^{'} = A_{n\_sum}\cos(\hat{\theta}_{rfm}) + B_{n\_sum}\sin(\hat{\theta}_{rfm}) \tag{6.12-1}$$

$$\begin{aligned} i_c &= A_{n\_sum}\cos(\hat{\theta}_{rfm} + \varphi_{cn}) + B_{n\_sum}\sin(\hat{\theta}_{rfm} + \varphi_{cn}). \\ &\cong A_{n\_sum}\cos(\frac{2\pi}{T_r}t + \varphi_{cn}) + B_{n\_sum}\sin(\frac{2\pi}{T_r}t + \varphi_{cn}) \end{aligned} \tag{6.12-2}$$

A_{n_sum} and B_{n_sum} can be calculated as:

$$A_{n\_sum} = A_{n\_sum}^{(0)} + k_i\int_0^t A_n(t)dt \tag{6.13-1}$$

$$B_{n\_sum} = B_{n\_sum}^{(0)} + k_i\int_0^t B_n(t)dt$$

Take eq.(16.13-1) into discrete one, it can be shown as follow

$$A_{n\_sun}^{(k+1)} = A_{n\_sun}^{(k)} + k_i T_r A_n^{(k)} \tag{6.13-2}$$

$$B_{n\_sun}^{(k+1)} = B_{n\_sun}^{(k)} + k_i \ T_r B_n^{(k)}$$

Because FT in Fig.6.12 (b) only admits the frequency of target ripple $1/T_r$ into SCRC, $\hat{\theta}_{rfm}$ is almost equal to $(2\pi \cdot t)/T_r$. Even if the harmonics of $\hat{\theta}_{rfm}$ is included in SG, it can be ignored. As when estimated speed $\Delta\hat{\omega}_{rfm}$ feedbacks again, FT will prevent high-frequency component out of SCRC. The calculation of the signal after SG in Fig.6.12 (b) is shown as follows:

$$\begin{aligned} i_c^{(k+1)} &= A_{n\_sum}^{(k+1)} \cos(\frac{2\pi}{T_r} t) + B_{n\_sum}^{(k+1)} \sin(\frac{2\pi}{T_r} t). \\ &= \{A_{n\_sum}^{(k)} \cos(\frac{2\pi}{T_r} t) + B_{n\_sum}^{(k)} \sin(\frac{2\pi}{T_r} t)\} + \\ & k_i T_r \{A_n^{(k+1)} \cos(\frac{2\pi}{T_r} t) + B_n^{(k+1)} \sin(\frac{2\pi}{T_r} t)\} \end{aligned} \tag{6.13-3}$$

In this way, eq.(6.13-3) can be taken as eq.(6.13-4):

$$i_c^{(k+1)} = i_c^{(k)} + k_i T_r \bullet \Delta\hat{\omega}_{rfm} = i_c^{(k)} + \Delta i_c^{(k)} \tag{6.13-4}$$

At last, the compensation signal i_c in Fig.12(c) is

$$i_c = -A_{n\_sum}^{(k)} \cos(\frac{2\pi}{T_r} t + \varphi_{cn}) + B_{n\_sum}^{(k)} \sin(\frac{2\pi}{T_r} t + \varphi_{cn}) \tag{6.13-5}$$

With eq. .(6.13-3) to eq. .(6.13-5), SCRC in the form of Repetitive Controller can be estab -lished. It is shown in Fig6.12 (c).

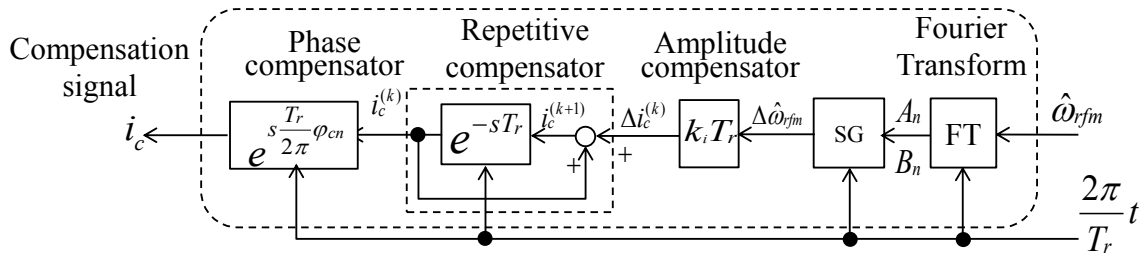

Fig. 6.12(c) SCRC in the form of Repetitive Controller.

From Fig.6.12(c), it can be known that SCRC has no influence of estimated position $\hat{\theta}_{rfm}$, which includes high-frequency noise. And this form of the SCRC is taken into the system analysis in the next section.

Consequently, the stability criterion for determining compensation gain of k_i and φcn in SCRC can be discussed in the next section.

6.6 Stability Analysis

As mentioned above, it is necessary to discuss the stability of the speed sensorless vibration suppression system (with SCRC) shown in Fig. 6.11.

6.6.1 System Equations and Block Diagrams

In order to design the transfer function of $P_\alpha(s)$ in eq.(6.3), assumption that vibration of θ_{rfe}, ω_{rfe}, $\Delta\theta_{rfe}$ and $\Delta\omega_{rfe}$, (Δ denotes perturbation) are sufficiently small for simplicity which is satisfied at relatively middle and high speed over about 300 rpm.

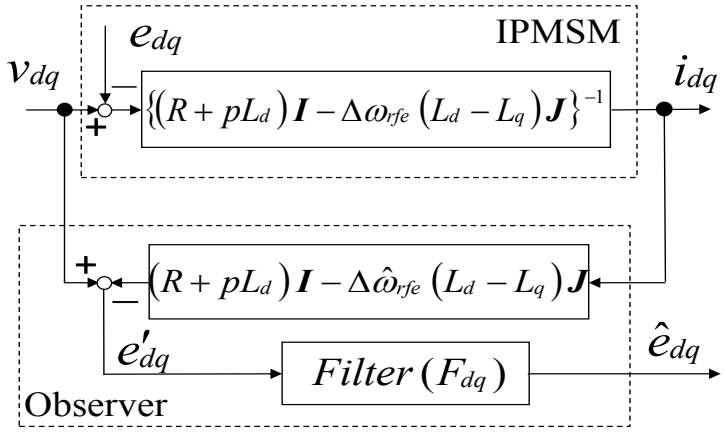

Fig. 6.13 The observer for estimating *d-q* axis component of EEMF.

Fig. 13 shows the observer in *d-q* axes, the model in the *d-q* axes is obtained by transforming eq. (6.8-1) and (6.8-2). Considering eq. (6.14-1) into *d-q* axes, the voltage equation and the EMF equation can be shown as follows

$$\varepsilon^{J\Delta\overline{\omega}_{rfe}t} \equiv \begin{bmatrix} \cos\Delta\overline{\omega}_{rfe}t & -\sin\Delta\overline{\omega}_{rfe}t \\ \sin\Delta\overline{\omega}_{rfe}t & \cos\Delta\overline{\omega}_{rfe}t \end{bmatrix} ; \Delta\overline{\theta}_{rfe} = \Delta\overline{\omega}_{rfe}t \qquad (6.14\text{-}1)$$

$$v_{dq} = \{(R + pL_d)I - \Delta\omega_{rfe}(L_d - L_q)J\}i_{dq} + e_{dq}, \tag{6.14-2}$$

$$e_{dq} = \{(L_d - L_q)(\omega_{rfe} i_d - p i_q) + \omega_{rfe} K_e\} J\varepsilon^{J\,\Delta\theta_{rfe})}.$$

$$v_{dq} = \{(R + pL_d)I - \Delta\hat{\omega}_{rfe}(L_d - L_q)J\}i_{dq} + e'_{dq}. \tag{6.14-3}$$

From eq. (6-14.2) and eq. (6-14.3) as flowing equation is derived

$$e'_{dq} = (\Delta\hat{\omega}_{rfe} - \Delta\omega_{rfe})(L_d - L_q)Ji_{dq} + e_{dq}. \tag{6.14-4}$$

Because in eq.(6.14-4), $\Delta\hat{\omega}_{rfe}$ includes high -frequency noise due to imperfection of motor model, which means e'_{dq} will not be equal to e_{dq}, the filter F_{dq} is applied to observer. As the a result, high-frequency noise of $\Delta\hat{\omega}_{rfe}$ will be reduced, which means $e'_{dq} \cong e_{dq}$.

The position error $\delta\theta_{rfe} = \theta_{rfe} - \bar{\omega}_{rfe}t$ (where $\bar{\omega}_{rfe}$ is the speed average of ω_{rfe}, $\bar{\omega}_{rfe} = \frac{1}{T_r}\int_{ta}^{ta+T_r} \omega_{rfe}dt$, t_a is arbitrary time in one period T_r , and $\bar{\theta}_{rfe} = \bar{\omega}_{rfe}t$) by torque ripple ΔT_{Lrip} is given as

$$\delta\theta_{rfe} = \arctan\left(-\frac{e_d}{e_q}\right) = \arctan\,(-\xi). \tag{6.15-1}$$

$$\Delta(\delta\theta_{rfe}) = \left(\arctan(-\xi)\right)'\Delta\xi = \frac{1}{1+\xi^2}\Delta\xi;$$

$$\Delta\xi = \frac{e_{qo}\,\Delta e_d - e_{do}\,\Delta e_q}{{e_{qo}}^2}. \tag{6.15-2}$$

$$= \frac{e_{qo}\,\Delta e_d - e_{do}\,\Delta e_q}{{e_{do}}^2 + {e_{qo}}^2} = K_d\Delta e_d - K_q\Delta e_q.$$

In the same way,

$$\Delta(\delta\hat{\theta}_{rfe}) = \frac{\hat{e}_{qo}\Delta\hat{e}_d - \hat{e}_{do}\,\Delta\hat{e}_q}{{\hat{e}_{do}}^2 + {\hat{e}_{qo}}^2} = \hat{K}_d\Delta\hat{e}_d - \hat{K}_q\Delta\hat{e}_q. \tag{6.15-3}$$

where θ_{rfe} and $\hat{\theta}_{rfe}$ are the real position and estimated position by providing the perturbation, respectively.

Assuming that at the steady state operation point estimated on *d-q axis* coincides with the real *d-q axis*, eq. (6.16-1) can be got. As a result, eq.(6.16-2) can be given

$$\hat{e}_{do} = e_{do},\ \hat{e}_{qo} = e_{qo}. \tag{6.16-1}$$

$$\hat{K}_d = K_d,\ \hat{K}_q = K_q. \tag{6.16-2}$$

From the eq. (10.1), and with the eq.(9.2), the filter in the rotation coordinate (*d-q* axis) is given by

$$\varepsilon^{-J\bar{\omega}_{rfe}t}\left\{(p+\alpha)I - \bar{\omega}_{rfe}J\right\}\varepsilon^{J\bar{\omega}_{rfe}t}\varepsilon^{-J\bar{\omega}_{rfe}t}\hat{e}_{\alpha\beta} = \varepsilon^{-J\bar{\omega}_{rfe}t}\alpha I e_{\alpha\beta}. \tag{6.17-1}$$

$$\varepsilon^{-J\bar{\omega}_{rfe}t}\left\{\bar{\omega}_{rfe}J + (p+\alpha)I - \bar{\omega}_{rfe}J\right\}\varepsilon^{J\bar{\omega}_{rfe}t}\hat{e}_{dq} = \alpha I e_{dq}. \tag{6.17-2}$$

Where $e^{J\bar{\omega}_{rfe}t}$ is rotation vector. As mentioned above, the vibration of $\Delta\omega_{rfe} = \omega_{rfe} - \bar{\omega}_{rfe}$ is very small, the rotation vector can also be used.

The estimated back EMF from eq.(6.17-2) is shown as

$$\begin{aligned}\begin{bmatrix}\hat{e}_d\\ \hat{e}_q\end{bmatrix} = I\hat{e}_{dq} &= \frac{\alpha}{(p+\alpha)} I e_{dq} = \frac{\alpha}{(p+\alpha)}\begin{bmatrix}e_d\\ e_q\end{bmatrix}\\ &= F_{dq}\begin{bmatrix}e_d\\ e_q\end{bmatrix}.\end{aligned} \tag{6.17-3}$$

$$F_{dq} = \frac{\alpha}{p+\alpha}. \tag{6.17-4}$$

The giving perturbation to the eq. (6.17-3), eq. (6.18) is driven.

$$\begin{bmatrix}\Delta\hat{e}_d\\ \Delta\hat{e}_q\end{bmatrix} = \frac{\alpha}{p+\alpha}\begin{bmatrix}\Delta e'_d\\ \Delta e'_q\end{bmatrix} \cong \frac{\alpha}{p+\alpha}\begin{bmatrix}\Delta e_d\\ \Delta e_q\end{bmatrix}. \tag{6.18}$$

From eq. (6.15-2), (6.15-3), (6.16-1), (6.16-2) and (6.18), the relationship between real position and estimated one is given as

$$\frac{\Delta\hat{\theta}_{rfe}}{\Delta\theta_{rfe}} = \frac{P*\Delta\hat{\theta}_{rfm}}{P*\Delta\theta_{rfm}} = \frac{\alpha}{p+\alpha}. \tag{6.19}$$

Assuming that : the position angle error $\delta\theta_{rfm} = \hat{\theta}_{rfm} - \theta_{rfm}$ is sufficiently small ($cos\delta\theta_{rfm} \cong 1$); the current controller on $\hat{d}$-$\hat{q}$ axis is performed as an ideal state because current controller loop gain is high enough when the SCRC is operated in the relatively

low frequency region; and $\hat{\imath}_d = 0$, the motor torque T_e is given as eq. (6.20) where $\hat{\imath}_q$ is the current on the estimated q-axis calculated by $\hat{\theta}_{rfm}$. As a result, the relationship between the real speed and the estimated speed is given as the first-order low-pass filter shown in eq. (6.17-4).

$$T_e = PK_{ef} i_q = PK_e \hat{i}_q \cos\delta\theta_{rfm} \cong PK_e \hat{i}_q \cong PK_e i_q^{ref} \tag{6.20}$$

By using the equations (6.20), considering eq. (6.6-2) and eq. (6-19) with respect to the perturbed variables (ΔI_{dq}, $\Delta\Omega_{rfm}$, *and* $\Delta\hat{\Omega}_{rfm}$) around the steady state operating points (I_{dq0}, Ω_{rfm0}, *and* $\hat{\Omega}_{rfm0}$), $\Delta T_e = L\{\Delta\tau_e\}$, Fig. 6.14 is obtained. In Fig. 14, the transformation $G_1(s)$, $G_2(s)$,$G_3(s)$ *and* $G_4(s)$ are given:

$$G_1(s) = \frac{\Delta T_e}{\Delta \hat{I}_q^{ref}} = PK_e. \tag{6.21}$$

$$G_2(s) = \frac{\Delta\Omega_{rfm}}{\Delta T_{dif}} = \frac{(J_f + J_r)s^2 + D_f s + K_f}{J_r s(J_f s^2 + D_f s + K_f)}. \tag{6.22}$$

$$G_3(s) = \frac{\Delta\hat{\Omega}_{rfm}}{\Delta\Omega_{rfm}} = \frac{\alpha}{s+\alpha}. \tag{6.23}$$

$$G_4(s) = \frac{\Delta I_q^{ref}}{\Delta\hat{\Omega}_{rfm}} = -\frac{K_{ps}s + K_{is}}{s}. \tag{6.24}$$

where $G_1(s)$ is the torque equation gain by eq. (6.20), $G_2(s)$ is the motor mechanics from eq. (6.6-2), $G_3(s)$ is the filter in observer derived from eq. (6.19), and $G_4(s)$ is the PI controller. ΔI_c is generated by the repetitive controller to suppress estimated speed ripple in $\Delta\hat{\Omega}_{rfm}$ which is estimated by speed estimator. The load torque ΔT_L is a disturbance torque due to load torque ripple.

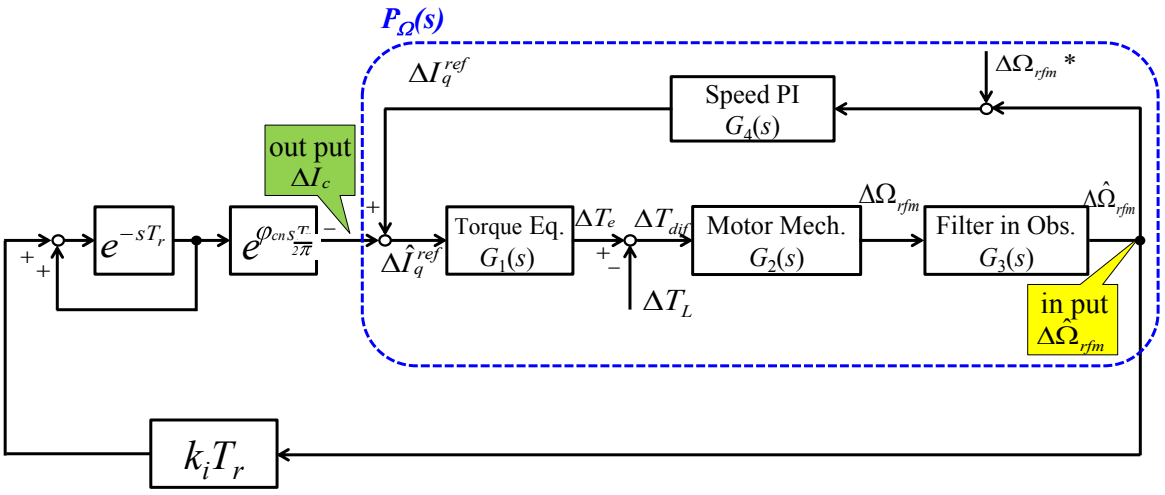

Fig. 6.14 Proposed system diagram of the linear approximation vibration suppression system.

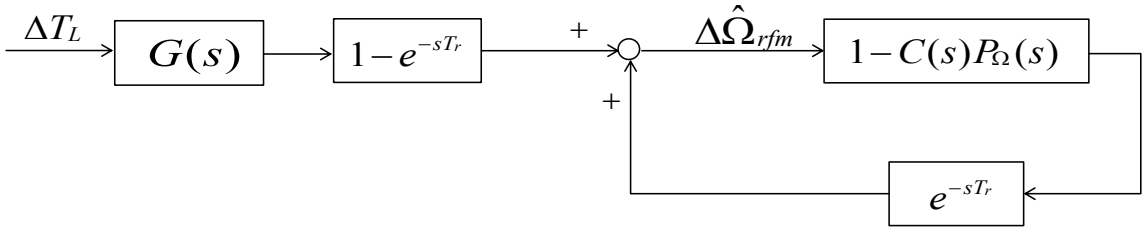

Fig. 6.15 Transformed equivalent block diagram(in case without FT).

6.6.2 Stability System

As mentioned in section IV-C, the SCRC is shown in Fig. 6.11 can be regarded as the repetitive controller with FT and SG so that the concept discussed in section II-B can also be used for this system. To achieve this aim, focusing on the input of repetitive controller $\Delta\hat{\Omega}_{rfm}$, the block diagram shown in Fig. 6.14 is transformed into one shown in Fig. 6.15. With the same theory of eq. (6.4)

$$\left|1-C(j\omega_n)P_\Omega(j\omega_n)\right|<1 \; for \;\; \omega_n=2\pi nf. \tag{6.25}$$

The transfer functions in Fig. 6.15 are shown as follows:

$$\begin{aligned} P_\Omega(s) &= \frac{\Delta\hat{\Omega}_{rfm}}{\Delta I_c} \\ &= [1+G_1(s)G_2(s)G_3(s)G_4(s)]^{-1}G_1(s)G_2(s)G_3(s). \end{aligned} \tag{6.26}$$

$$C(s) = k_i T_r e^{\varphi_{cn} sTr} . \tag{6.27}$$

$$G(s) = \frac{\Delta\hat{\Omega}_{rfm}}{\Delta T_L} = G_2(s)G_3(s). \tag{6.28}$$

Where, $P_{\Omega}(s)$: transfer function of motor and the torque ΔI_c to $\Delta\hat{\Omega}_{rfm}$.

$C(s)$: transfer function of proportional compensator and time leading element.

$G(s)$: transfer function from ΔT_L to $\Delta\hat{\Omega}_{rfm}$.

6.6.3 SCRC gain k_i, φ_{cn}

Fig. 6.16 shows the Nyquist loci of $1\text{-}C(j\omega)\,P_{\Omega}(j\omega)$, with the phase compensation gain element (φ_{cn} = 1.8). Now the specific points on loci, corresponding to the fluctuation angular frequency ω_{rfm} component extracted by FT, the Nyquist analysis is considered in the case of SCRC according to the criteria expressed in eq. (6.4). In 3 cases (A, A' and A"), the operation point A" stays outside the unit circle, which means that the SCRS will be unstable at this point. Then, an operating point can be moved into the unit circle by reversing the sign of k_i shown in Fig.6.16 (a) (A"→A), where reversing the sign of k_i means reversing the phase. However, B" shown in Fig. 6.16 (b) can not be moved into the unit circle with reversing k_i. In such a case, the operation point can be moved into the unit circle by using the phase compensator gain φ_{cn} (B"→B).

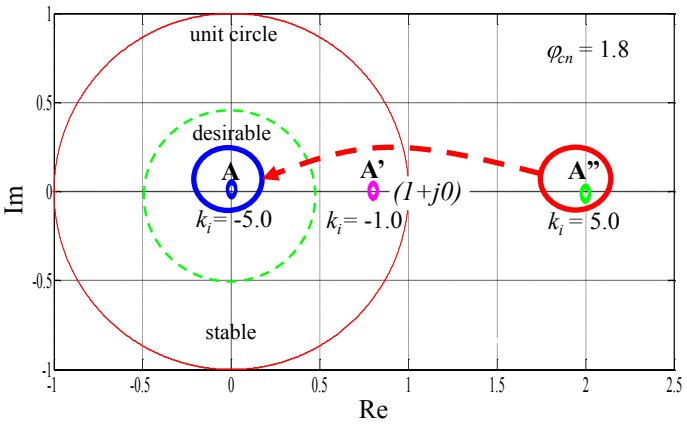

$$C(s) = k_i T_r e^{\varphi_{cn} sT_r}$$

$$C(j\omega_n) = k_i T_r e^{j\omega_n T_r \varphi_{cn}}$$

Parameters adjust:
k_i = variable,
φ_{cn} = 1.8

(a) Case A: when the operating point exits outside of the unit circle (φ_{cn} = 1.8), and reverse signs of k_i.

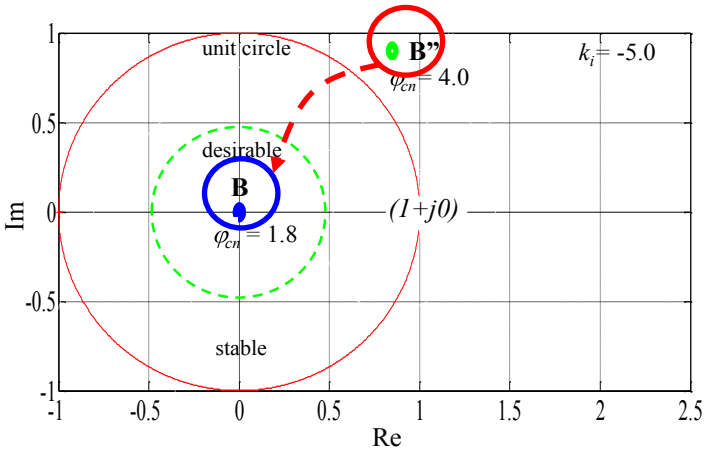

$$C(s) = k_i T_r e^{\varphi_{cn} s T_r}$$

$$C(j\omega_n) = k_i T_r e^{j\omega_n T_r \varphi_{cn}}$$

Parameters adjust:
k_i = -5,
φ_{cn}= variable

(b) Case B: when the operating point exits outside of the unit circle with the phase control sign of φ_{cn}.

Fig. 6.16 Nyquist loci of transfer function $1\text{-}C(j\omega_n)\,P_\Omega(j\omega_n)$: Stability analysis results (●: the operating point of the 10 [Hz]).

The stabilization of the SCRC control system is designed as follows:

1) From eq. (6.25) means that all points on the Nyquist plot transfer function of $1\text{-}C(j\omega_n)\,P_\Omega(j\omega_n)$ must stay inside the unit circle for stable operation(the time leading element φ_{cn} =1.8) as shown in Fig. 6.16(a), and the The ω_n is angular frequency of vibration extracted by the Fourier Transformer (FT), the Nyquist plot starts from a point $1 + j0$. On the other hand, the frequency of vibration signal is selected by the FT before inputted to SCRC in proposed system.

2) Most Nyquist points (operating points) other than the resonance point exist near the point $1 + j0$. We can see in Fig.6.16 that if the value of k_i is small, a loci of vector will be expanded centering on the point $1 + j0$. In the case operating points exist inside the unit circle, so the operating points can be then apart from the circumference of the unit circle, convergence speed of the vibration can be made quick(for example, A' operation point in Fig 6.16(a). On the other hand, in the case operating points exist outside the unit circle, the operating points are apart from the unit circle greatly and divergence speed of the vibration will become quick (for example, A" operation point in Fig.6.16(a)). Therefore, it is advisable to set large value on *ki*, unless it causes inconvenience for the convergency of the vibration as shown in experiment results (Fig. 6.19).

3) Nyquist operation point stays near the original point, from the view point of faster convergence of the speed vibration, which menas that $H(j\omega_n)$, defined as

$$H(j\omega_n) = 1 - C(j\omega_n) P_\Omega(j\omega_n). \tag{6.29}$$

Is nearly zero, that is $H(j\omega_n) \cong 0$. Thi s condition is useful from the view point of stability

margine. That is, when the parameters of the system is changed and than the position of $H(j\omega_n)$ moves to the complex plane, the $H(j\omega_n)$ still stay inside the unit circle . this meanes that, the original point of $H(j\omega_n)$ is near origin.

From $H(j\omega_n)$=0 ,

$$C(j\omega_n) \cong \frac{1}{P_\Omega(j\omega_n)}. \tag{6.30}$$

$$P_\Omega(j\omega_n) = A_\Omega e^{(j\varphi_\Omega)}. \tag{6.31}$$

With eq. (6.30) and eq. (6.31) k_i and φ_{cn} can be got as follows:

$$\begin{cases} k_i = \dfrac{1}{A_\Omega T_r} \\ \varphi_{cn} = -\varphi_\Omega \end{cases} or \begin{cases} k_i = -\dfrac{1}{A_\Omega T_r} \\ \varphi_{cn} = -\varphi_\Omega \pm \pi \end{cases}. \tag{6.32}$$

Therefore, the operation point can be moved within the unit circle by adjusting the gain of k_i *and* φ_{cn}. This means that the control system will be stable. We can be calculated the actual parameters stabilization of the near origin point as shown in Fig. 6.17.

It should be pointed out that the EEMF position Sensorless system loses the stability in the relatively low speed region. And in the experimental system, the speed is fluctuated if the load torque is not constant. The low speed region is defined as speed less than 300 [rpm]. Above the base speed of 600 [rpm], the experiments have been carried out. In our system, the speed command both 600[rpm] and 1200[rpm] have been tested to prove the stability of SCRC.

6.6.4 Frequency Response Analysis

In Fig. 6.15, eq. (6.26) is used for designing the gains of k_i and φ_{cn} so that it is necessary to validate the plant $P_\Omega(s)$. To achieve this aim, the signal i_c was injected shown in eq. (6.33), and the response of the estimated speed $\hat{\omega}_{rfm}$ was measured.

$$i_c = A\sin\omega_{in}t. \tag{6.33}$$

Fig. 17 shows the experiment results compared with the theoretical result of $P_\Omega(j\omega)$ shown in eq. (6.26). These results indicate that both results have almost the same characteristics. Based on the results, the appropriate parameters used in the experiment were same values as shown in Fig. 6.15 as Section V, be taken to stability control in the experiment. The error are occurred from the parameter error and modely error of the motor.

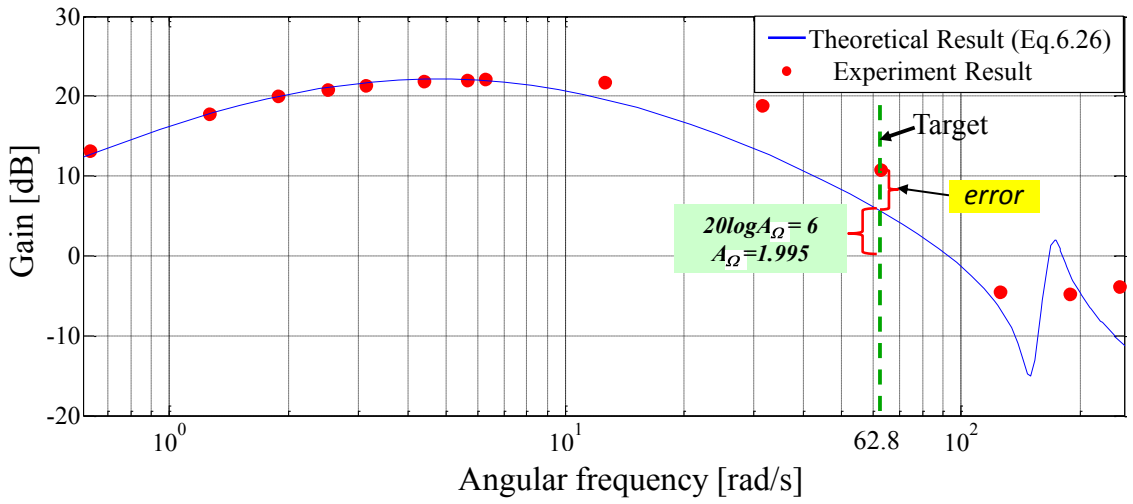

(a) Bode plot of gain [dB].

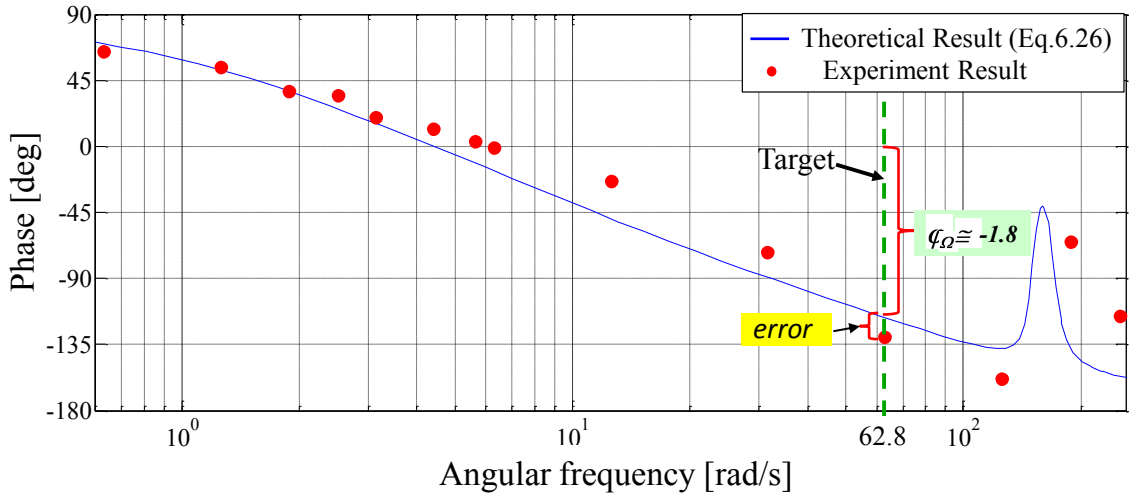

(b) Bode plot of phase[deg]

Fig. 6.17 Bode plots of transfer function $P_\Omega(s)$.

It should be pointed out that the EEMF position sensorless system loses the stability in lower speed region. And in the experimental system, the speed fluctuates if the load torque is not constant, in lower speed region less than about 300 [rpm]. Above the base speed of 600 [rpm], the current vector is controlled in order to produce the maximum torque under the current limitation. So the experiments will be carried out in the middle-high speed region over 300 [rpm]. In our system, the speed command from 600[rpm] to 900[rpm] will be tested to prove the stability of SCRC in middle-high speed.

6.7 Experiment

6.7.1 Experimental Setup

The proposed SCRS shown in Fig. 6.12 is implemented into the DSP (TMS320C6713) system of Myway Corporation. An experimental setup is depicted in Fig. 6.18. The experimental parameters are shown in Table I and Table II. With the theory of the system stability analysis shown in section V, the integration gain k_i and phase gain φ_{cn} are designed.

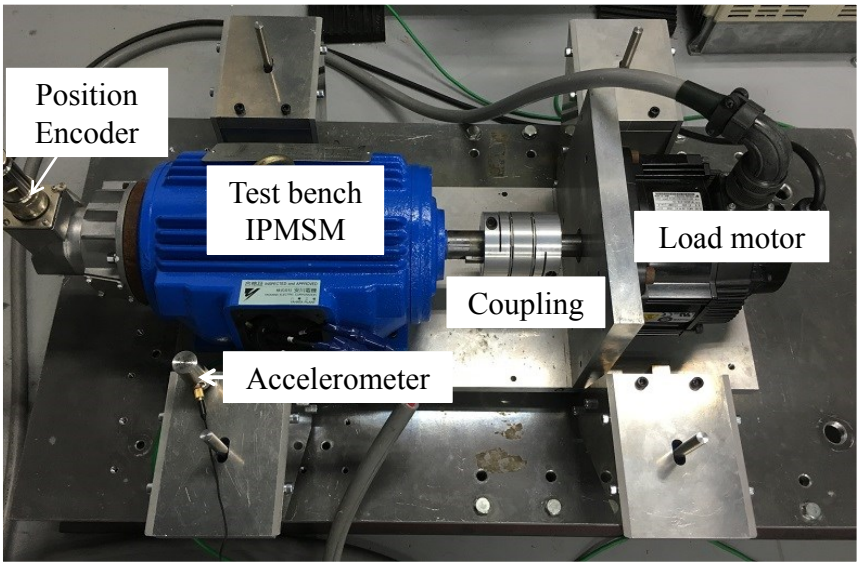

Fig. 6.18 Overall of experiment system.

The experiment is carried out with the speed command ω_{rfm}* = 600 [rpm] and the load torque $T_L = 2.0 + 2.0\sin\theta_{rfm}$ [N]. The load torque T_L is generated by a servo motor. At 1 [s], the anti-vibration control starts to suppress the torque ripple T_{Lrip}.

TABLE 1

Motor Parameters

IPMSM (Test Bench)		
Rated power	[W]	750
Rated speed	[rpm]	1750
Rated current	[A]	3.5
Number of pole pairs	P_S	3
Stator Resistance	R [Ohm]	1.25
d-axis inductance	L_d [H]	0.0168
q-axis inductance	L_q [H]	0.0218
EMF constant	K_e [V·s/rad]	0.255
Motor inertia	J_r [kg·m^2]	0.0055
Servo motor (Load Motor)		
Rated power	[W]	850
Rated speed	[rpm]	1500
Rated current	[A]	6.9

TABLE II

Experimental Parameters

Inverter		
DC-link voltage	[V]	200
Carrier frequency	[kHz]	10
Controller		
Control period	[μs]	100
Fourier sampling period	[μs]	1300
Speed command	$2\pi/60\omega_{rfm}$* [rpm]	600-900,1200
Speed controller Proportional gain	k_{ps} [A·s/rad]	0.08
Speed controller Integral gain	k_{is} [A/rad]	0.14
Current controller cutoff frequency	[rad/s]	5000
SCRC integration gain	k_{i}	-5.0, -9.6
SCRC phase gain	φ_{cn}	1.8, 0.022
Pole of disturbance observer	α [rad/s]	$0.5\omega_{rfe}$
	β [rad/s]	ω_{rfe}
Load torque	T_L [Nm]	$2.0 + 2.0\sin\theta_{rfm}$

6.7.2 Experimental Results

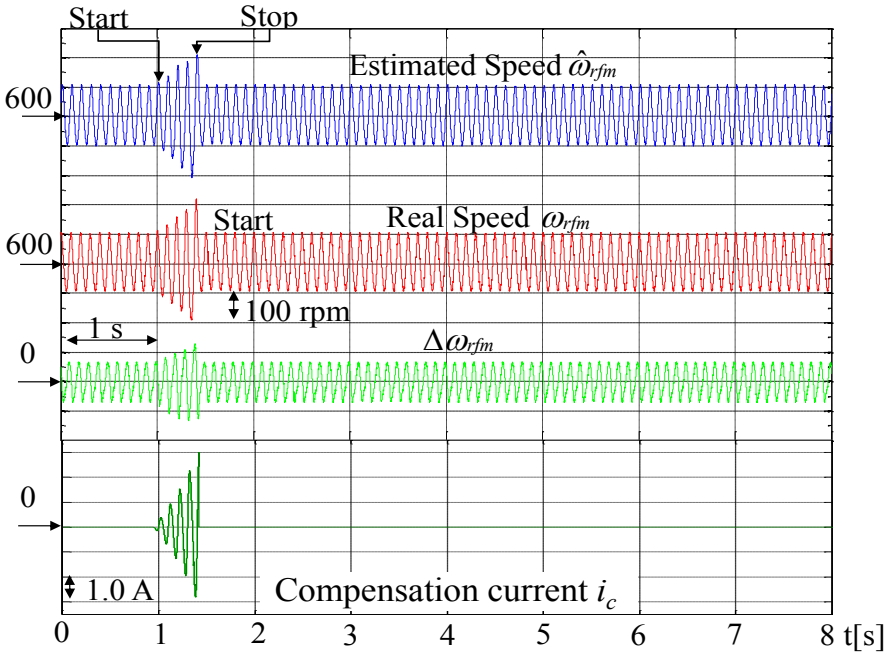

Fig. 6.19 Case A'': Rotor speed and compensation current.

Fig. 6.19 (Case A'': Operation point outside of unit circle "unstable case") shows the motor speed and the compensation current. After starting the vibration suppression, the speed ripple is diverged (selected parameters of gain k_i and φ_{cn} were not suitable) by the compensation current (i_c) produced from the SCRC. In addition, at time 1.4 [s], the waveform has returned to the condition before starting of the vibration suppression control because the compensation current has stopped due to rated current limiter.

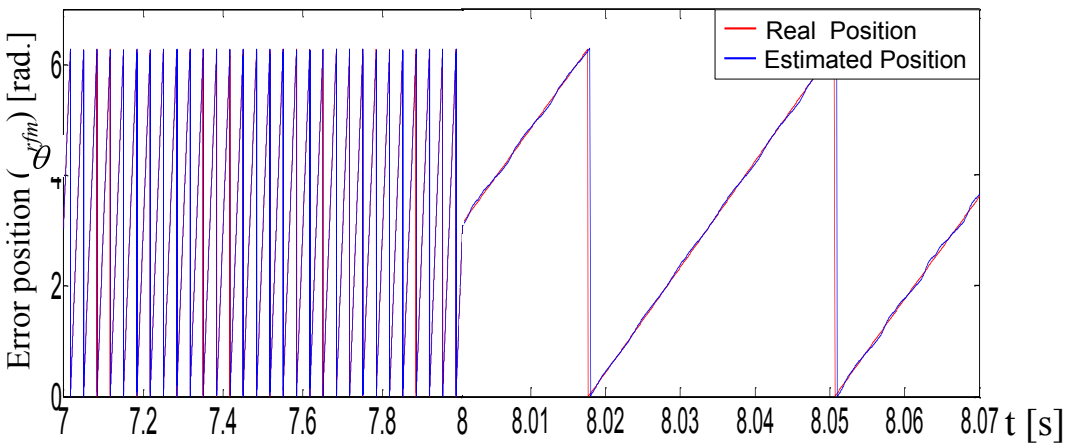

Fig. 6.20 Case A: The estimated position $\hat{\theta}_{rfm}$ and real position θ_{rfm}.

Fig. 6.20 shows the position estimation result and real position (at the steady state of 600 [rpm]). And it has confirmed the validity of the control system estimation by SCRC with EEMF observer.

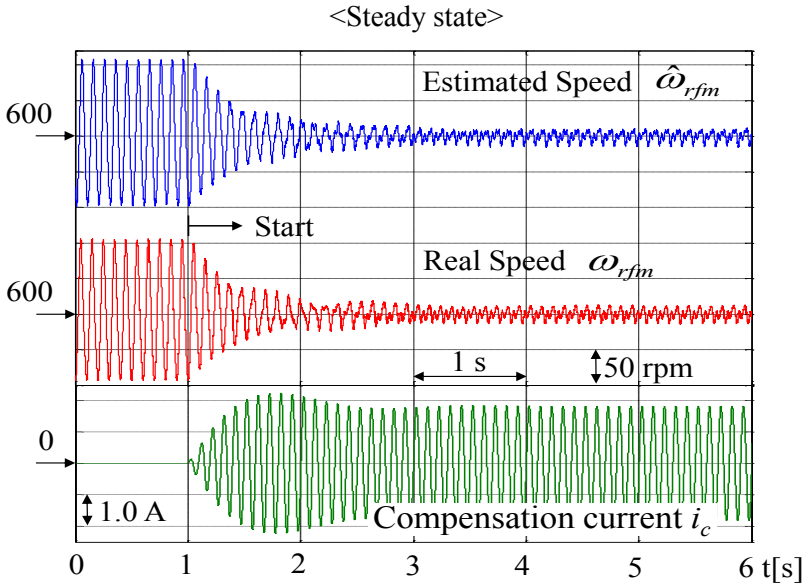

Fig. 21 Case A: Rotor speed and compensation current (f=10[Hz]).

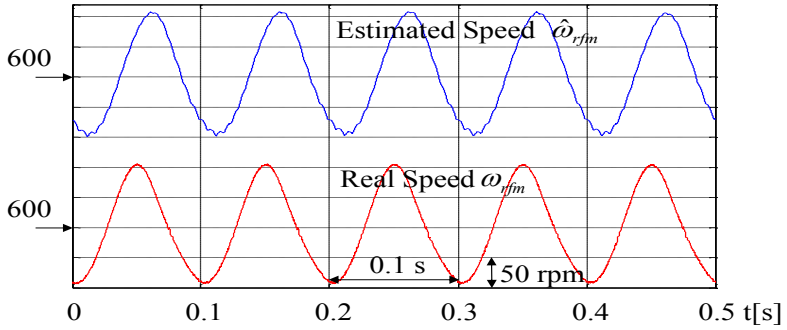

(a) Before compensation.

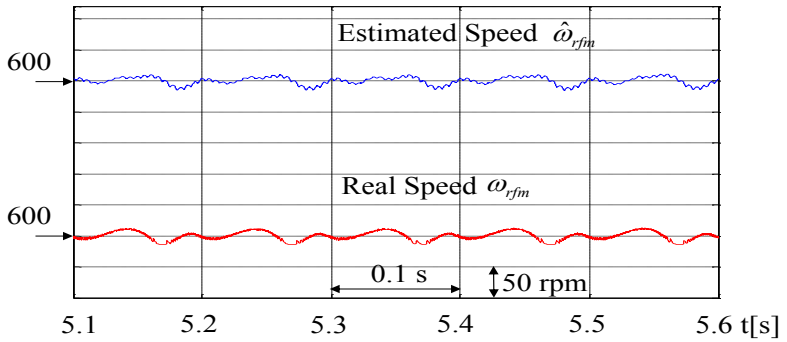

(b) After compensation(steady state)

Fig. 22 Case A: Enlarged view of rotor speed(f = 10 [Hz]).

Fig. 21 (case A: an operation point near center of the unit circle "stable case") shows the experimental of the rotor real speed ω_{rfm}, the estimated speed $\hat{\omega}_{rfm}$, and the compensation current (i_c) generated by SCRC. The current (i_c) suppresses ripple in the rotor speed $\hat{\omega}_{rfm}$. Fig. 22 (a) and (b) shows the enlarged view of the rotor speeds ω_{rfm} and $\hat{\omega}_{rfm}$, which is before and after compensation, respectively.

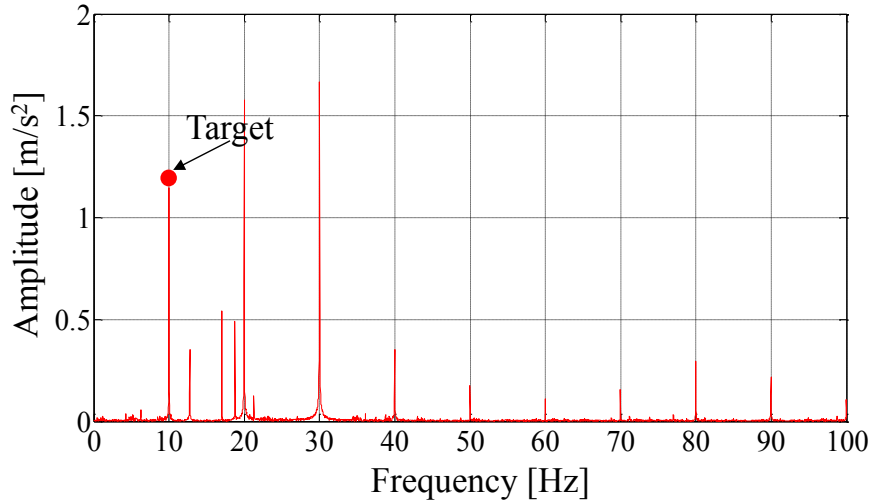

(a) Before compensation

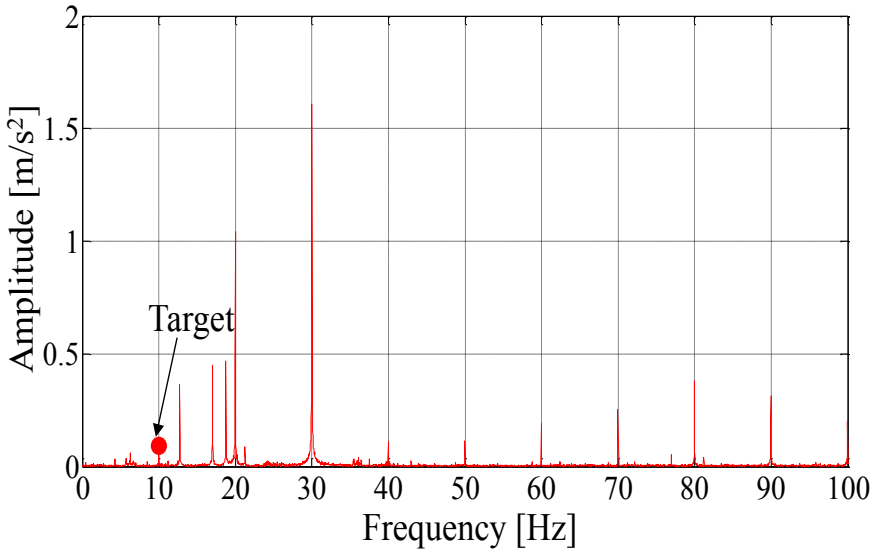

(b) After compensation

Fig. 23 Case A: FFT analysis of frame vibration (accelerometer) (f = 10 [Hz]). .

Fig. 23 (a) and (b) show FFT analysis of the frame vibration, respectively. The target

harmonic (10 [Hz] component) is approximately 96% reduced by SCRC. These results indicate that SCRC under sensorless speed control is useful for suppressing position dependent torque ripple which causes the frame vibration.

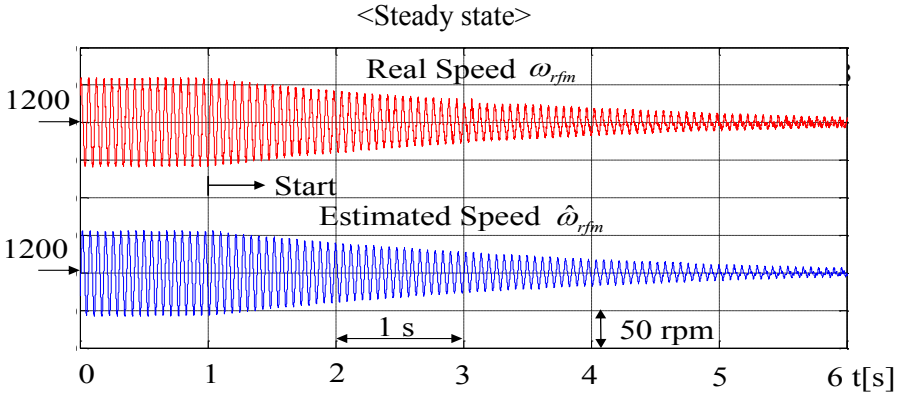

(a) Before adjusting parameters k_3= -5.0, k_4=0.018.

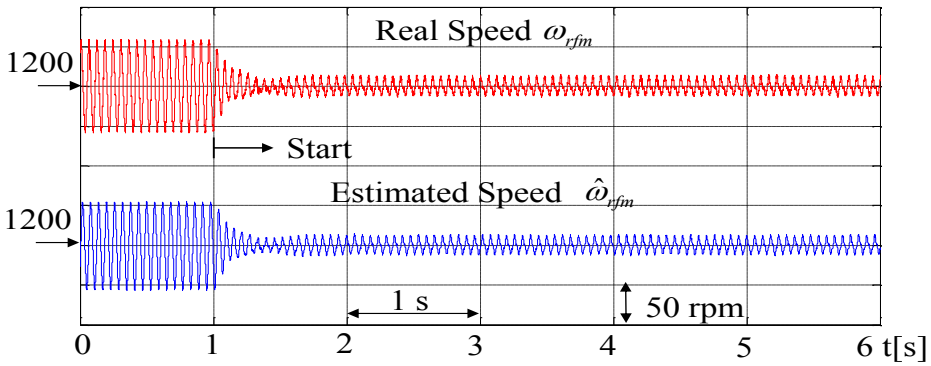

(b) After adjusting parameters k_i = -9.6, φ_{cn} = 0.022.

Fig. 24 Improvement of speed estimation ability by suppression of rotor speed (f=20[Hz]).

Fig. 24 shows the experimental result when f = 20[Hz]. In Fig.24 (a), the experiments before adjusting k_i and φ_{cn} is shown. Fig.24(b) shows the experimental result after adjusting the parameters k_i and φ_{cn}. It is necessary to select parameters k_i and φ_{cn} to keep the system stable.

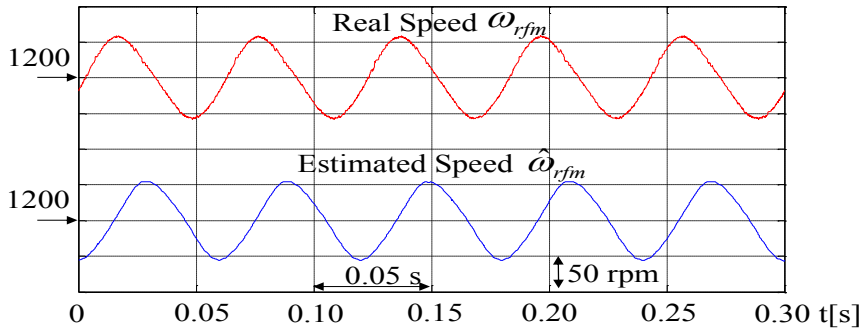

(a) Before compensation.

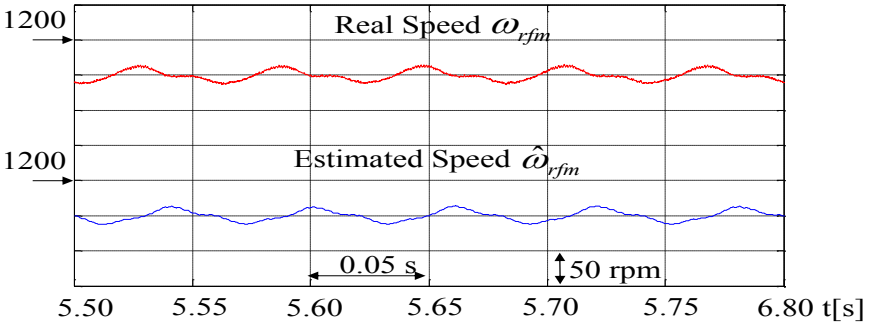

(b) After compensation(steady state)

Fig. 25 After adjusting the parameters (k_i and φ_{cn})Enlarged view of rotor speed (f = 20 [Hz]).

Fig. 25(a) and (b) shows the enlarged view of the rotor speeds ω_{rfm} and $\hat{\omega}_{rfm}$, which is compared between ones before and after compensation, respectively.

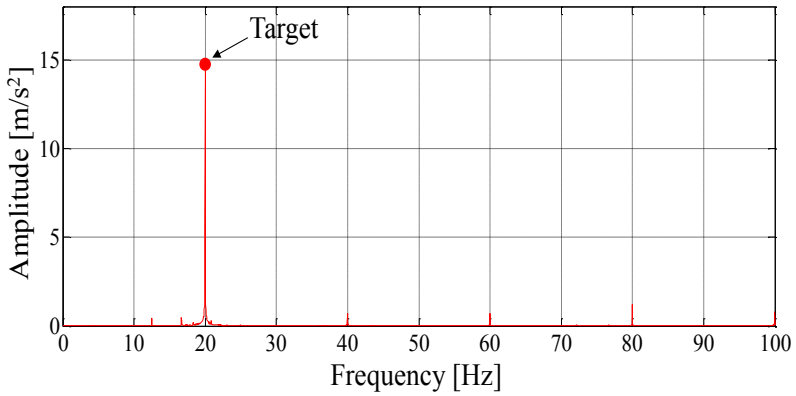

(a) Before compensation.

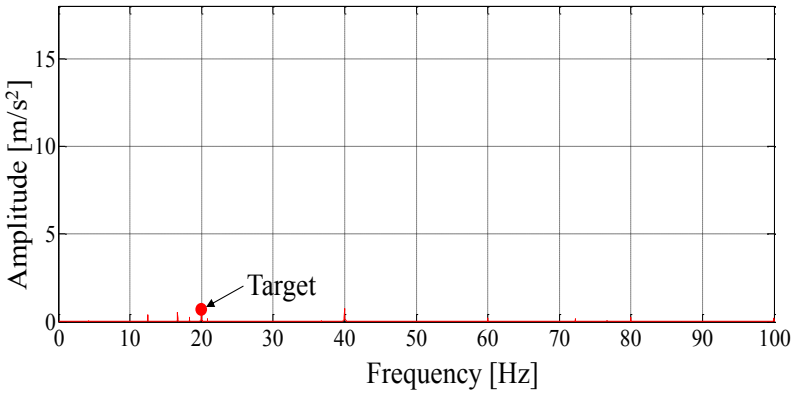

(b) After compensation.

Fig. 26 Case A: FFT analysis of frame vibration (accelerometer).

Fig. 26(a) and (b) show FFT analysis of the frame vibration, respectively. It can be confirmed that the mechanical vibration is also considerably reduced too. The target harmonic (f = 20 [Hz] component) is approximately 92% reduced by SCRC.

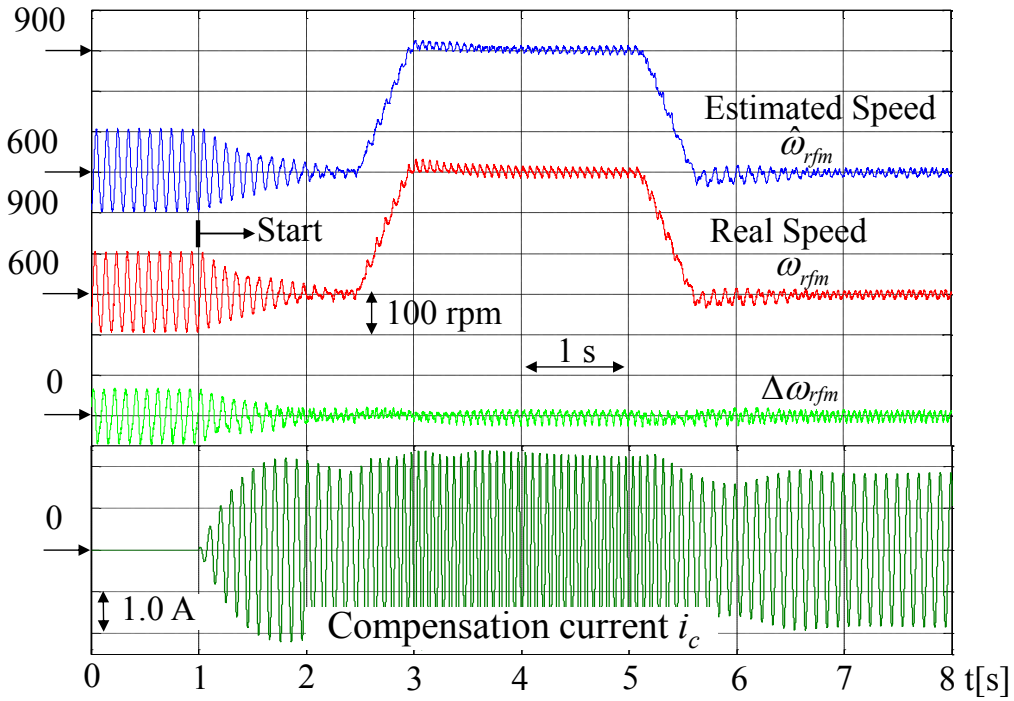

Fig. 6.27 Case A: Rotor speed and compensation current.

Fig. 6.27 (case A: an operation point near center of the unit circle "stable case") shows the rotor real speed ω_{rfm}, the estimated speed $\hat{\omega}_{rfm}$, and the compensation current (i_c) generated by SCRC. In Fig. 27, the acceleration and deceleration of the motor speed between 600 [rpm] and 900 [rpm] are also shown. The speed error $\Delta\omega_{rfm}$ has to be a small

values in the acceleration and deceleration areas. The current (i_c) suppresses ripple in the rotor speed $\hat{\omega}_{rfm}$. Fig. 6.28 (a) and (b) shows the enlarged view of the rotor speeds ω_{rfm} and $\hat{\omega}_{rfm}$, which is before and after compensation, respectively.

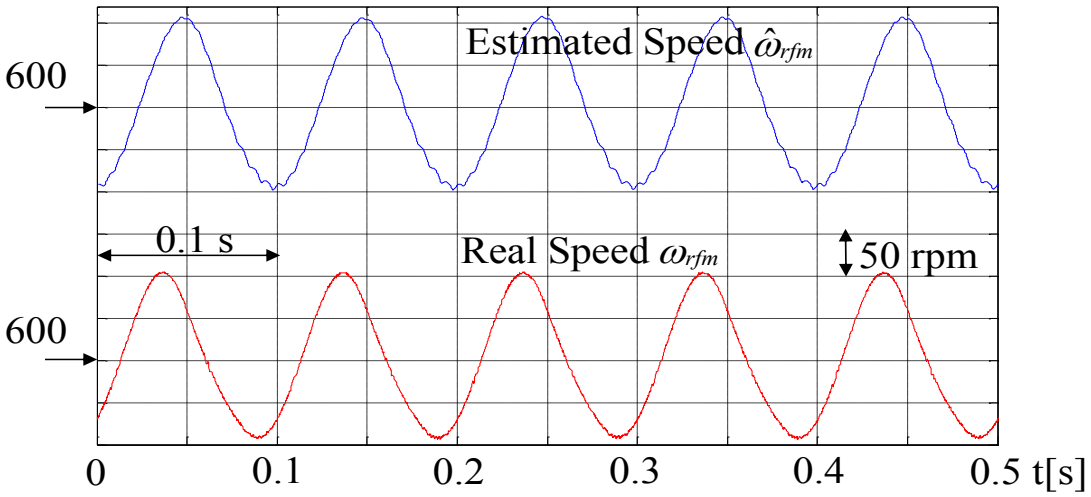

(c) Before compensation.

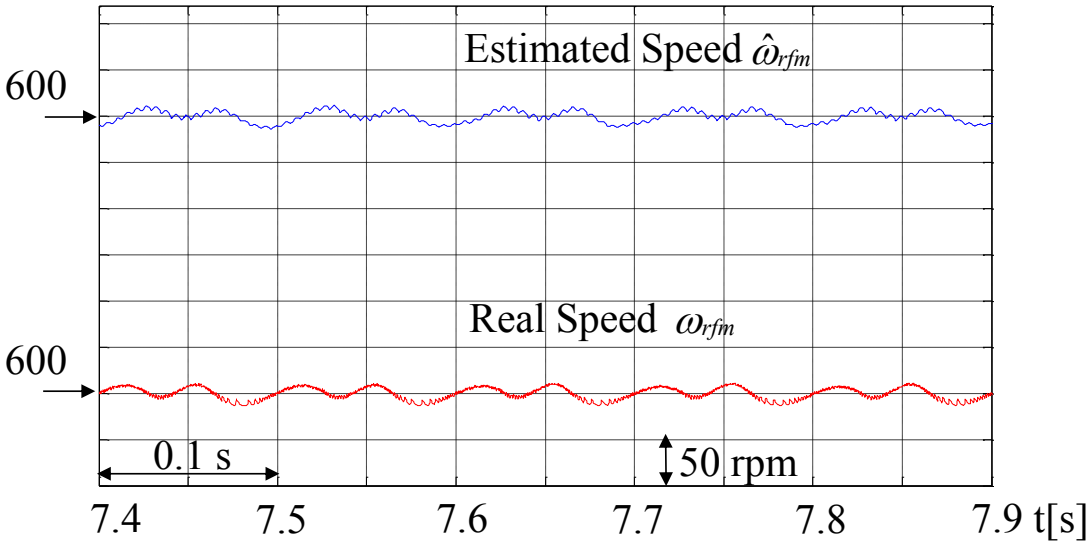

(d) After compensation

Fig. 6.28 Case A: Enlarged view of rotor speed.

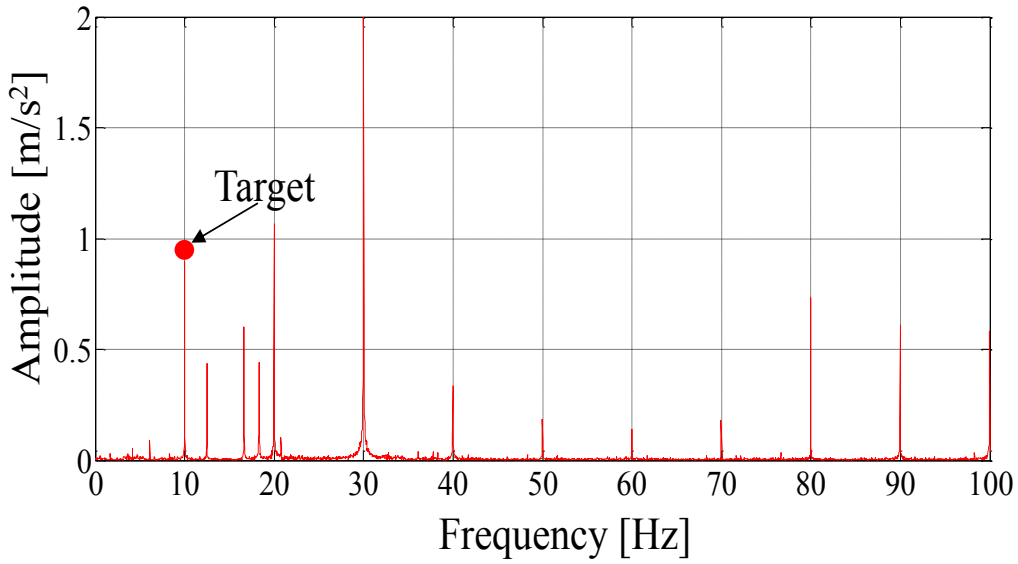

(a) Before compensation

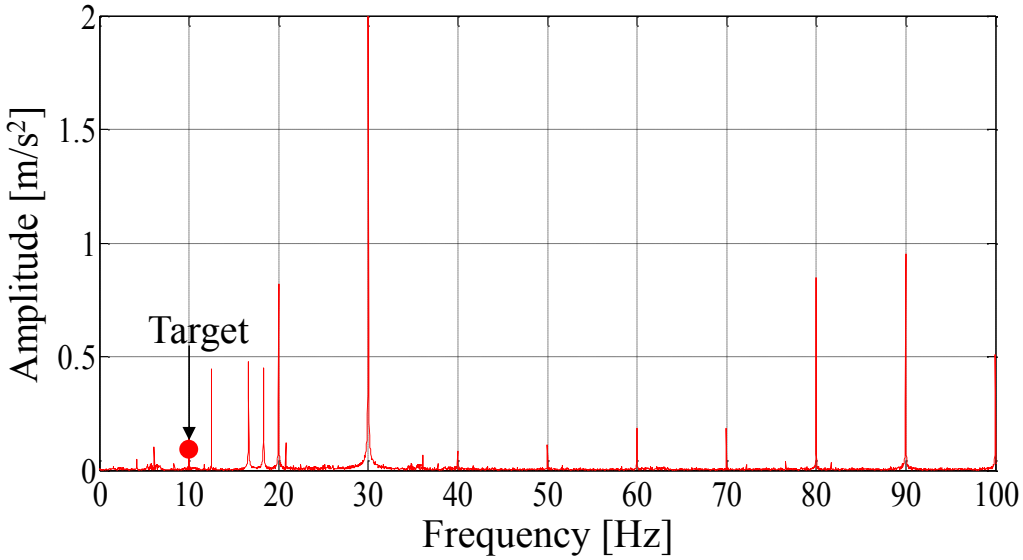

(b) After compensation

Fig. 6.29 Case A: FFT analysis of frame vibration (accelerometer).

Fig. 6.29(a) and (b) show FFT analysis of the frame vibration, respectively. The target harmonic (10 [Hz] component) is approximately 94% reduced by SCRC. These results indicate that SCRC under sensorless speed control is useful for suppressing position dependent torque ripple which causes the frame vibration.

6.8 Conclusions

In this paper, a novel anti-vibration controller named SCRC without position sensors and accelerometers has been proposed. The torque ripple which causes the frame vibration is reduced by SCRC which utilizes the estimated speed from the EEMF observer. System stability analysis has been given to stabilize the system with the gain of k_i and φ_{cn}. Experimental results show that the proposed method is useful for suppressing periodic load torque. The speed variable sensorless anti-vibration control also can be achieved with SCRC.

Future work of us will focus on the stability analysis in different speed region, especially in low speed region. Harmonics frequencies which are different from the speed command frequency will also be considered.

References

[1] T. Su, S. Hattori, M. Ishida, and T. Hori, “Suppression control method for torque vibration of ac motor utilizing repetitive controller with Fourier transform,” IEEE Trans. Ind. Appl., vol. 38, no. 5, pp. 1316–1325, Sep 2002.

[2] M. Zhang; Y. Li; T. Zhao; Z. Liu; L. Huang, "A speed fluctuation reduction method for sensorless PMSM-compressor system," in Industrial Electronics Society, 2005. IECON 2005. 31st Annual Conference of IEEE , vol., no., pp.5 pp.-, 6-10 Nov. 2005

[3] A. Shimada, K. Kawai, T. Zanma, S. Doki, and M. Ishida, “Sensorless Suppression Control for Frame Vibration of PMSM,” IEEJ Trans., vol. 128, no. 11, pp. 1246-1253, 2008

[4]

[5] J. Kim; K. Nam, "Speed ripple reduction of PMSM with eccentric load using sinusoidal compensation method," in Power Electronics and ECCE Asia (ICPE & ECCE), 2011 IEEE 8th International Conference on, vol., no., pp.1655-1659, May 30 2011-June 3 2011

[6] T. Yamaguchi, Y. Tadano, N. Hoshi, “Torque Ripple Suppression Control by Periodic Disturbance Observer with Model Error Correction,” IEEJ Trans., vol.134, no. 2, pp.185-192, 2014

[7] Z. Chen, M. Tomita, S. Doki, and S. Okuma, “An extended electromotive force model for sensorless control of interior permanent magnet synchronous motors,” IEEE Trans. Ind. Electron., vol. 50, no. 2, pp. 288–295, Apr 2003.

[8] K. Kato, M. Ishida, “Vibration suppression control by suppression of ripple of estimated velocity using repetitive controller for position sensorless control system of PMSM,” IEEJ, MD/LD conference 2013, MD-13-62, LD-13-124, pp.115-119, 2013.

[9] D. S. Naidu, Optimal Control System, Idaho State University Pocatello, Idaho, UAS, 1940.

[10] S. Hattori, M. lshida and T. Hori, "Suppression Control Method for Torque Vibration of Brushless DC Motor Utilizing Repetitive Control with Fourier Transform," IEEE Trans. Ind. Electron., pp.427-432, 2000.

[10] M. lshida, Tinghsu Su, Hattori, S. and Hori T., ”Suppression Control Method for torque Vibration of AC motor utilizing repetitive controller with Fourier Transformer” Industry Applications Conference of IEEE, vol.3

Chapter 7

SIMULATANEOUS VIBRATION SUPPRESSION CONTROL FOR SENSORLESS PMSM DRIVEN BY UTILIZING MULTIPLE-SPECIFIC CONPONENT REDUCTION CONTROL METHOD

This paper proposes a suppression control method of the motor frame vibration caused by the torque ripple, the speed fluctuation reducing method for sensorless Permanent Magnet Synchronous Motor(PMSM). This controller is called Multiple Specific Component Reduction Controller (M-SCRC). An earlier method utilizes the compensation signals by the SCRC with the Fourier Transform. It can work without accelerometer, requiring the rotor speed and position estimated by Extended Electromotive Force (EEMF). But it can only compensate the signal which is the same frequency with mechanical speed command. This paper mainly consists of the following parts. Firstly, the Configuration of Control System will be given. Secondly, Simultaneous Vibration suppression Control and Stabilization of Vibration Suppression Control System will be shown. Thirdly, the experimental results show the effectiveness of the proposed system. At last it is the conclusion.

7.1 Load Torque Ripple

In motor drive application, causes of torque ripple are roughly categorized as either motor-based or load-based one. The factors based on motor include cogging torque and spatial harmonics of flux. They present a high-frequency torque ripple such as 6^{th} harmonics of motor electrical speed. Torque ripples based on load side consist of load torque ripple $\Delta\tau_{Lrip}$. They present torque ripples with relatively low-frequency such as *1/P, 2/P, 3/P* (*P* = number of motor pole pair).

This paper targets in the system which the motor and load are integrated. In this system, the frame vibration is caused by the load torque ripple $\Delta\tau_{Lrip}$. The mechanical dynamics of motor

frame and rotor in PMSM and load are given as

$$\Omega_{rfm} = M_{rf}(T_e - T_L) = M_{rf}\ T_{dif}. \tag{7.1}$$

$$M_{rf}(s) = \frac{(J_r + J_f)s^2 + D_f s + K_f}{J_r s(J_f s^2 + D_f s + K_f)}. \tag{7.2}$$

$$\tau_L = \tau_{L0} + \Delta\tau_{Lrip}\ . \tag{7.3}$$

$$\Delta\tau_{Lrip} = \sum_{n=1}^{\infty} A_{\tau Lrip}\ \sin(n\theta_{rfm}). \tag{7.4}$$

where $A\tau_{\mathrm{Lrip}}$ is the amplitude of the load torque ripple. The load torque ripple $\Delta\tau$Lrip is the *nth* order sinusoidal wave. As a result, the periodic speed ripple $\Delta\omega_{\mathrm{rip}}$ is expressed as

$$\Delta\omega_{rip} = \sum_{n=1}^{\infty} A_{\omega rip}\ \sin(n\theta_{rfm} + \varphi_{\omega rip}). \tag{7.5}$$

7.2 Simultaneous Vibration suppression Control: Multiple-Specific Component Reduction Control (MSCRC)

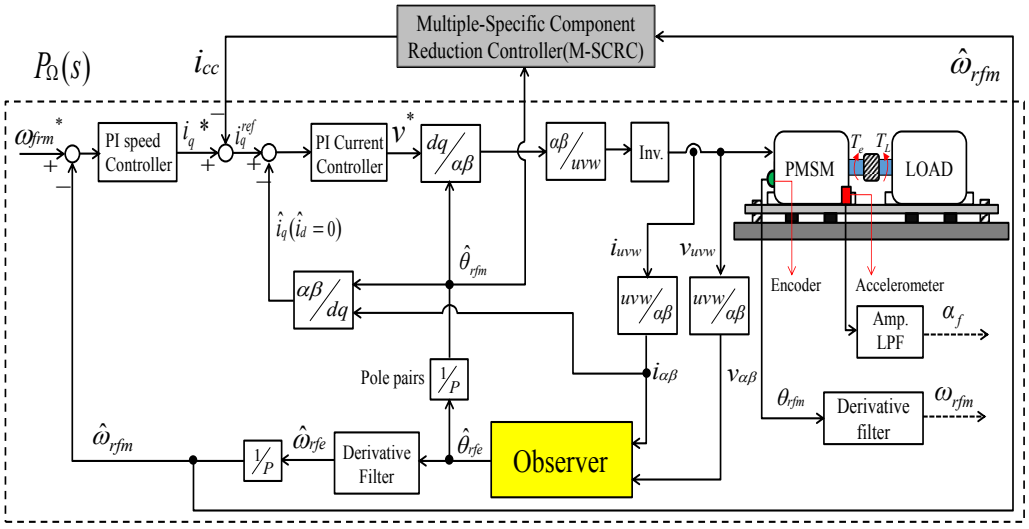

Fig. 7.1 Overall proposed position sensorless vibration suppression control system with M-SCRC.

7.2.1 Overall Configuration

Fig. 7.1 shows the overall proposed position and seed sensorless vibration suppression system with Multiple-Specific Component Reduction Control (MSCRC). Fig.

7.1 consists of three control systems. Three control systems are motor control system, sensorless control system(Observer)[6,11] and MSCRC.

7.2.2 Control Configuration

The vibration suppression control part in Fig. 7.1 is constructed as shown in Fig. 7.2. In Fig. 7.2(b), the compensation signal i_{cc} generator obtained off-line. The detail of M-SCRC part, *index n* is the number of the oscillating frequency to be considered, $\hat{\omega}_{rfm}=[\hat{\omega}_{rfm}\ \ \hat{\omega}_{rfm_2}...\hat{\omega}_{rfmn}]^T$, $k_c=[k_{c1}\ \ k_{c2}...k_{ci}]^T$ and $\varphi_c=[\varphi_{c1}\ \ \varphi_{c2}...\varphi_{ci}]^T$. As shown in Fig. 7.2(b), the MSCRC control system past consist of the integral compensation k_{ci} to adjust control

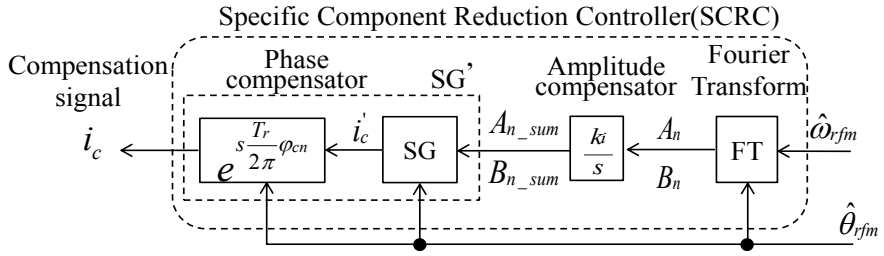

Fig. 7.2(a) Original form of the Specific Component Reduction Control (SCRC)[11] with the one target frequency component.

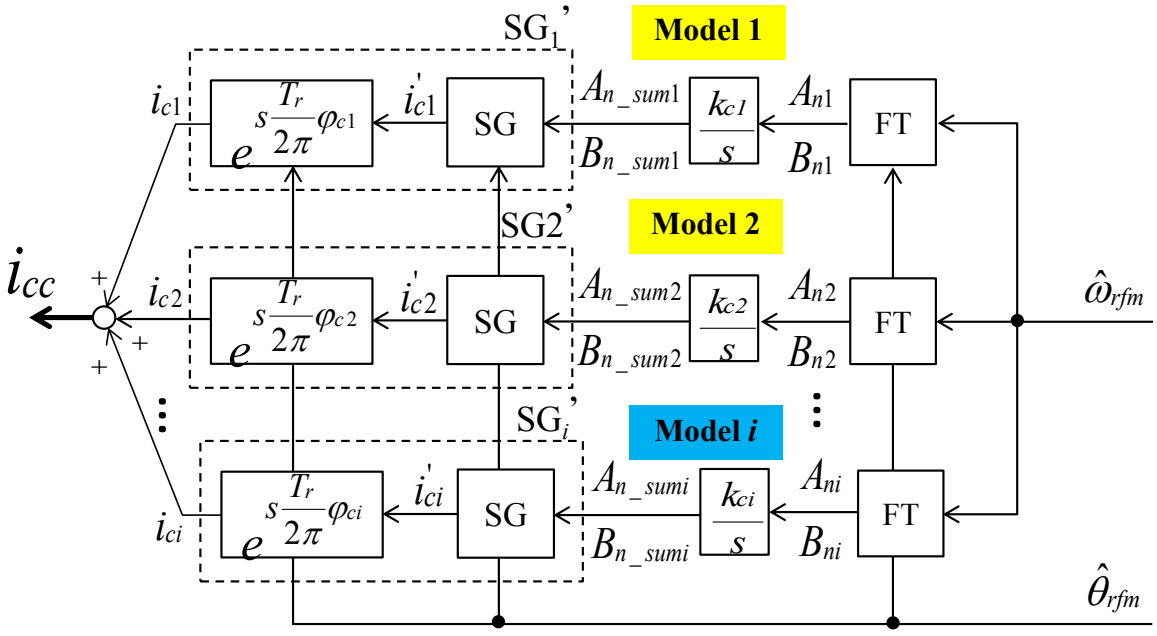

Fig. 7.2(b) Detail of Multiple-Specific Component Reduction Control (MSCRC).

loop gain and phase compensation φ_{ci} to compensate phase lag. The Fourier Transform coefficients A_n and B_n are extracted by FT, integrated to generate a compensation signal A_{n_sum} and B_{n_sum}. The MSCRC is unlikely to amplify high frequency noise of $\hat{\theta}_{rfm}$. As there are the multi-target fluctuation frequency component left after FT in Fig.7.2 (b), the output signal of SG and SG' are shown as follows:

$$i'_{ci} = A_{n\_sumi}\cos(\hat{\theta}_{rfm}) + B_{n\_sumi}\sin(\hat{\theta}_{rfm}). \tag{7.6-1}$$

$$i_{ci} = A_{n\_sumi}\cos(\hat{\theta}_{rfm} + \varphi_{ci}) + B_{n\_sumi}\sin(\hat{\theta}_{rfm} + \varphi_{ci}). \tag{7.6-2}$$

The earlier method SCRC utilizes the compensation signal i_{cc} while MSCRC is generated from the sum of i_{c1} and i_{c2}.

In the earlier work [11], SCRC is applied to each frequencycofficients, extracted by Fourier Transform and the compensational signal is generated in the SCRC simultaneously for the vibration suppression control. After generating compensation signal for the last CPU period, the compensation signal is generated again by renewed A_{ni} and B_{ni}. *In MSCRC* each compensation signal can suppress its corresponding frequency component of the estimated angular speed $\Delta\hat{\omega}_{\mathrm{rfm}}$.Thus, all the compensation signals are obtained by n time initiation of the procedure. As a result, MSCRC requires time to suppress the target frequencies.

On the other hand, MSCRC with Fourier Transform (FT) expansion is applied simultaneously in the proposed configuration. SCRC is applied for only target frequency component. Therefore, the proposed MSCRC is capable of reducing multipled target frequency components, which is improved compared with conventional method [11].

Consequently, the stability criterion for determining compensation gain of k_{ci} and φ_{ci} in MSCRC will be discussed in the next section.

7.3 MSCRC parameters k_{ci} and φ_{ci}

In the MSCRC system, following condition should be satisfied for all selected frequency components $\hat{\omega}_{\mathrm{rfm}}$ n_i (i=1, 2,...m) :

$$|1 - C_i(j\omega_n)\, P_\Omega(j\omega_n)|<1,\ i=1,\ 2,\ldots m \tag{7.7}$$

$$C_i(s) = k_{ci}T_r e^{s\frac{T_r}{2\pi}\varphi_{ci}}. \tag{7.8}$$

As mentioned above, it is necessary to set the MSCRC control parameters k_{ci} and φ_{ci} properly so that the vibration suppression control system is stable. Fig. 7.3 shows the Nyquist plot of $1\text{-}C(j\omega n)\, P_\Omega(j\omega n)$. The Nyquist plot analysis is considered according to the criteria expressed in eq. (7.7). Fig. 7.3(a) shows the different operation point, 600 [rpm] (corresponding to f = 10[Hz]). The operation point (A"n_1,n_2) stays out of the unit circle,

which means that the MSCRC will be unstable at this point. Then, an operating point can be moved into the unit circle by reversing the sign of k_{ci} shown in Fig. 7.3(a) (A"n_1,n_2)→(An_1,n_2). Reversing the sign of k_{in} means phase shift by π. Fig. 7.3 (b) shows the different operation point, 800[rpm](corresponding to f = 13.33 [Hz]). However, (Bn_1,n_2) shown in Fig. 7.3 (b) uses the same method to move each operation point into original of the unit circle by appropriating the parameters k_{ci} and φ_{ci}. In the simultaneous case, the operation point (B'n_1,n_2) can be moved into the unit circle by using the same condition in (An_1,n_2) can be desirable condition.

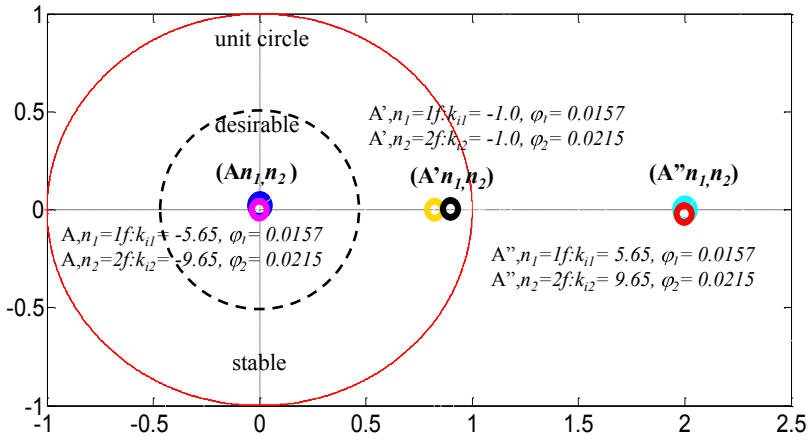

(a) Case A: The different operation point, 600 [rpm] (corresponding to f = 10[Hz]).

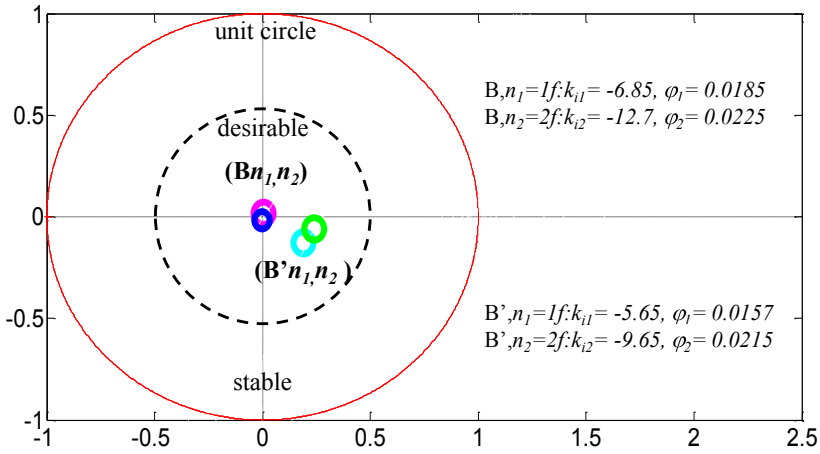

(b) Case B: The different operation point, 800 [rpm] (corresponding to f = 13.33[Hz]).

Fig. 7.3 Nyquist plot of transfer function *(1-C(s) P_Ω(s)<1)*

7.4 Experiments

7.4.1 Experiment System

The performance of the proposed transducer-less Vibration suppression control for sensorless PMSM driven has been investigated using the experimental drive system shown in Fig. 7.4, The proposed MSCRC has been implemented in the DSP (TMS320C6713) of Myway Corporation. The experimental parameters are shown in Table 7.1 and Table 7.2.

The experiment is carried out with the speed command ω_{rfm}* = 600 [rpm], 800 [rpm] and ω_{rfm}* = 600 [rpm] to 800 [rpm]with the load torque $T_L = 0.9 + 0.9 \sin\theta_{rfm}$ [N]. The load torque T_L is generated by a servo motor. At 1 [s], the suppression vibration control starts to suppress the torque ripple T_{Lrip}. Load torque τ_L is generated by the generator, and load torque is controlled by i_{qload}.

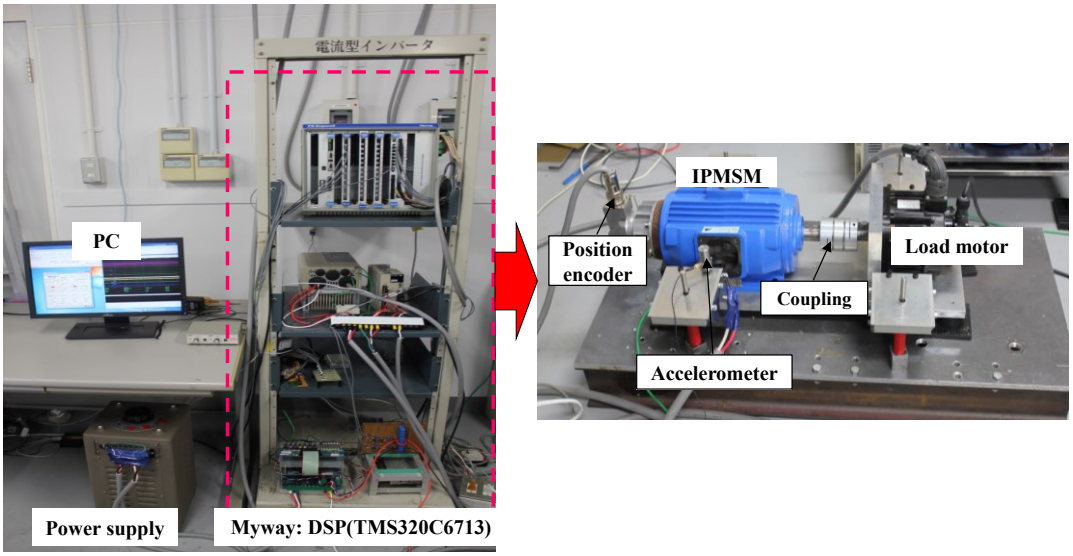

Fig. 7.4 Overall of experiment system.

Table 7.1: Motor Parameters.

IPMSM (Test Bench)		
Rated power	[W]	750
Rated speed	[rpm]	1750
Rated current	[A]	3.5
Number of pole pairs	P_S	3
Stator Resistance	R [Ohm]	1.25
d-axis inductance	L_d [H]	0.0168
q-axis inductance	L_q [H]	0.0218
EMF constant	K_e [V·s/rad]	0.255
Motor inertia	J_r [kg·m^2]	0.0055
Frame inertia	$J_f[kg \bullet m^2]$	0.0207
Frame viscous coefficient	$D_f[kg \bullet m^2/s]$	0.108
Frame rubber coefficient	$K_f[N/mm]$	148.54
Servo motor (Load Motor)		
Rated power	[W]	850
Rated speed	[rpm]	1500
Rated current	[A]	6.9

Table 7.2: Experimental Parameters.

Inverter		
DC-link voltage	[V]	200
Carrier frequency	[kHz]	10
Controller		
Control period	[μs]	100
Fourier sampling period	[μs]	1300
Speed command	ω_{rfm}* [rpm]	600 : 800
Speed controller Proportional gain	k_{ps} [A·s/rad]	0.08
Speed controller Integral gain	k_{is} [A/rad]	0.14
Current controller cutoff frequency	[rad/s]	5000
MSCRC integration gain	k_{ci}	-5.65:-9.65/ -6.85 : -12.7
MSCRC phase gain	φ_{ci}	0.0157, 0.0215/ 0.0185, 0.225
Pole of disturbance observer	α [rad/s]	0.4*ω_{rfe}
	β [rad/s]	ω_{rfe}
Load torque	T_L [Nm]	0.9 + 0.9sinθ_{rfm}

7.4.2 Experiment Results

Fig. 7.5 and Fig. 7.6 show a result of the proposed method at different operating point, the rotor speed 600 [rpm] (corresponding to 10 [Hz]). It can be seen that the simultaneous vibration suppression control is successful at the other operation points. The target frequency are n_1 = 90% and n_2 = 85% reduced by MSCRC as shows in Fig. 7.5. If the Nyquist point is out of the unit circle Case (A*"*n_1,n_2), the speed vibration suppression is out of work as shown in Fig.7.6.

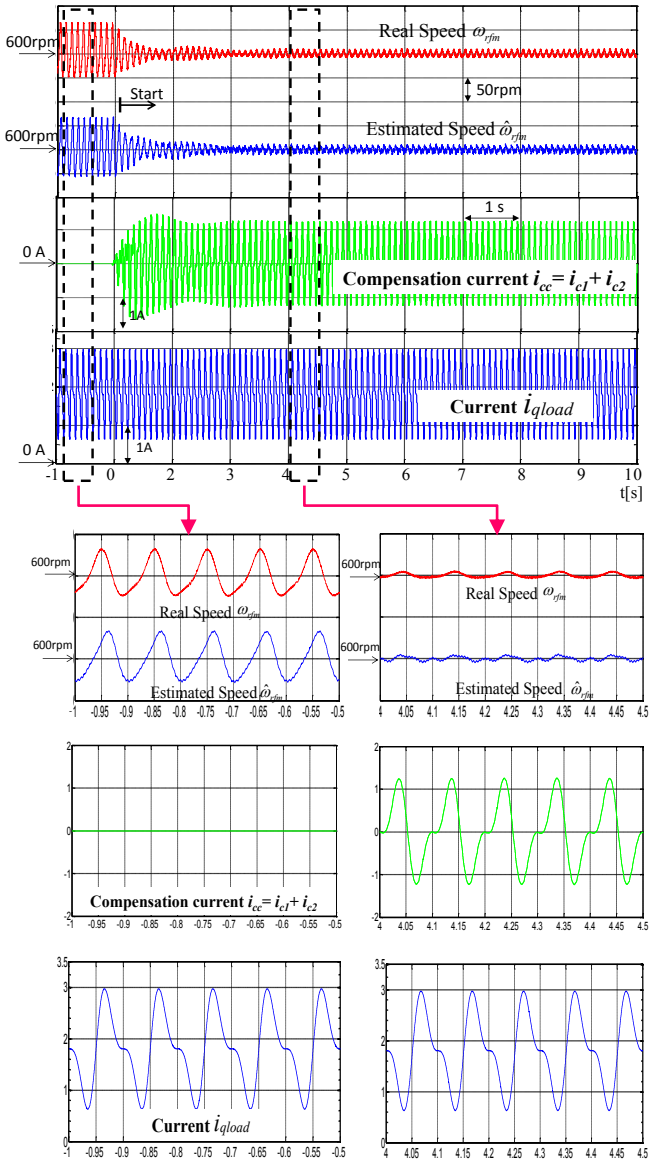

(a) Before Compensation. (b) After Compensation.

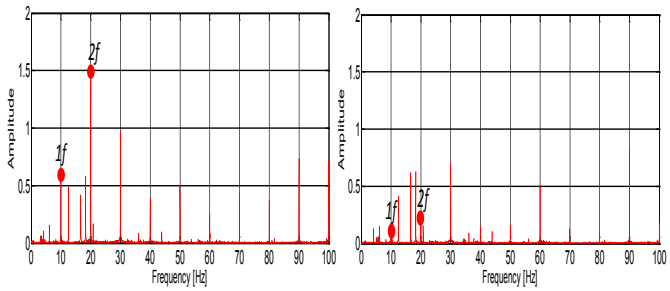

(b)Before Compensation. (b) After Compensation.

Fig. 7.5 Case (An_1,n_2): Experimental by the proposed method at a different operating point, the rotor speed 600 [rpm] (f = 10 [Hz])/ Enlarged view and FFT analysis.

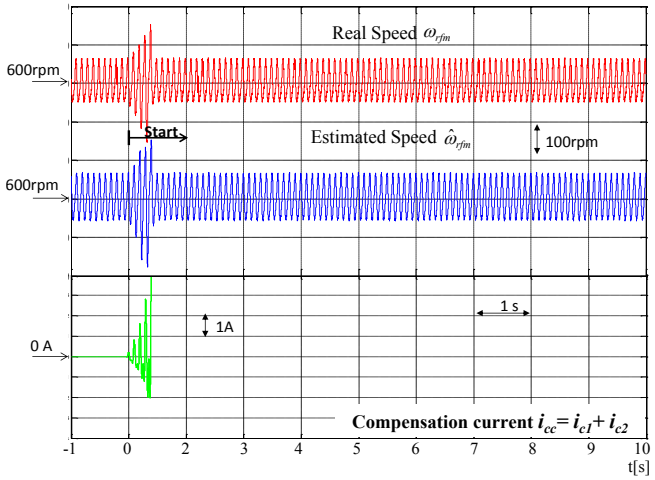

Fig. 7.6 Case (A*"*n_1,n_2): "Unstable case" at different operating point, the rotor speed 600 [rpm] (f = 10 [Hz]). Enlarged view and FFT analysis.

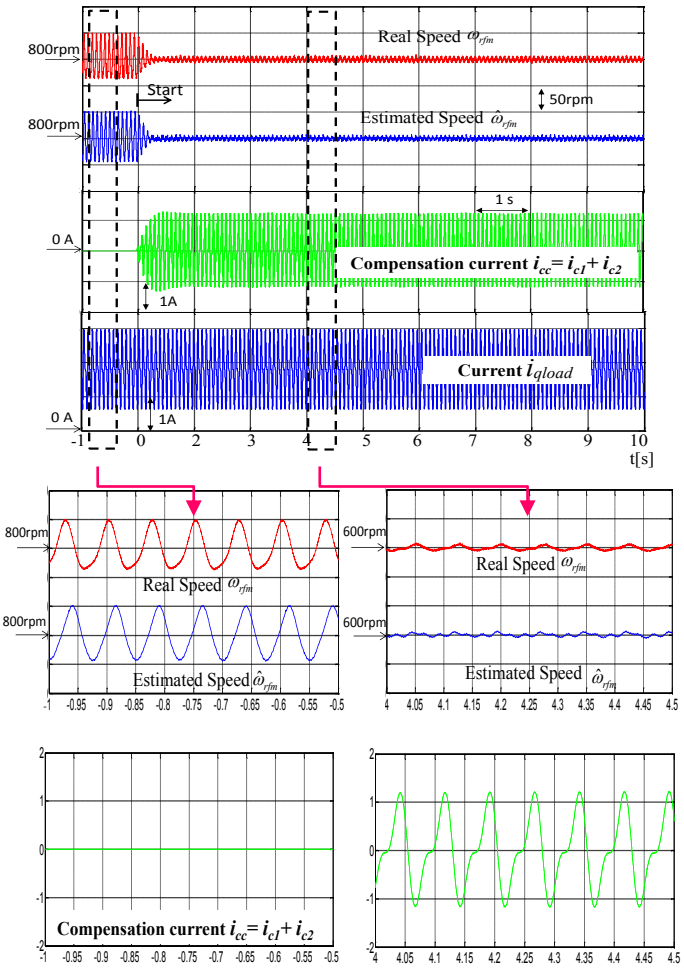

(a) Before Compensation. (b) After Compensation.

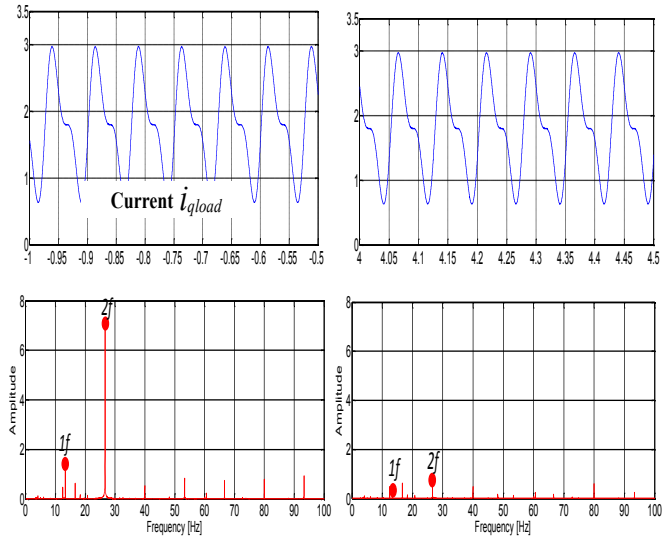

(a) Before Compensation. (b) After Compensation.

Fig. 7.7 Case (B'n_1,n_2): "Desirable case"(at different operating point, the rotor speed 800 [rpm] (f = 13.33 [Hz])). Enlarged view and FFT analysis.

Fig. 7.7 shows a result of the proposed method at different operating point, the rotor speed 800 [rpm] (corresponding to 13.33 [Hz] and 26.67 [Hz]) shown in Fig. 7.3(b). When the Nyquist point is close to the original point Case (Bn_1,n_2) the speed vibration suppression is faster. Also, when the Nyquist point is on the unit circle Case (B'n_1,n_2) by using the parameters k_{in} and φ_{cn} as same in the Case (An_1,n_2) shown in Fig.7.3(a). It is the desirable point control. The speed vibration suppression takes short- time in Fig. 7.7. The target frequency are n_1 = 91.5% and n_2 = 82% reduced by MSCRC as shown in Fig. 7.7.

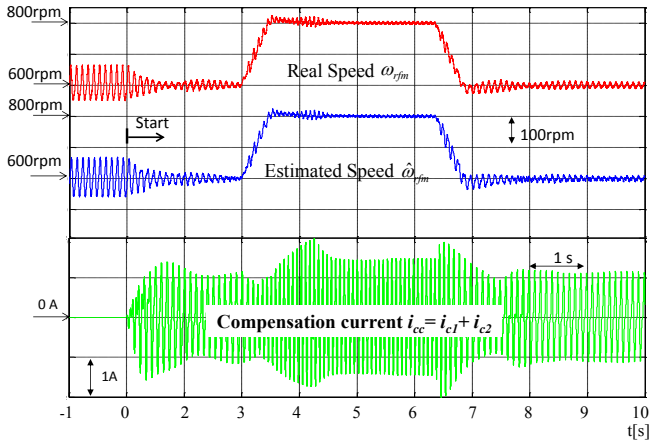

Fig. 7.8 Speed variable suppression vibration control with different operating point, the rotor speed 600 to 800 [rpm].

Fig. 7.8 shows the Nyquist plot for the variable speed operation, under the condition with Fig. 7.3(a)(An_1,n_2) and Fig. 7.3(b)(B'n_1,n_2). Fig. 7.8 shows that SCRC has the ability to achieve variable speed suppression vibration control, if Nyquist analysis is in the unit circle.

7.5 Conclusions

In this paper, a novel PMSM vibration suppression control method called M-SCRC has been proposed to suppress the multiple components in IPMSM frame vibration system. System stability analysis with Nyquist diagram has been proposed to design two most important parameters in MSCRC. When Nyquist point of the proposed system diagram is within the unit circle, the whole system is stable. The target frequency harmonics components are eliminated by MSCRC. Experimental results show that the proposed MSCRC with IPMSM position sensorless control system is quietly useful for suppressing periodic load torque in different speed regions , without accelerometer. The speed variable sensorless suppression control also can be achieved with MSCRC. The speed variable sensorless suppression control also can be achieved with MSCRC.

Our future work will focus on the stability analysis in the low speed region.

7.6 Acknowledgement

This work has been supported by MIU (Mie University and Motor control Laboratory) and the DSP (TMS320C6713) of the Myway Corporation.

References

[1] T. Su, S. Hattori, M. Ishida, and T. Hori, “Suppression control method for torque vibration of ac motor utilizing repetitive controller with Fourier transform,” IEEE Trans. Ind. Appl., vol. 38, no. 5, pp. 1316–1325, Sep 2002.

[2] M. Zhang; Y. Li; T. Zhao; Z. Liu; L. Huang, "A speed fluctuation reduction method for sensorless PMSM-compressor system," in Industrial Electronics Society, 2005. IECON 2005. 31st Annual Conference of IEEE , vol., no., pp.5 pp.-, 6-10 Nov. 2005.

[3] A. Shimada, K. Kawai, T. Zanma, S. Doki, and M. Ishida, “Sensorless Suppression Control for Frame Vibration of PMSM,” IEEJ Trans., vol. 128, no. 11, pp. 1246-1253, 2008.

[4] J. Kim; K. Nam, "Speed ripple reduction of PMSM with eccentric load using sinusoidal compensation method," in Power Electronics and ECCE Asia (ICPE & ECCE), 2011 IEEE 8th International Conference on, vol., no., pp.1655-1659, May 30 2011-June 3 2011.

[5] T. Yamaguchi, Y. Tadano, N. Hoshi, “Torque Ripple Suppression Control by Periodic Disturbance Observer with Model Error Correction,” IEEJ Trans., vol.134, no. 2, pp.185-192, 2014.

[6] Z. Chen, M. Tomita, S. Doki, and S. Okuma, “An extended electromotive force model for sensorless control of interior permanent magnet synchronous motors,” IEEE Trans. Ind.
Electron., vol. 50, no. 2, pp. 288–295, Apr 2003.

[7] D. S. Naidu, Optimal Control System, Idaho State University Pocatello, Idaho, UAS, 1940.

[8] S. Hattori, M. lshida and T. Hori, "Suppression Control Method for Torque Vibration of Brushless DC Motor Utilizing Repetitive Control with Fourier Transform," IEEE Trans. Ind. Electron., pp.427-432, 2000.

[9] M. lshida, Tinghsu Su, S. Hattori, and T. Hori, “Suppression control method for torque vibration of AC motor utilizingrepetitive controller with Fourier transformer”, Industry Applications Conference of IEEE, vol.3, pp.1675 – 1682, 2000.

[10] K. Kawai, T. Zanma and M. lshida, "Simultaneous Vibration Suppression Control for Permanent Magnet Synchronous Motor Using Repetitive Control and Feed forward Compensation” IEEJ Trans. IA, Vol. 127, No. 7 , 2007.

[11] S. Suthep, Y. Wang, N. Yamamura, M. lshida K. Yubai, S. Komada and M. lshida " Frame Vibration Suppression Method for Sensorless PMSM-Drive Applications”, JPE Trans. , 2016. (Accepted for public).

Chapter 8

Conclusion and Future Work

8.1 Conclusion

In the earlier researches, the effectiveness of PMSM frame vibration control with Fourier Transformation and the repetitive controller has been proved. But this method needs the accelerometer to detect the frame vibration. Moreover, because of the imperfections of motor structures and controller, this method can't decrease the harmonics in high-frequency.

In this thesis, a position sensorless control method has been proposed. The frame vibration has been detected by SCRS without the accelerometer. SCRS has the same characteristics with the repetitive controller to the controlled plant, but SCRS doesn't increase the harmonics in other frequency. This method is aimed at the compressor, which the torque vibration happens. And then, the stability analysis has been proposed. At last, with this stability analysis, the experiment has been carried out. The effectiveness of the research has been demonstrated.

A novel PMSM vibration suppression control method called M-SCRC has been proposed to suppress the multiple components in IPMSM frame vibration system.SCRC has been developed. Not only the first-order frequency component has been involved in the controller, but also the second-order one. It shows that SCRC can be taken into practice of multipled components application. As a result, this controller is named as Multipled Specific Component Reduction Controller(M-SCRC). The experimental results show that the proposed MSCRC with IPMSM position sensorless control system is quietly useful for suppressing periodic load torque in different speed regions , without accelerometer. The speed variable sensorless suppression control also can be achieved with MSCRC. The speed variable sensorless suppression control also can be achieved with MSCRC.

8.2 Future Work

In this thesis, position and accelerometer sensorless frame vibration control have been proposed. Based on the stability analysis, the effectiveness of the research has been demonstrated by experiment. But as the poposed method requires exact sysrem parameters, the system must be identified a proper values of parameter first. The method

in this thesis has been used the trial and error procedure for determining the values of the parameters. And the frame vibeation frequency approaches the mechanical resonance frequency of the frame suppression system, it is difficult for SCRS to keep the system stable. And the position sensorless method, using a low-pass filter and the Extended Electromotive Force Model can't estimate very low speed including zero speed. As a result, a huge speed estimation error happens in the low-speed estimation. The PMSM parameter estimation and new position sensorless method will be developed in future.

Moreover, Stability analysis of M-SCRC is also required to realize the parameter determination procedure which stabilize the vibration suppression system, by applying the auto-tuning algorithm for the M-SCRC parameters. Also, the control parameters can be changed automatically for the change of the motor operating point or the controlled system by the proposed method, and the M-SCRC system can behave stably.

List of Publications

A.1 Journal Paper

[1] S. Suthep, Wang Yankai, M. Ishida, N. Yamamura, K. Yubai and S.Komada , "Frame Vibration Suppression method for Sensorless PMSM-Drive Applications", Adjustable Speed Drives, Journal of Electronics (JPE), (Accepted, to be published on Nov. 2016).

[2] Supharat Suthep, Wang Yankai, Itokawa Yuuma, Muneaki Ishida, K. Yubai and S.Komada, "Frame Anti-Vibration Control for Sensorless IPMSM-Driven Applications",in Proc. Of the 19th IEEE IECON2016, Annual Conference of the IEEE Industrial Electronics Society, iazza Adua, Italy, in October 23-27, 2016. (Accepted)*
* to be updated and reviewed for Trans. on IE after Conference.

A.2 International Proceedings

[1] S. Suthep, W. Yankai, M. Ishida, N. Yamamura, K. Yubai and S.Komada, "Anti-vibration Control System with Frame Vibration Suppression Method for Sensorless IPMSM-driven Applications," in Proc. Of the 19th IEEE International Conference on Electrical Machines and Systems (ICEMS 2016), , in Chiba, Japan, in November 13-16, 2016 .

A.3 Other (international conferences and domestic study group without peer review)

[1] Supharat Suthep, Wang Yankai, Muneaki Ishida, "Sensorless Speed Estimation Control of Field Orient Control(FOC) for PM Synchronous Motor Based on Back-EMF Observer," Proceedings of the 4th International Symposium for Sustainability by Engineering at MIU, Dcc. 3rd,2014.

[2] S. Suthep, M. Hohsino, M. Ishida, N. Yamamura, K. Yubai and S. Komada , "Simultaneous Vibration suppression control for sensorless PMSM drive by Utilizing Multiple-Specific Component Reduction Control method.", International Research Journal of Engineering and Thechnology (IRJET), (submitted).